Inverse Design of Plasmonic Nanoparticle Metamaterials

Rishabh Sanghavi

A dissertation submitted in partial fulfillment of the
requirements for the degree of

Doctor of Philosophy

University of Washington

2026

Reading Committee:

Zachary Sherman, Chair

Lilo D. Pozzo

David Beck

Brandi Cossairt

Program Authorized to Offer Degree:

UW Chemical Engineering

University of Washington

Abstract

Inverse Design of Plasmonic Nanoparticle Metamaterials

Rishabh Sanghavi

Chair of the Supervisory Committee:

Assistant Professor Zachary Sherman

Department of Chemical Engineering

Self-assembly of strongly coupled plasmonic nanoparticles is a scalable and promising route for producing optical metamaterials with emergent photonic properties, with applications in nanophotonic devices to function as energy harvesters, waveguides, optical filters, and photo- and thermocatalysts. The optical response of these materials can be tuned through nanoparticle size, shape, arrangement, and chemical composition, resulting in a vast design space that is too time-consuming and expensive to navigate using "forward" strategies. To this end, we formulate optical metamaterial design as an inverse problem, where we specify target optical behavior and use numerical optimization to autonomously discover nanoparticle metamaterials possessing the desired features. Our design framework uses a gradient-based iterative optimization approach to rapidly navigate through candidate materials self-assembled from tens of thousands of nanoparticles, specifying the position, size, dielectric properties, and other physical features of each nanoparticle. In particular, we demonstrate inverse-designed nanoparticle metamaterials with tunable extinction spectra of complex lineshape for quasi-2D stratified metasurfaces and 3D metamaterials. The optimizer converges to highly heterogeneous structural motifs with resonance frequencies distributed across the target spectrum. We also describe a general approach for finding the derivative of any optical figure of merit and use it to inverse design electric near-field intensity with spatial profiles matching targeted patterns. In doing so, we show that the optimizer can simultaneously control mesoscale structure and local microstructure.

Metamaterial designs optimized at a single angle of incidence have uncontrolled responses at other incidence angles, which limits their use in applications requiring angle-dependent behavior. In the second part of the thesis, we extend our inverse strategy to simultaneously control both the incident frequency and incident angle response of plasmonic metamaterials. We inverse design quasi-2D stratified metasurfaces with tunable extinction spectra that are nearly independent of the incidence angle. To connect directly to measurable observables, we derive expressions for the derivatives of transmittance and reflectance with respect to nanoparticle position and physicochemical features and demonstrate how these can be incorporated into optimization routines. Lastly, we discuss three promising future research projects that leverage our inverse design methodology as a key component: inverse design of the colloidal interactions and self-assembly protocols to produce optical metamaterials, magnetoplasmonic materials controlled with magnetic-field-directed self-

assembly, and ellipsometric characterization of nonuniform thin films.

In the final section of the thesis, we present a mechanistic study of the depolymerization of polyethylene terephthalate (PET), a polymer that frequently adds to postconsumer plastic waste. One of the ways to recover valuable raw materials from postconsumer plastic waste is by depolymerizing PET into its monomeric constituents, dimethyl terephthalate (DMT), and ethylene glycol (EG) through methanolysis with the help of acid or base catalysts. Tertiary amines are attractive base catalysts for this process because, unlike metal-based catalysts, they avoid generating environmentally harmful waste. However, their catalytic mechanism remains unexplored, limiting efforts for plastic upcycling. Using density functional theory (DFT) and transition state analysis, we show that tertiary amine-catalyzed methanolysis of PET can proceed through a stepwise mechanism involving multiple discrete steps, rather than a single concerted step. Comparing our calculations with experimental results, we find that DMT yield correlates with charge polarization in the amine catalyst, suggesting a possible atomic-level descriptor for future catalyst design.

TABLE OF CONTENTS

Page

LIST OF FIGURES

Figure Number Page

LIST OF TABLES

Table Number Page

ACKNOWLEDGMENTS

This dissertation describes my research contributions during this PhD, but it does little justice to the people behind the scenes who made it possible. It was only through the unending support of everyone around me that I made it through. Over these years in the program and in Seattle, I've been fortunate to be surrounded by friends, colleagues and members of the community. It would be impossible to thank them all, but I want to express my sincere gratitude to each and every one.

I want to begin by thanking my committee members, David Beck, Brandi Cossairt, and Lilo Pozzo, for supervising my general and final exams and guiding my research. They brainstormed ideas with me, helped me see how my work connects to colleagues in other fields and facilitated genuine discussions that I looked forward to. I'm also grateful to Jim Pfaendtner, Julie Rorrer, and David Bergsman for supervising my preliminary exam. Julie went further, mentoring me and giving me opportunities to improve my presentation skills, including through her chemical reaction engineering course. Thank you Julie, for being an excellent mentor in the department while I worked on plastic upcycling and catalysis projects.

I've had the absolute pleasure of spending the last five years alongside colleagues from the Pfaendtner research group and Z lab. Thank you to Alyson Shoji, Lejla Beiberic, Kaylyn Torkelson, Christian Philips, Orion Dollar, Jessica Kong, and T. Emme Burgin in the Pfaendtner research group for being great friends and colleagues through lunches and many happy hours. Alyson, Lejla, Kaylyn, and Christian never missed an opportunity to make sure I was laughing and not taking everything seriously during a period of transition. It was inspiring to witness their growth as scientists firsthand. We went through various parts of this rocky journey together and they have became trusted friends that I can count on.

I got to work alongside Haoqing Zhang, Yu-fang Hsieh, Hanson Chen, and Kenny Lam in the Z Lab. They really brought our basement office back to life. Thank you for playing racquet sports with me during lab breaks and group outings, and for always showing up to celebrate my milestones. I'll always treasure the thoughtful cards, snacks and the biggest balloon I've ever received as a gift. I can't wait to see all the amazing things they do next and celebrate their wins with them. Huge thanks also go to my cohort mates and friends in UW ChemE. Through many homework sessions in the first year, celebrations, happy hours and coffee breaks, you all made the hard parts of this degree easier to get through.

Thank you to Jim Pfaendtner for introducing me to computational molecular science. I've learned a lot about quantum chemistry calculations and molecular dynamics from him. The passion Jim brings to teaching is evident to anyone who watches him mentor students. I'm glad to have him as a mentor.

I joined my advisor Zach Sherman's group as one of his first students, in my third year and I cannot thank him enough for taking me on. Zach is an immensely talented scientist, a prolific presenter, and a passionate educator. His passion for science is unmistakable the moment he starts teaching. He has dedicated huge amounts of time every week to explain concepts, discuss research,

brainstorm ideas, and work through problems. His feedback consistently made my work better and he fundamentally changed how I present my research for the better. Nothing in these pages would exist without his guidance and efforts in helping me get this together. I've had the chance to watch closely how he mentors and supports students while pushing them to ask questions and think for themselves. As I move forward in my career, I hope to carry forward the I gained from Zach as both a scientist and a mentor.

I had the great opportunity to work with four very talented undergraduate students. Vera Kotova was the first student I worked with, and I must thank her for her patience working with me as a first-time mentor in a lab that was still coming together. Vera handled the uncertainty and open-ended nature of a new lab with patience and excitement and was a joy to work with. She made important contributions to laying the foundation for our work in chapter 5 on inverse design of incident angle agnostic metamaterials. Next, I have to thank Andrew Imaoka, who spent the summer at UW and tackled a novel project with experimental collaboration. Andrew drove the work from day one and I got to learn a lot from his background in mathematics. He established the basis of a completely new project through extensive simulations and collaborated with colleagues running ellipsometry experiments. Adam Nixon joined the lab in his senior year to complete his honors thesis. He trained and collaborated with many graduate students in the lab, generating a huge amount of data on magnetoplasmonic nanoparticles right away in his first quarter and opened many avenues of future exploration built upon the work in this thesis. Lastly, I want to thank Sabrina Boczek. Sabrina came in with ideas to improve our optimization framework right away. Given her extensive background in applied mathematics, I learned so much from her about optimization techniques and how they could be applied to our efforts to inverse design metamaterials. All of them were stewards in the department, wearing multiple hats, juggling jobs, mentoring other students. Even while carrying a demanding undergraduate degree, they found the time to help me with research. Thank you so much

I have to thank Nadia Intan specifically. As a postdoc winding down in PRG, Nadia was preparing for her next role when Jim was transitioning to a new job, right as I was wrapping up my second year. Nadia carried me across the finish line to publish my first-author paper. Through honest feedback, suggestions and encouragement, she taught me a great deal about writing scientific publications. She did this while transitioning in her own career, during an extremely busy, chaotic time. I'm immensely thankful to Nadia for this.

I got to begin grad school in the Pfaendtner research group at the same time as Marlo Zorman, Ava Waggett, and Nisarg Joshi. I think one of them still owes the other a couple of oat milk lattes, but I won't name names. Having a built-in group of smart, driven, funny friends from day who care for your success just as much as their own is a rare adult experience. I'll forever be grateful to have shared this experience with them. Research can turn into a solitary pursuit very quickly given the nature of the job. So having them alongside me while transitioning into grad school in a new city was priceless.

I must single out Ayça Ersoy and Marlo Zorman. We started this long journey together and they've stuck it out with me all the way to the finish line. Thank you for taking all the water break walks to LSB with me. I could not have imagined I'd be so lucky to go to grad school with them. I cannot put into words how much they've contributed to my growth as a person. They have truly made my life in Seattle. When trips to the basement office got monotonous over the years, I'd go

back anyway just because I knew I'd get a chance to say hi to them. I am so grateful to have them both as a mentors, friends, and role models to look up too.

Seattle has felt like home away from home for years because of the community around me. Huge thanks to my therapist for helping me grow, find my place in this community, and navigate the challenges of being an adult in a big city far away from home, and of course, for hearing the same thing repeatedly through the years. Thanks to my friends at Husky Running club, especially Ken Masumoto, for introducing me to the running community in Seattle. Special thanks to all coaches at Club Northwest, who gave me an outlet to cut off from long research days during Tuesday night track practices. It was an absolute joy to be able to go to these practices and track meets with them.

Being so far way from Mumbai, all the time I have gotten to spend with my family has been precious. Thank you for your constant, selfless and unwavering support. Thank you to my sisters Rajvi and Hiral, my brother Pratik, my aunt Kashmira, my uncle Bhavesh, my grandparents and my parents Bindi and Dipesh. The countless opportunities I have received in life is because of you all. Your sacrifices, support, and time are immeasurable There is no way I would be able to write this thesis without you. I love you all!

DEDICATION

To my family and friends, for everything you have done to help me succeed

Chapter 1

Introduction

Colloids are mesoscopic particles with size between 1 nm and 1 μm dispersed in a continuous medium, such as gas or liquid.[1,2] They are "supramolecular" — much larger than atoms and molecules but much smaller than the macroscopic objects we interact with day-to-day. Colloids are seen everywhere in our daily lives, including in detergents, milk, paints, and inks. They act as drug carriers for poorly water-soluble drugs,[3] as rheological modifiers in paints, inks, coatings,[4] as foam stabilizers in detergents and fire suppressants,[5], and as cosmetic components.[6]

Brownian motion, the stochastic "jerky" motion of colloidal particles in a solvent, is the defining feature of colloidal dispersions. Collisions and interactions between solvent molecules and colloid surfaces happen on timescales that are much faster than the timescales on which the colloids move. Due to this separation of timescales, the colloids experiences a huge number of solvent-colloid interactions over a short time[1] resulting in a stochastic net force. This stochastic force drives a "random walk" trajectory, i.e. the colloid experiences Brownian motion. This motion is quantified by the colloid's diffusivity $D = k_B T/\gamma$, where γ is the hydrodynamic drag coefficient of the colloid. Thus, the energy driving Brownian motion the thermal energy $k_B T$ of the solvent. Gravity also acts on colloidal particles, and the ratio of colloid radius a to the "sedimentation length" $\ell = k_B T/mg$, where m is the buoyant mass and g is the gravitational acceleration, characterizes whether sedimentation or diffusion will dominate the colloid's motion. When $a \ll \ell$, Brownian motion dominates sedimentation and small particles remain suspended in solution. When $a \gg \ell$, large particles sediment to the bottom (if denser than the solvent) of the container or cream to the top (if less dense than the solvent).

The interaction between two colloids is the sum of the interactions between all the atoms of the two colloids. This can be conveniently represented through an effective colloidal pair potential that is a function of, for spherical colloids, only the center-to-center distance. Analogous to how atomic potentials determine the equilibrium structure and macroscopic properties of the materials they make up, so too does the colloidal interaction potential determine the structure and properties of colloidal materials. While we cannot engineer atomic pair potentials, colloidal pair potentials are highly tunable through the features of the colloid, its surface, and the solvent.[2]

The colloidal interaction potential determines if a colloidal dispersion is "stable", where particles remain suspended, or "unstable", where particles irreversibly aggregate and crash out of solution.[4,7] All colloids interact via van der Waals forces, whose strength depends on the dielectric contrast between each colloidal particle and the intervening continuous phase. Van der Waals interactions are always attractive and diverge to infinite strength as the surface-to-surface separation approaches zero. Without the presence of any other repulsive interactions, van der Waals forces cause colloids

[1] short compared to colloid motion but long compared to solvement molecule motion

to irreversibly aggregate and crash out of solution.

Colloids can be stabilized through electrostatic interactions. When dispersed in liquids, the surface of colloidal particles typically become charged. The surface charge attracts oppositely-charged counterions from the solution and repels like-charged co-ions, creating a region of excess counterions near the particle surface, called the "double layer". If the colloids have the same net charge, they will repel one another. Due to the ions in the double layer, the length scale over which the colloids experience appreciable electrostatic interactions, i.e. the "screening length", is smaller than that for electrostatic interactions between two bare charges. In other words, the ions "screen out" electrostatic interactions between colloids. Colloidal dispersions can also be stabilized by grafting polymeric ligands to particle surfaces, resulting in steric repulsions between the polymer layers that also have an associated interaction range. Therefore, there is typically a delicate balance between the attractive forces that drive colloidal instabilities and the repulsive interactions stabilizing them. Stabilizing repulsions must keep the colloid surfaces far enough apart to prevent van der Waals attractions from driving irreversible aggregation. The Derjaguin-Landau-Verwey-Overbeek (DLVO) interaction potential is a simple model capturing this for a sum of van der Waals attractions and screened electrostatic repulsions. Through analysis of the DLVO potential, we can predict for example, the salt concentration at which a stable colloidal dispersion will become unstable.

We can induce and control *reversible* attractions between colloids by adding depletants, such as small particles or nonadsorbing polymer chains, to colloidal dispersions.[2] The center of mass of the depletant is sterically excluded from a region around each colloid. If two colloids come close enough to each other, their "depletion zones" overlap and depletant is excluded from the gap between them. Depletant in the surrounding solution creates a high osmotic pressure that pushes on the pair outside the gap, but there is no depletant inside the gap to counteract this force. This osmotic pressure imbalance pushes the two colloids together and creates an effective "depletion attraction" between the colloidal particles. The depletion forces are purely entropic and do not depend on the chemical composition of the colloids or the depletant. An equivalent way to rationalize depletion is to realize that the free volume accessible to the depletant increases as colloids move close together. This increase in depletant entropy lowers the overall free energy of the dispersion.

This tunability over colloidal interactions can be utilized to controllably self-assemble colloids. Self-assembly is a "bottom-up" approach to structure formation, in which colloidal building blocks arrange themselves. This contrasts "top-down" methods like lithography and 3D printing. Self-assembly can be further categorized as "static", where colloids spontaneously assemble with no external energy input, or "dynamic", where external energy sources drive structure formation.[8] Static self-assembly can only be controlled through tuning of the interparticle potentials, while dynamic self-assembly can be tuned by both interparticle interactions and the external energy source. Because dynamic self-assembly is not constrained by equilibrium thermodynamics, it can access a much broader variety of complex structures and states, including those that are dissipative and time-varying.

Therefore, colloids have a vast design space for self-assembly. We can control colloidal interactions through strategic design of the building blocks and can assemble them into essentially any target structure we want, provided we can engineer the appropriate interparticle interactions. In this thesis, I focus on the use of self-assembled soft matter for nanophotonics. Colloids have very strong light-matter interactions and, consequently, interesting optical properties because their size is commensurate with the wavelength of light. Purely "geometric" optical interactions occur due to particle size in otherwise optically "boring" materials. In metals and metallic-like materials, plasmonic light-matter interactions due to mobile electrons are strong. Because incident light

waves have an electric field component that oscillates with time, they exert electrophoretic forces on the free electrons driving oscillatory electron motion in time. This collective electron motion induces electric polarization within the material, resulting in charge separation at interfaces. In nanoparticles, the plasmon modes are confined to the small volume of the nanoparticle and are therefore termed "localized surface plasmon resonance" (LSPR), contrasting bulk plasmons in bulk materials and surface plasmon resonance (SPR) at planar interfaces. The oscillating electrons inside the nanoparticle induce an electric dipole moment $\mathbf{p}$ that also oscillates in time. The dipole oscillates at the same frequency as the incident light, but with a phase lag. The magnitude of the dipole moment changes with the incident light frequency and we specify the frequency around where $|\mathbf{p}|$ is maximized as the LSPR frequency. At the LSPR frequency, the large dipole moment result in enormous optical absorption and scattering, large near-field enhancement near the nanoparticle surface, and large heat generation.

A review paper on LSPR in semiconductor nanocrystals[9] details that investigations of plasmonic nanoparticles have primarily focused on metals, such as gold and silver, which are straightforward to synthesize.[10–12] Metals, by definition, have free electrons in their conduction bands and are therefore plasmonic. However, *any* material containing free electrons is plasmonic. For example, semiconductor materials can be synthesized in a metallic state through atomic doping, which changes the Fermi level and pushes electrons into the conduction band. This is especially useful because the concentration of free electrons, and therefore their LSPR frequency, can be tuned with the doping amount. The chemical composition of host semiconductor and dopant, the spatial distribution of dopant, and the nanoparticle size and shape all also affect the LSPR mode.[9] These parameters are tuned via the colloidal synthesis procedure.[13,14] Several synthetic approaches have been developed for nucleation and growth of metal and doped semiconductor nanoparticles, including hot injection, continuous injection, and heat-up methods.[15,16] The physicochemical features of the synthesized nanoparticles are determined by, for example, the choices of solvent, metal precursor, organic surfactant, temperature, and synthesis time. After synthesis, the concentration of dopants and nanocrystal volume fractions can be measured with inductively coupled plasma mass spectrometry (ICP-MS) or atomic emission spectrometry (ICP-AES).[17,18]

A variety of instruments are used to measure light-matter interactions. Transmission spectra are measured in UV-vis-NIR (ultraviolet-visible-near infrared) spectrometers, from which extinction and, in some cases, absorption spectra can be extracted. Longer wavelengths (lower frequencies) can be measured in a Fourier transform infrared (FTIR) spectrometer.[18,19] By fitting dielectric models to the measured extinction spectra of very dilute nanoparticle dispersions, the dielectric function of the nanoparticles can be determined. Ellipsometers measure the amplitude shift, phase lag, and change in polarization state of reflected and transmitted light off a material at a range of incidence angles, from which the complex dielectric function can also be inferred.[20] Photoluminescence, the emission of light after absorbing photons, can be measured in interferometers.[21] Dynamic light scattering (DLS) provides information about the particle size distribution, which is typically characterized by a mean size and a polydispersity.[22] More accurate particle size measurements can be obtained using transmission electron microscopy (TEM)[23] or via light scattering techniques, i.e. static light scattering (SLS) and small angle X-ray scattering (SAXS).

Surface-enhanced Raman spectroscopy (SERS) leverages plasmonic resonance to detect molecules. The Raman signal captures information about interatomic bonds in a molecule by detecting a shift in the energy of light when it interacts with these bonds. The Raman signal is generally weak, but when the molecule is placed near a plasmonic substrate, the strong local field intensity due to LSPR on the substrate can amplify the Raman signal, dramatically enhancing the signal-to-noise ratio in

SERS.[24] For more information, Maier and co-workers write a thorough discussion of imaging and characterization techniques that leverage LSPR.[11]

For many photonic applications, the "desired" material photonic spectrum (or similar optical figure of merit) is known. The materials design task is, given a vast design space, what materials posses this target spectrum and how can they be synthesized? This challenge is usually approached through a *forward* strategy, which relies on trial and error synthesis and characterization of many materials. The process must be repeated many times to screen for materials with properties that match the target, which can be expensive and time-consuming. This is a challenge whether we are designing materials in the lab or simulating them *in silico*. As discussed earlier, colloidal interactions and self-assembly offer a vast, tunable design space for engineering material properties. *Inverse* design offers a strategy to navigate this large parameter space efficiently and design soft materials with desired optical responses without needing to test impractically large numbers of candidates. In an inverse approach, we specify a target optical property as an input to a numerical optimization routine. The optimizer then steps through the tunable design parameters to reach a material design that displays the target optical property. This is advantageous because we only need to consider the material designs on the optimization path rather than exhaustively sample the entire design space via parameter sweeps.

In this thesis, I develop inverse routines to design nanoparticle-based optical metamaterials. "Metamaterials" display *emergent* light-matter interactions that depend not only on the identity of the building blocks making them up but also on their structural arrangement. Note, that quasi-2D metamaterials are often called "metasurfaces" and we'll switch between the two descriptors. Metamaterials with remarkable light-matter interactions have been fabricated including materials that selectively transmit a specific polarization state, display structural color, and perform "calculations" on images.[25]

A key component of any computational design tool for photonic materials is the simulation method for light-matter interactions.[26] In classical electromagnetism, optical simulations amount to numerical solutions of Maxwell's equations. Typical electromagnetic methods for solving Maxwell's equations include finite element, finite-difference time-domain, and discrete dipole methods,[27,28] and the method of moments.[29,30] These can handle a small number of nanoparticles well with complex geometries, but are computationally expensive for materials with a larger number of nanoparticles.[31] Coupled dipole methods[32–34] capture the effect of dipoles induced in each nanoparticle on its neighboring nanoparticles and the overall material assembly, and can treat larger configurations of nanoparticles. Similarly, transition-matrix approaches, multi-particle Mie theory,[35,36] and boundary element methods[29,37] scale efficiently to large configurations. Based on these, our approach to solving Maxwell's equations is through the mutual polarization method (MPM),[38] discussed in detail in Chapter 2 and the methods section of Chapter 3.

Optimization schemes either make use of gradients of the objective function with respect to parameters or are gradient-free. Gradient-free methods include genetic algorithms,[39] particle swarm optimization,[40] non-linear search methods, and hybrid methods that mix particle swarm optimization with genetic algorithms.[41] Bayesian optimization is also a gradient-free algorithm, based on calculating the posterior distribution of an event given prior events. It builds a surrogate model that calculates this posterior distribution of the optical objective function, and then uses an acquisition function to decide what parameters to sample next.[42,43] These gradient-free methods work well only for smaller system sizes and simpler geometries. As the system scales up and the parameter space grows, these methods become computationally more expensive. They may be useful in cases where it is not possible to compute the gradient or access it.[44] Gradient-based

optimization is hence more widely used for photonic inverse design. Gradient-based approaches are well documented in the literature,[45] and gradients provide optimization algorithms with a path to improve the solution. The solution may be either a local or global minimum, but will still improve the photonic design. Topology optimization is often used as a gradient-based, steepest-descent optimization method to determine the optimal design of a material, such as a wavelength demultiplexer.[46,47] Gradient-based methods can additionally handle a larger design space and material size. While this may intuitively suggest greater computational expense, this can be handled through the adjoint method. The adjoint method calculates the gradient for the entire material through just two calculations: one *forward* and one *adjoint*, irrespective of material size or number of parameters.[48] Gradient-based optimization and the adjoint method are reported in detail and implemented in Chapter 3.

A third category of inverse design methods is using deep learning. Both gradient-based and gradient-free methods involve solving Maxwell's equations in the mathematical model repeatedly at each iteration, which can become computationally prohibitive for more complex systems. Neural networks (NNs) in deep learning can map directly between input and optical response. They can also be trained on the inverse mapping, from optical response to input, and act as a surrogate model that learns this mapping directly, removing the need to run iterations.[49] Additionally, their ability to universally approximate any continuous function, as established by the universal approximation theorem, has made them a promising alternative for inverse design problems.[50] In photonics, small changes in parameters may either not affect the output optical property or lead to an unexpected jump, i.e. it is common to have non-linear relationships that need to be captured. A deep learning architecture, known as a neural network, is built from layers that take data as input. NNs can have non-linear layers to capture non-linear optical relationships.[51] A wide variety of networks are available for training, such as convolutional neural networks (CNN), recurrent neural networks (RNN), generative models, and generative adversarial networks (GAN). Their contributions to inverse design in photonics are discussed in detail in the 2023 review paper.[26] Choosing the right network, and whether to use it stand-alone or in conjunction with adjoint methods, based on the training data and the optical problem at hand, remains an open design choice to explore.

A clear limitation of applying deep learning is the amount and quality of training data available. Generating large datasets will inevitably require running electromagnetic simulation methods. The dataset would also need to be tailored to the optimization problem being solved. The solution could also be degenerate and harder to narrow down to the correct set of optimized parameters. Another limitation is that if the optimization goal changes, the dataset needs to be modified and recreated every time, and its generation is not a straightforward or quick process. While solutions to implement DL, such as transfer learning, where trained neural networks can be repurposed, have been implemented in photonics, they are not discussed at length here since they are not the focus of this thesis.[52] Deep learning methods provide a wide scope for future research to inverse design optical materials.

Topology optimization is often used as a gradient-based, steepest-descent optimization method to determine the optimal design of a material, such as a wavelength demultiplexer.[46,47] Gradient-based methods can additionally handle a larger design space and material size with the same number of iterations. While this may intuitively suggest more parameter calculations per iteration for more particles, and thus greater computational expense, this can be handled through the adjoint method. The adjoint method calculates the gradient for the entire material through just two calculations: one *forward* and one *adjoint*, irrespective of material size or number of parameters.[48] Gradient-based optimization and the adjoint method are reported in detail and implemented in Chapter 3.

Despite how well topology optimization works for materials with complex patterns from lithography, it cannot be directly applied to nanoparticles, which are discrete and can self-assemble. The goal of my thesis is to create a gradient-based inverse design method for NP metamaterials. We can utilize the same computational advantage that adjoint method provides and can handle larger design space of nanoparticles.

Chapter 2 provides a detailed description of the electromagnetic simulation method MPM used in this thesis. I begin by solving for Maxwell's equations for electric field $\mathbf{E}(x)$ through Laplace equation for electrostatics. Using this, we get local electric field and its gradient. I show the math for calculating dipoles from this, that is then used to calculate the optical property of extinction cross-section. I list out the key features that can be extracted from this optical property and then point to sections where its gradients are calculated analytically for inverse design optimization.

I just discussed why we would like to use gradient-based algorithms for nanoparticle material design. In Chapter 3, I explain exactly how to compute the derivatives of an optical figure of merit with respect to parameters of the dielectric function, position, and size. The idea is to use these parameters to calculate a model spectra and minimize its error with respect to a target spectra using objective function of integrated square error. For minimization of objective function we propagate the gradients with respect to individual parameters. To show that this method is effective for size and chemical composition, we used it to design quasi-2D metasurfaces. To show that this method is effective for position/microstructure, we used it to design 3D metamaterials. We found that our inverse protocol was remarkably effective and flexible in the spectral lineshapes it could reproduce. We demonstrated that we could easily tune a material's dielectric plasma frequency, size and resonance frequencies by simply changing the input spectrum. Through repeated use of the inverse protocol we learned that both multilayer metasurfaces and 3D metamaterials can optimize to reach a similar target response. Structure and dielectric properties of both material are completely different. We also learn that plasmonic coupling between layers is weaker, while it is much stronger between individual nanoparticles. We also show how to run inverse design for other figures of merit via adjoint methods. We show this method is effective by designing for spatial profile of electric field intensity in a polka dot pattern by optimizing particle positions. We find that nanoparticle dipole moments depend on both frequency and polarization. As particles update position during the optimization, it couples both changes in dipole and resonance frequency due to change in plasmonic coupling.

In Chapter 3, I explained how to control the frequency-dependent behavior of a metamaterial through gradient-based methods. In Chapter 4 I explain how to control the angle-dependent behavior. In particular, I show how to use inverse design to design a quasi-2D metasurface, which innately has large angle dependence. We used an objective function that considered both how close the FOM is to a target FOM and how close the FOMs in two polarization states are to one another. Using it we designed quasi-2D multilayer metasurfaces for complex extinction spectra where we control the resonant frequency and linewidth of the peak. By decomposing the ensemble extinction into contributions from individual layers, we find that the peaks 'shift-by-one' and overlap with adjacent layer peak of the other polarization state and as a result overall extinction from both polarizations overlap. This is the reason the entire metasurface is nearly independent of the polarization direction. The second half of the chapter is work done alongside Kenny Lam, a PhD student in the lab. We extend our gradient-based design using adjoint method to other optical properties of reflectance and transmittance. We choose them because they can be measured experimentally, while extinction cross-section isn't an experimental observable. I discuss optimization result of transmittance for normal incidence of light, and present scope of future work on calculating

gradients when light is at an angle of incidence. I layout the stratified medium calculation in the methods, used to calculate reflectance and account for incidence angle of light.

In Chapter 5, I investigated the role of tertiary amines as a catalyst for PET depolymerization. We studied the reaction mechanism of PET depolymerization with these amines via methanolysis using density functional theory (DFT)-based methods. The goal of this study was to gain an understanding of the mechanism behind PET methanolysis with tertiary amine catalysts. PET methanolysis has been studied with many metal-based catalysts experimentally, but not much is reported with amines. Amines are known to accelerate transesterification reaction and tertiary amines are promising, because they don't lead to amidation and as a result don't directly participate in the reaction. We used density functional theory (DFT) to study the pathway of this reaction by starting with a base case of methyl ester in place of PET, with the goal of characterizing the simplest methanolysis reaction possible. Transition state structure of the surrogate model was found and confirmed by varying key atomic distances. We were able to use the surrogate model for PET methanolysis by extending it to benzoate structure, which is a more realistic representation of PET. Evolution of the key bonds in transition state structure, and their change in relative energy are discussed in detail in the study. Six different tertiary amines classified as linear, cyclic, aromatic, diamine were then investigated with surrogate model. Energy landscape of the reaction with these catalysts in vacuum and implicit methanol solvent is reported. Role of catalyst in the proton transfer step is investigated through an alternate 2-step process, where proton first transfers to amine nitrogen before breaking the ester bond. We make the argument for why this reaction could be a 2-step process instead, and discuss the correlation between proton transfer energy and experiment yield of PET product DMT, reported for tertiary amine catalysts. Through our investigation, we found that charge on N atom in implicit methanol of tertiary amine catalysts correlates directly with product yield of PET. We make the case for how charge on N atom could be used as a potential descriptor to screen a wider range of catalysts for PET depolymerization. Broadly, the chapter also provides a systematic approach to find transition states for reaction of similar complexity through DFT. A portion of my PhD was done with Professor Jim Pfaendtner and focused on polymer upcycling using catalytic solvolysis for deconstructing municipal wastes. This chapter is a result of that work

Finally, in Chapter 6, I discuss how the results of the work of this thesis can be leveraged to incorporate structural control of nanoparticle metamaterial through inverse design of colloidal interaction parameters to direct self-assembly. Experimental techniques to form monolayer thin films can be corroborated alongside monolayer films designed from gradient-based inverse design. It can be used to determine concentration of thin films. We can also study plasmonic response of paramagnetic nanoparticles self-assembled through external magnetic fields.

Chapter 2

Electromagnetic Simulations of Colloidal Materials

2.1 Governing Equations of Electromagnetism

We'll tackle the problem of a collection of N spherical particles of radius a exposed to an incident electromagnetic wave $\mathbf{E}_{\text{inc}}$. The particles have permittivity ε_p and permeability μ_p, while the background fluid has permittivity ε_f and permeability μ_f, all of which are in general complex numbers and functions of (angular) frequency ω. The response of the dispersion is governed by Maxwell's equations,

$$\nabla \cdot \mathbf{D} = 0, \qquad \nabla \cdot \mathbf{B} = 0, \qquad \nabla \times \mathbf{E} = -\frac{\partial \mathbf{B}}{\partial t}, \qquad \nabla \times \mathbf{H} = \frac{d\mathbf{D}}{dt}, \tag{2.1}$$

where $\mathbf{E}(\mathbf{x}, t)$ is the electric field, $\mathbf{D}(\mathbf{x}, t)$ is the electric displacement, $\mathbf{H}(\mathbf{x}, t)$ is the magnetic field, and $\mathbf{B}(\mathbf{x}, t)$ is the magnetic induction. Writing each of the fields in terms of their Fourier components $\mathbf{E}(\mathbf{x}, t) = \int d\omega\, \mathbf{E}(\mathbf{x}, \omega) e^{-i\omega t}$ and using the linear constitutive relations $\mathbf{D}(\mathbf{x}, \omega) = \varepsilon(\mathbf{x}, \omega)\mathbf{E}(\mathbf{x}, \omega)$ and $\mathbf{B}(\mathbf{x}, \omega) = \mu(\mathbf{x}, \omega)\mathbf{H}(\mathbf{x}, \omega)$, we can show that in a region of space where ε and μ are constant, Maxwell's equations reduce to Helmholtz equations for the Fourier modes

$$\nabla^2 \mathbf{E} + k^2 \mathbf{E} = 0, \qquad \nabla^2 \mathbf{B} + k^2 \mathbf{B} = 0, \tag{2.2}$$

where $k \equiv \omega\sqrt{\mu\varepsilon}$ is the wavenumber. Unless otherwise specified, $\mathbf{E}$ and $\mathbf{B}$ will refer exclusively to the Fourier components and we will drop the ω argument. (2.2) are simpler PDEs, but we must now solve for two different fields, one inside the particles $\mathbf{E}_p$ and another outside the particles (in the fluid) $\mathbf{E}_f$. At each particle's surface, these two fields must satisfy boundary conditions on their normal $\hat{\mathbf{n}}$[1] and tangent $\mathbf{I} - \hat{\mathbf{n}}\hat{\mathbf{n}}$ components

$$\varepsilon_p \hat{\mathbf{n}} \cdot \mathbf{E}_p = \varepsilon_f \hat{\mathbf{n}} \cdot \mathbf{E}_f \qquad (\mathbf{I} - \hat{\mathbf{n}}\hat{\mathbf{n}}) \cdot \mathbf{E}_p = (\mathbf{I} - \hat{\mathbf{n}}\hat{\mathbf{n}}) \cdot \mathbf{E}_f \tag{2.3}$$

$$\mu_p \hat{\mathbf{n}} \cdot \mathbf{H}_p = \mu_f \hat{\mathbf{n}} \cdot \mathbf{H}_f \qquad (\mathbf{I} - \hat{\mathbf{n}}\hat{\mathbf{n}}) \cdot \mathbf{H}_p = (\mathbf{I} - \hat{\mathbf{n}}\hat{\mathbf{n}}) \cdot \mathbf{H}_f \tag{2.4}$$

2.2 Plane Wave Solutions to Maxwell's Equations

The simplest solution to Maxwell's equations is that of a *plane wave*.

$$\mathbf{E}(\mathbf{x}) = \mathbf{E}_0 e^{i\mathbf{k}\cdot\mathbf{x}} \tag{2.5}$$

$\mathbf{x}$ is a position in space, and so $\mathbf{E}(\mathbf{x})$ is the value of the electric field vector at each position $\mathbf{x}$. $\mathbf{E}_0$ is a complex vector, containing both real and imaginary components, and represents the *polarization* state of the light wave (e.g. linearly polarized, circularly polarized). $\mathbf{k}$ is the *wavevector* given by

$$\mathbf{k} = \sqrt{\varepsilon\mu}\,\omega\hat{\mathbf{k}} \tag{2.6}$$

[1] hats indicate unit vectors which have a (complex) magnitude of 1

In general, ε and μ are complex numbers, but we will assume here they are both real in this subsection to simplify our explanations. $\hat{\mathbf{k}}$ is a unit vector indicating the direction of propagation of the light wave. The magnitude of the wavevector $k = |\mathbf{k}| = \sqrt{\varepsilon\mu}\,\omega$ is the *wavenumber*. The frequency of the light wave is related to its wavelength λ as

$$\lambda = \frac{2\pi}{\sqrt{\varepsilon\mu}\,\omega} \tag{2.7}$$

Note that, while λ is the true wavelength of light in a material, nearly everyone uses the wavelength in vacuum λ_0 as *the* wavelength,

$$\lambda_0 = \frac{2\pi}{\sqrt{\varepsilon_0\mu_0}\,\omega} \tag{2.8}$$

where ε_0 and μ_0 are the vacuum permittivity and vacuum permeability. For example, when a spectrum is plotted (i.e. some quantity as a function of wavelength), the wavelength is nearly always λ_0. Also note that the vacuum speed of light is $c = 1/\sqrt{\varepsilon_0\mu_0}$. We won't need it much, but the magnetic field is

$$\mathbf{H}(\mathbf{x}) = Z^{-1}\,\hat{\mathbf{k}} \times \mathbf{E}(\mathbf{x}) = \mathbf{H}_0 e^{i\mathbf{k}\cdot\mathbf{x}} \tag{2.9}$$

where $Z = \sqrt{\mu/\varepsilon}$ is the impedence of the medium. The electric field $\mathbf{E}$, the magnetic field $\mathbf{H}$, and the wavevector $\mathbf{k}$ are all orthogonal to one another and their directions satisfy the right hand rule relation

$$\hat{\mathbf{E}} \times \hat{\mathbf{H}} = \hat{\mathbf{k}} \tag{2.10}$$

Note that this implies that the electric field vector *always* points in a direction orthogonal to the direction of propagation. The *intensity* of the light wave I is the magnitude of the *flux* of electromagnetic energy (energy per area per time) that the light wave contains.

$$I = \frac{1}{2}\Big|\,\mathrm{Re}\,[\mathbf{E} \times \mathbf{H}^*]\Big| \tag{2.11}$$

where $*$ indicates complex conjugation and Re[$\cdot$] indicates the real component of the quantity in brackets. Plugging in for $\mathbf{E}$ and $\mathbf{H}$, the intensity of a plane wave is

$$I = \frac{1}{2Z}|\mathbf{E}_0|^2 \tag{2.12}$$

2.3 Complex Representation of Harmonic Time Dependence

Why do we use complex numbers for wave problems? This is a powerful mathematical notation that greatly simplifies calculations. The *actual* electric field $\mathbf{E}_{\text{true}}$ that would be measured can be written in terms of the complex $\mathbf{E}$ as

$$\mathbf{E}_{\text{true}}(\mathbf{x}, t) = \mathrm{Re}\left[\mathbf{E}(\mathbf{x})e^{i\mathbf{k}\cdot\mathbf{x}-i\omega t}\right] \tag{2.13}$$

$$= \mathbf{E}'\cos\left[\mathbf{k}\cdot\mathbf{x} - \omega t\right] - \mathbf{E}''\sin\left[\mathbf{k}\cdot\mathbf{x} - \omega t\right] \tag{2.14}$$

and similarly for $\mathbf{H}_{\text{true}}$. Unless otherwise specified, prime ($'$) and double prime ($''$) indicate the real and imaginary components of a complex number, e.g. $\mathbf{E}' = \mathrm{Re}\,\mathbf{E}$ and $\mathbf{E}'' = \mathrm{Im}\,\mathbf{E}$. The exponential term $e^{i\mathbf{k}\cdot\mathbf{x}-i\omega t}$ causes $\mathbf{E}_{\text{true}}$ to oscillate as we move through the material (i.e. changing $\mathbf{x}$ at constant t) and over time (i.e. changing t at constant $\mathbf{x}$). The incident field will, in this work, always be a

linearly-polarized plane wave

$$\mathbf{E}_{\text{inc,true}}(\mathbf{x},t) = \text{Re}\left[\mathbf{E}_0(\mathbf{x})e^{i\mathbf{k}\cdot\mathbf{x}-i\omega t}\right] \tag{2.15}$$

$$= \mathbf{E}_0 \cos\left[\mathbf{k}\cdot\mathbf{x}-\omega t\right] \tag{2.16}$$

Comparing to (2.14), we see that the real component of $\mathbf{E}$ represents the portion of $\mathbf{E}$ that oscillates in phase with the incident field and the imaginary component of $\mathbf{E}$ represents the portion oscillating out of phase. Because all oscillating fields have the same *harmonic* time dependence $e^{-i\omega t}$, it can be eliminated from the problem using our complex number notation. This reduces a more difficult time-dependent problem in terms of real numbers into a simpler time-independent one in terms of complex numbers without losing any information! Note that, because the the driving field oscillates in time, several other quantities also oscillate in time, including nanoparticle dipole moments $\mathbf{p}$. We use the same complex number representation for all such quantities.

2.4 Quasistatic Solutions to Maxwell's Equations for Spherical Nanoparticles

For an incident wave $\mathbf{E}_{\text{inc}}(\mathbf{x}) = \mathbf{E}_0 e^{i\mathbf{k}\cdot\mathbf{x}}$, the electric field $\mathbf{E}(\mathbf{x})$ around a single spherical nanoparticle at position $\mathbf{x}_i$ can be solved analytically. The *scattered* field, $\mathbf{E}_{\text{sc}} = \mathbf{E} - \mathbf{E}_{\text{inc}}$, can be written as a multipole expansion

$$\mathbf{E}_{\text{sc}} = \frac{1}{2\pi\varepsilon_f r^3} f(k,r)\,\hat{\mathbf{r}}\hat{\mathbf{r}}\cdot\mathbf{p} - \frac{1}{4\pi\varepsilon_f r^3} g(k,r)\,(\mathbf{I}-\hat{\mathbf{r}}\hat{\mathbf{r}})\cdot\mathbf{p} + \cdots \tag{2.17}$$

where $\mathbf{r} = \mathbf{x} - \mathbf{x}_i$, $r = |\mathbf{r}|$, $\hat{\mathbf{r}} = \mathbf{r}/r$, and the induced electric dipole moment is

$$\mathbf{p} = 4\pi a^3 \varepsilon_f \frac{\varepsilon_p - \varepsilon_f}{\varepsilon_p + 2\varepsilon_f} \gamma(ka)\mathbf{E}_{\text{inc}}(\mathbf{x}_i) \tag{2.18}$$

f, g, and γ are known functions of k, r, a, ε_f, ε_p, μ_f, and μ_p, and all tend to 1 in the *quasistatic* limit. The next terms in the expansion contain the magnetic dipole, electric/magnetic quadrupoles, etc. There are a few length scales we can compare to the wavelength λ to determine when a quasistatic description is appropriate. In the limit of $ka \to 0$ ($a/\lambda \to 0$), the incident field does not vary across the length of the particle, and the particle experiences an effectively constant[2] electric field. In this case, $\gamma \to 1$ and the expression for the dipole moment is the same as the electrostatic dipole moment. Additionally, the higher order terms in (2.17), which are proportional to $\nabla\mathbf{E}_{\text{inc}}$ and higher-order derivatives, are negligible. Next, if we have a finite collection of nanoparticles whose positions span a system size L, we can compare λ to L. In the limit of $kL \to 0$ ($L/\lambda \to 0$), the incident field does not vary across the system and all nanoparticles experience the *same* constant field $\mathbf{E}_0$. Last, we compare λ to the distance r of some point away from the particle. The smallest r can be is a, which is on the surface of the nanoparticle. Whether $\mathbf{E}_{\text{sc}}$ is quasistatic or not is determined by the magnitude of ka, which we already discussed in terms of the dipole moment. If $ka \to 0$, then the *near-field* near the particle surface is quasistatic; $f \to 1$ and $g \to 1$ in (2.17) and $\mathbf{E}_{\text{sc}}$ is identical to the field around an electrostatic dipole. The near-field region retains this quasistatic nature for as long as $kr \ll 1$. However, at some point, r will grow large enough that kr is not small. Unless $k = 0$ (i.e. true electrostatics), the *far-field* where $kr \gg 1$ is never quasistatic. However, only the slowest decaying component of (2.17) is nonnegligible here, so the far-field typically has a simple

[2]This field is nearly constant in space but it still oscillates rapidly in time with the harmonic time dependence $e^{-i\omega t}$

form.

In summary, the quasistatic dipole moment and scattered near-field are

$$\mathbf{p} = 4\pi a^3 \varepsilon_f \frac{\varepsilon_p - \varepsilon_f}{\varepsilon_p + 2\varepsilon_f} \mathbf{E}_0 \tag{2.19}$$

$$\mathbf{E}_{\text{sc}} = \frac{1}{4\pi\varepsilon_f r^3} \left(3\hat{\mathbf{r}}\hat{\mathbf{r}} - \mathbf{I}\right) \cdot \mathbf{p} \tag{2.20}$$

and the far-field scattered field is

$$\mathbf{E}_{\text{sc}} = \frac{k^2 e^{ikr}}{4\pi\varepsilon_f r} \left(\mathbf{I} - \hat{\mathbf{r}}\hat{\mathbf{r}}\right) \cdot \mathbf{p} \tag{2.21}$$

2.5 Absorption, Scattering, and Extinction Cross-Sections

Consider a control volume comprising two concentric spheres around an irradiated particle. How much energy is lost (i.e. attenuated) in this volume? If the particle were not present, all the power flowing into the control volume by the incident field flows out. With a particle present, the power flowing out is less than that flowing in. The attenuated power P_{ext} is the sum of the power absorbed P_{abs} by the particle and the power scattered P_{sc} by the particle. The power flux at any point is given by the time-averaged Poynting vector $\text{Re}[\mathbf{E} \times \mathbf{H}^*]/2$. By integrating the normal component of the Poynting vector over the surface S of the particle, we obtain

$$P_{\text{abs}} = \frac{1}{2}\text{Re} \int_S dS\, \mathbf{E} \cdot (\hat{\mathbf{n}} \times \mathbf{H}^*)\,, \quad P_{\text{sc}} = -\frac{1}{2}\text{Re} \int_S dS\, \mathbf{E}_{\text{sc}} \cdot (\hat{\mathbf{n}} \times \mathbf{H}_{\text{sc}}^*)\,. \tag{2.22}$$

The absorbed power involves the total field $\mathbf{E}$ while the scattered power involves only the scattered field $\mathbf{E}_{\text{sc}}$. The absorbed power uses the $-\hat{\mathbf{n}}$ component of the Poynting vector (the power flowing *into* the particle) while the scattered power uses $\hat{\mathbf{n}}$ (the power scattered *out* of the particle). Note that, because there are no "sources" in the control volume, the integral of the scattered Poynting vector over any spherical surface is the same, so both integrals can be evaluated at the particle surface. We've also applied the vector triple product identity $\mathbf{n} \cdot (\mathbf{E} \times \mathbf{H}*) = -\mathbf{E} \cdot (\hat{\mathbf{n}} \times \mathbf{H}^*)$. With $\mathbf{E} = \mathbf{E}_{\text{inc}} + \mathbf{E}_{\text{sc}}$ and realizing that the incident field alone has no power attenuation, the attenuated power is

$$P_{\text{ext}} = \frac{1}{2}\text{Re} \int_S dS \left(\mathbf{E}_{\text{inc}} \cdot (\hat{\mathbf{n}} \times \mathbf{H}_{\text{sc}}^*) + \mathbf{E}_{\text{sc}} \cdot (\hat{\mathbf{n}} \times \mathbf{H}_{\text{inc}}^*)\right). \tag{2.23}$$

Though we can use the quasistatic dipole expression, we have to leave the quasistatic limit for the scattered near-field and use the full non-quasistatic expression for $\mathbf{E}_{\text{sc}}$. Substituting this into the attenuated power integral leads to a simple expression for the total attenuated power in terms of the induced dipole moment

$$P_{\text{ext}} = \frac{k}{2\sqrt{\mu_f \varepsilon_f}} \text{Im}\left[\mathbf{p} \cdot \mathbf{E}_0\right] \tag{2.24}$$

Finally, the extinction cross-section is the power attenuated divided by the incident power flux $\sqrt{\varepsilon_f/\mu_f} E_0^2/2$

$$\sigma_{\text{ext}} = \frac{k}{\varepsilon_f E_0^2} \text{Im}\left[\langle \mathbf{p} \rangle \cdot \mathbf{E}_0\right] \tag{2.25}$$

which has units of area and is independent E_0. For a collection of nanoparticles, $\mathbf{p}$ is simply replaced by the (particle) average dipole $\langle \mathbf{p} \rangle = N^{-1} \sum_i \mathbf{p}_i$.

2.6 Coupled Dipole Methods

In collections of many particles, each particle is polarized not only by the incident field but also by the fields scattered by the other particles

$$\mathbf{p}_i = 4\pi a^3 \varepsilon_f \alpha \left(\mathbf{E}_0 + \sum_{j \neq i} \mathbf{E}_{\mathrm{sc},i} \right) \tag{2.26}$$

where the dipole "polarizability" is

$$\alpha = \frac{\varepsilon_p - \varepsilon_f}{\varepsilon_p + 2\varepsilon_f} \tag{2.27}$$

and the scattered field is

$$\mathbf{E}_{\mathrm{sc},j} = \frac{1}{4\pi\varepsilon_f r^3} \left(3\hat{\mathbf{r}}\hat{\mathbf{r}} - \mathbf{I} \right) \cdot \mathbf{p}_j \tag{2.28}$$

with $\mathbf{r} = \mathbf{x} - \mathbf{x}_j$. These expressions assume the quasistatic limit. The dipole moments are all coupled together, so we must solve a linear system of equations for the unknown dipoles simultaneously

$$\begin{bmatrix} \mathbf{E}_0 \\ \mathbf{E}_0 \\ \vdots \end{bmatrix} = \begin{bmatrix} \mathbf{M}_{11} & \mathbf{M}_{12} & \cdots \\ \mathbf{M}_{21} & \mathbf{M}_{22} & \cdots \\ \vdots & \vdots & \ddots \end{bmatrix} \cdot \begin{bmatrix} \mathbf{p}_1 \\ \mathbf{p}_2 \\ \vdots \end{bmatrix} \tag{2.29}$$

The $\mathbf{M}_{ij}$ are matrices that encode the field that particle i feels due to the dipole moment of particle j,

$$\mathbf{M}_{ij} = \begin{cases} \dfrac{1}{4\pi\varepsilon_f r^3} \left(\mathbf{I} - 3\hat{\mathbf{r}}\hat{\mathbf{r}} \right) & i \neq j \\ \dfrac{1}{4\pi a^3 \varepsilon_f \alpha} \mathbf{I} & i = j \end{cases} \tag{2.30}$$

where now $\mathbf{r} \equiv \mathbf{x}_i - \mathbf{x}_j$. It's convenient to represent this with the compact notation

$$\mathscr{E}_0 = \mathscr{M} \cdot \mathscr{P} \tag{2.31}$$

where $\mathscr{E}_0 = [\mathbf{E}_0, \ldots, \mathbf{E}_0]^T$ is incident electric field repeated N times, $\mathscr{P} = [\mathbf{p}_1, \ldots, \mathbf{p}_N]^T$ is the list of particle dipoles, $\mathscr{M}$ is a tensor whose ij^{th} block is $\mathbf{M}_{ij}$, and the T superscript indicates transposition. In analogy to electrostatics, $\mathscr{M}$ is called the "grand potential matrix" as it yields the electric potential and its derivatives (i.e. electric field) from the charge multipole moments (i.e. dipoles). We solve for the unknown dipoles by inverting $\mathscr{M}$

$$\mathscr{P} = \mathscr{C} \cdot \mathscr{E}_0, \quad \mathscr{C} = \mathscr{M}^{-1} \tag{2.32}$$

Again by analogy to electrostatics, $\mathscr{C}$ is called the "grand capacitance tensor". The average dipole is then

$$\langle \mathbf{p} \rangle = \mathbf{C} \cdot \mathbf{E}_0 \tag{2.33}$$

where $\mathbf{C} = \sum_{ij} C_{ij}/N$ and C_{ij} is the ij^{th} block of $\mathscr{C}$. Because each particle has, in general, a different dipole spectrum $\mathbf{p}_i(\omega)$, it is convenient to decompose the extinction cross-section[3] σ into contributions from each individual nanoparticle

$$\sigma(\omega) = \frac{1}{N}\sum_i \sigma_i(\omega), \quad \sigma_i(\omega) = \frac{3Z\omega}{4\pi a^3 E_0^2}\,\mathrm{Im}[\mathbf{p}_i(\omega)\cdot\mathbf{E}_0] \tag{2.34}$$

Note that now, σ and σ_i are the extinction cross-section per nanoparticle volume, with dimensions of 1/length. Because each $\sigma_i(\omega)$ is a spectrum, we can extract descriptor like resonance peak location, peak hight, and full width at half maximum (FWHM) for each nanoparticle in addition to the descriptors for the ensemble averaged spectrum. For example the ensemble resonance frequency, ω_{res}, and the resonance frequency of nanoparticle i, $\omega_{\text{res},i}$, can be defined as

$$\omega_{\text{res}} = \text{argmax}\,\sigma(\omega) \qquad \omega_{\text{res},i} = \text{argmax}\,\sigma(\omega_i) \tag{2.35}$$

2.7 The Mutual Polarization Method (MPM)

Constructing the large $3N$-by-$3N$ $\mathscr{M}$ matrix explicitly takes $O(N^2)$ operations and inverting it takes $O(N^3)$ operations, both of which are prohibitively expensive. Instead, we can use an iterative scheme like GMRES to solve the system of equations approximately. The cost now scales with the number of iterations multiplied by the time it takes to compute the matrix/vector dot product on the right side of (2.29). The dot product can be computed rapidly using a spectrally-accurate Ewald summation in $O(N(\log N)^n)$ time, where $n < 1$.

One major challenge is that fast iterative solvers like GMRES require $\mathscr{M}$ to be positive definite[4] to guarantee convergence. When $\mathscr{M}$ is given by (2.30), it is not guaranteed to be positive definite when particles overlap ($r < a_i + a_j$). Unfortunately, particle overlaps are common in dynamic simulations, which cannot model true hard interactions. We could assign particles a smaller radius for the electric dipole calculations so that no pairs are overlapping, but now this radius is different than the thermodynamic radius used to construct the configuration. This changes the effective volume fraction and places particle surfaces farther apart than expected, both of which have big implications for the optical properties. Instead, a regularization can be applied to overlapping pairs so that $\mathscr{M}$ is guaranteed to be positive definite in the $\omega \to 0$ limit. One such regularization for a triply-periodic system is

$$\mathbf{M}_{ij} = \frac{3\delta_{ij}\mathbf{I}}{4\pi a_i^3(\varepsilon_p - \varepsilon_f)} + \frac{9}{a_i a_j \varepsilon_f V}\sum_j \sum_{\mathbf{q}\neq 0} \frac{e^{i\mathbf{q}\cdot(\mathbf{x}_i - \mathbf{x}_j)}}{q^2} j_1(qa_i) j_1(qa_j)\hat{\mathbf{q}}\hat{\mathbf{q}} \tag{2.36}$$

which is written as a sum in reciprocal space over wavevectors[5] $\mathbf{q} \in 2\pi[n_x/L_x, n_y/L_y, n_z/L_z]$ for integers n_i. L_i are the periodic box lengths, $V = L_x L_y L_z$ is the system volume, and δ_{ij} is the Kronecker-δ function. (2.36) is equivalent to (2.30) when particles are non-overlapping ($r \geq a_i + a_j$), but has a different form for overlapping particles ($r < a_i + a_j$), ensuring $\mathscr{M}$ is *always* positive definite

[3] we are now dropping the "ext" subscript

[4] Because the diagonal entries of $\mathscr{M}$ are complex, $\mathscr{M}$ is generally never positive definite. What we mean here is that $\mathscr{M}$ should be positive definite in the electrostatic limit of $\omega = 0$. Else, convergence at all ω can be extremely poor and important physical properties, like the Kramers-Kronig relations, are not satisfied.

[5] unrelated to the wavevector $\mathbf{k}$ of incident light

and that (2.29) can be solved iteratively. This choice of regularization plus the particular procedure for Ewald summation defines the "mutual polarization method" (MPM), which we use for all optical simulations in this work.

2.8 Models for the Dielectric Function

We'll assume that each nanoparticle i has a dielectric function ε_i described by the Drude model

$$\varepsilon_i(\omega) = \varepsilon_{\infty,i} - \frac{\varepsilon_0 \omega_{p,i}^2}{\omega^2 + i\gamma_i \omega} \tag{2.37}$$

$\omega_{p,i}$ is the plasma frequency, γ_i is the free electron[6] damping coefficient, and $\varepsilon_{\infty,i}$ is the high-frequency permittivity. The Drude model describes only the plasmon mode of metallic materials and resonant features at higher frequencies are not considered, effectively lumped together in the single constant ε_∞.

[6] or, more generally, "charge carrier"

Chapter 3

Inverse Design of Optical Metamaterials Assembled from Plasmonic Nanoparticles

3.1 Abstract

Self-assembly of strongly coupled plasmonic nanoparticles is a scalable and promising route for producing optical metamaterials with emergent photonic properties. Understanding, controlling, and designing the light-matter interactions of these components is crucial to improving their performance. In this paper, we formulate optical metamaterials design as an inverse problem, where we first specify a target optical behavior and then use numerical optimization to autonomously discover self-assembled nanoparticle metamaterials possessing the desired features. We use a coupled dipole method for electromagnetic simulation to efficiently compute gradients of optical figures of merit with respect to nanoparticle position, size, and parameters of the dielectric function analytically for gradient-based iterative optimization. Our design framework rapidly iterates through candidate materials self-assembled from tens of thousands of nanoparticles, and specifies the position, size, dielectric properties, and other physical features of each nanoparticle within an optimal metamaterial, subject to arbitrary constraints on the choices of design parameters. We use our tool to perform simulated annealing optimization to propose nanoparticles metamaterials with optical features tunable over an enormous range. In particular, we have inverse designed nanoparticle metamaterials with: 1) tunable extinction spectra of complex lineshape and 2) electric near-field intensity with spatial profiles matching targeted patterns. By examining libraries of metamaterials with similar optical features, we can describe the key structure-property relations governing their optical responses.

3.2 Introduction

Optical metamaterials are heterogeneous, nanostructured materials with emergent light-matter interactions that are controlled by systematically tuning their microstructure.[25,53] They are engineered to have desirable photonic properties that are challenging to achieve with single-component materials, including negative effective refractive index, tunable structural color, and capability for multiplexing (i.e. responding selectively to) light of different wavelengths, polarizations, incident angles, and incident powers.[54–58] To contend with the enormous design space, inverse methods are emerging as a valuable tool for engineering optical metamaterials.[44,59–63] In an inverse approach (3.1), the input is a specific, "target" photonic property and numerical optimization and/or machine learning methods are used to discover the features of a metamaterial with the desired optical response. To date, development of inverse methods has focused mainly on "topology optimization" of 2D metasurfaces to determine the complex spatial features and arrangements of bicontinuous material domains.[44,64] The computationally-inverse-designed pattern can then be reproduced experimentally through top-down nanofabrication.[46,65–68] A majority of metasurfaces require electron-beam lithography to pattern their very small features, resulting in low throughput and high costs.[44,69] Photolithography enables higher-throughput production of lower-resolution

patterns, but the restriction on the minimum feature size results in degraded performance and less tunability.[70–72]

The focus of this paper is to develop computational inverse methods for *nanoparticle-based* metasurfaces. Controlled self-assembly of metal, doped semiconductor, and similar conductive nanoparticles is a powerful synthetic strategy to create nanophotonic soft materials on bulk scales.[73] Metal (e.g. gold, silver), doped semiconductor (e.g. tin-doped indium oxide (ITO)), and similar conductive materials have strong light-matter interactions due to their localized surface plasmon resonance (LSPR), i.e. collective oscillations of mobile electrons within the material.[9,12] For semiconductors in particular, the LSPR can be crafted by varying the dopant identity, dopant concentration, and dopant distribution throughout the nanoparticle.[9] Near the LSPR frequency, nanoparticles have large absorption and scattering efficiency and generate intense local electric field "hotspots" near their surfaces.[9,12] Taking advantage of these features, plasmonic nanoparticles are regularly used to enhance the signal of surface-enhanced Raman scattering (SERS) and surface-enhanced infrared absorption (SEIRA) to probe molecular absorption.[74,75] Plasmonic nanoparticles have also been incorporated into photovoltaic devices,[76] used in electrochromic devices,[77–79] and function as electrocatalysts.[80] Much of the energy absorbed via the LSPR mode is dissipated as heat, so plasmonic nanoparticles serve as localized and nanoscale heat sources.[81] On the other hand, doped metal oxide nanoparticles have large emission in the mid-IR and function as effective passive coolants for heat remediation via radiative cooling.[82,83] The plasmon modes of neighboring particles are highly coupled, and self-assembly is emerging as a powerful tool to modulate optical properties of plasmonic soft matter. Such "plasmonic metamaterials" display emergent properties, like perfect adsorption[84,85], epsilon-near-zero behavior[18], large refractive index,[86] and induced birefringence[87,88] and circular dichroism.[89] Plasmonic metamaterials can be tuned both at the single particle LSPR level and the assembled structure level, yielding a broad array of possible achievable properties.

Assembly of plasmonic nanoparticles has historically involved close-packed superlattice via deposition or solvent evaporation. The lattice structure is determined primarily via the core nanoparticle shape and the lattice spacing set by the length/density of the (typically organic) surface ligand shells. For example, three-dimensional truncated octahedral gold nanostructures such as Pt@Au nanoframes and Au@Pt nanoparticles self-assemble into close-packed 3D superlattices that generate a very strong and spatially uniform near-field electric field over large areas that enhanced surface-enhanced Raman spectroscopy (SERS) signals.[90] Gold octahedra have also been synthesized to assemble in a tip-to-tip configuration, aligning pointed tips towards neighboring NPs. This 'powder-like' assembly produces a highly-ordered nanoporous network with well-organized hot-spots and high hot-spot accessibility for small molecules.[91] Optimal plasmonic superlattice configurations have also been explored by examining how lattice parameters, local degree of order, and cluster architecture influence SERS efficiency.[92] Layers of ITO NPs with varying Sn doping concentrations, stacked onto germanium gold substrate, form a cavity structure, that is shown to selectively control distribution of electric field intensity within the assembly.[84] In another configuration, close-packed ITO NPs monolayer enhances near-field intensity into the gaps between the NPs, that enhances the spectral intensity of molecular vibrations placed there.[93] By varying the size and concentration of ITO NPs, their collective LSPR is tuned close to mid IR region to resonate with the molecular vibrations. These results show that tuning LSPR in plasmonic NPs allows for selectively near-field enhancement spatially and can assist in molecule detection.

In contrast to metamaterials comprising dielectric nanoparticles (e.g. photonic crystals), because plasmonic coupling does not require crystalline order, disordered assemblies display strong emergent

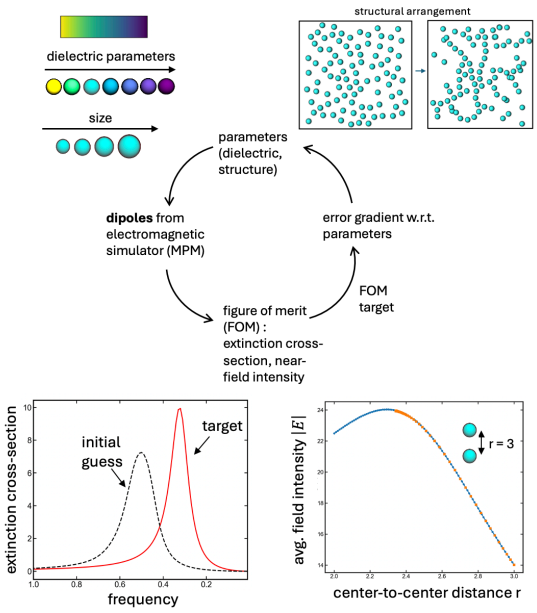

Figure 3.1: Inverse design framework schematic for designing nanoparticle-based optical metamaterials

plasmonic responses.[73,94,95] Over the last 20-30 years, many controlled self-assembly strategies have been developed using DNA-mediated assembly,[96] molecular linkages via dynamic covalent chemistry,[38,97,98] depletion attractions via non-absorbing polymer,[99–101] polymer bridging,[101] and coacervation of lower critical solution temperature (LCST) macromolecules (e.g. PNIPAM or elastin-like polypeptides).[102] These strategies have expanded the achievable structures, including disordered, percolated colloidal gels of tunable structure (e.g. fractal dimension) and clusters of controlled size, shape, and arrangement. Because these structures are lower density and can remain in solution, they enable reconfigurable materials with switchable photonic behavior controlled with chemical[97] or thermal stimuli.[102,103].

More recently, disordered NP assemblies like NP gel networks have also been investigated. Experimental techniques like small-angle X-ray scattering (SAXS), combined with computational modeling of light-matter interactions, have enabled detailed analysis of how local structural variations influence near-field and far-field responses of these ensembles.[31] For plasmonic metal NPs such as gold or silver, the discrete LSPR response of individual nanocrystals is lost upon gelation as particles tend to fuse into wire-like networks, erasing the isolated particle plasmonic signature.[104,105] To address this limitation, a study introduced a gelation approach of balancing short-range depletion attraction and long-range electrostatic repulsions, allowing disordered assemblies to form while preserving the LSPR of the individual NPs and overall morphology.[101]

Topology optimization approaches do not naturally extend to inverse design of nanoparticle self-assembly because we do not have direct control over the nanostructure. This issue has been partially solved through the development of computational inverse methods for "structure design", which discover the nanoparticle shape, surface features, and thermodynamic pair potentials that promote self-assembly of target structures.[106–108] Through inverse structure design, extremely complex structures have been self-assembled including single- and multicomponent colloidal crystals with

very large unit cells, quasicrystals, self-limiting colloidal clusters, and void geometries.[109–114] Unfortunately, *structure* design methods, do not easily extend to *optical* design, where the objective function explicitly incorporates a desired optical feature. A key difficulty is the prohibitive computational expense of electromagnetic simulations for large, self-assembled nanoparticle configurations, which must be performed hundreds or thousands of times during iterative optimization.[115,116] Common electromagnetic simulation methods like finite-difference time-domain (FDTD) or finite element method (FEM) are only feasible for $O(10)$ nanoparticles, which is insufficient for capturing the multi-length scale features of self-assembled configurations of $O(10^3)$–$O(10^6)$ nanoparticles. A second major difficulty is the challenge of computing gradients of an objective function with respect to physically tunable parameters of nanoparticles.

We model our configurations as ensemble of NPs composed of ITO or indium-tin oxide like dielectric functions, which is a plasmonic semiconductor formed by doping indium oxide (I_2O_3) with tin. They are plasmonic NPs whose optical properties can be controlled by tuning its LSPR in the near-infrared (NIR) region.[117–120] LSPR can be tuned by varying distribution of Sn dopant in indium oxide. Dopants can be localized to the core, distributed homogeneously, or segregated towards the surface. These distributions specifically influence LSPR characteristics such as linewidth, represented by the damping coefficient (γ) in the dielectric model used in this study.[121] For example, it is shown that when Sn is segregated on the surface of indium oxide, it leads to symmetric and narrow LSPR line shape.[122]

Additionally, bulk plasma frequency (ω_p) has been shown to increase with shell growth in core/shell model of indium oxide/ITO. ω_p is directly proportional to the free carrier concentration, which can be controlled by doping.[121] These tunable parameters present a design opportunity to tailor the LSPR response of individual NPs. Thus, in our model, tunability is incorporated by varying γ and ω_p of each NP continuously through the Drude dielectric function.

We use mutual polarization method (MPM) to compute the induced dipoles of each of these ITO-like NPs in the presence of incident field E_0. As reported previously, MPM is an electromagnetic simulation method utilizing coupled dipole approximations, where the optical response is determined from both the individual particle dipole and its interactions with dipoles of other NPs in the system.[38] MPM is fully differentiable, meaning that the resulting optical properties or objective functions are differentiable with respect to input parameters. These gradients can then be used to guide the optimization. The method is also reported to compute optical responses of large configurations and can account for triply periodic boundary conditions and particle overlaps. As discussed previously, MPM has been used to supplement experiments in the past for systems such as colloidal gels, metasurfaces, plasmonic superlattices.[18,31,38,98,123] Details about MPM are discussed further in methods Section 3.5.2.

The goal of this paper is to address this challenge by formulating and implementing a computational inverse framework for designing nanoparticle optical metamaterials utilizing nanoparticle self-assembly. The paper is organized as follows : first, we demonstrate optimization routine and MPM simulations for band-stop filter. We optimized a multi-layer configuration for dielectric parameters and radius for the optical figure of merit of extinction cross-section as the target spectra. We tuned the target spectra's bandwidth, bandcenter and modality and found optimized configurations for each of them using the same underlying principles. Next, we explored an alternate route to reach the target spectra by treating the nanoparticles as individual units instead of layers, allowing us to explicitly examine the dipole-dipole coupling between particles. The flexibility of this framework is also demonstrated for different band-stop targets.

In this paper, we also introduce an alternate optimization approach based on adjoint optimization within the inverse design framework to study near-field figure of merit of electric field intensity for plasmonic nanoparticles. We demonstrate this framework using a one-dimensional optimization problem for a spatial field pattern. Finally, we discuss how the resonance frequencies of individual particles and field polarization contribute to the resulting field patterns and outline directions for further exploration of the design space.

3.3 Results and Discussion

3.3.1 Overview of Optical Simulation

Optical simulation MPM is used to calculate induced dipoles ($\mathbf{p}_i$) in NPs by solving Maxwell's equations for a configuration irradiated with light $\mathbf{E_0}$. It is used to solve a linear system of equations in the quasistatic limit where radius of each NP (a_i) is much smaller than wavelength of light on system ($\lambda \gg a_i$), so that each dipole moment $\mathbf{p}_i$ is obtained by solving Laplace equation of electrostatics. We only retain the dipole truncation (p-truncation) in the moment expansion of each particle's total polarization response, while the quadrupole truncation (Q-truncation) and higher order terms are omitted.

Each $\mathbf{p}_i(\omega)$ is a complex vector that is a function of frequency. As a result, optical properties calculated using $\mathbf{p}_i(\omega)$ will be frequency-dependent. All NPs are described by the Drude model to give their electric permittivity also dependent on frequency $\varepsilon_p(\omega)$ through particle polarizability $\alpha_i(\omega)$. Section 3.5.1

3.3.2 Computing Gradients Analytically

We start by explaining the general features of our inverse design method for the case where the extinction cross-section $\sigma(\omega)$, defined in (3.16), is the figure of merit (FOM). This has a particularly simple form because of the similarity between extinction cross-section

$$\sigma \sim \frac{\omega}{N} \sum_i \mathrm{Im}\left[\mathbf{p}_i \cdot \mathbf{E}_0\right] \tag{3.1}$$

and the electrostatic energy of a collection of polarizable nanoparticles

$$U = \frac{1}{2} \sum_i \mathbf{p}_i \cdot \mathbf{E}_0 \tag{3.2}$$

$\nabla_{\mathbf{x}_i}\sigma$, the gradient of σ with respect to the position of particle i, is therefore related to $\mathbf{F}_i = -\nabla_{\mathbf{x}_i} U$, the electrostatic force on polarizable nanoparticles. There are numerous efficient numerical methods for computing $\mathbf{F}_i$.[124] Derivatives of σ with respect to other variables have similarly simple forms. For other optical FOMs, section 3.5.5 describes a more general approach. We highlight only key details here, a complete description is in the methods 3.5.4 and 3.5.5.

We choose a target extinction cross-section spectrum $\sigma_t(\omega)$ that we wish our metamaterial to display. We use the integrated squared error between the simulated $\sigma(\omega;\lambda)$ and the target $\sigma_t(\omega)$ as the objective function (or "loss")

$$f(\lambda) = \int_0^\infty d\omega \left(\sigma(\omega;\lambda) - \sigma_t(\omega)\right)^2 \tag{3.3}$$

Many other objective functions may be used, including spectral shape-matching metrics,[125] but our focus is not to determine the relative performance of different objective functions. The optimizer minimizes f by varying a set of M design parameters $\lambda = [\lambda_1, \ldots, \lambda_M]$. Each λ_k can be the position of a nanoparticle i $\mathbf{x}_i$, its radius a_i, or a parameter of its dielectric function $\varepsilon_i(\omega)$. When ε_i is represented with the Drude dielectric function, there are 3 "dielectric parameters", the plasma frequency $\omega_{p,i}$, damping coefficient γ_i, and high-frequency permittivity $\varepsilon_{\infty,i}$. If we can compute $\partial f/\partial\lambda = [\partial f/\partial\lambda_i, \ldots, \partial f/\partial\lambda_M]$ efficiently, we can utilize gradient-based schemes for the numerical optimization. Using the fact that $\not{p} = \mathscr{M}^{-1} \cdot \not{\mathscr{E}}_0$ and the matrix identity $\partial\mathscr{M}^{-1}/\partial\lambda_k = \mathscr{M}^{-1} \cdot \partial\mathscr{M}/\partial\lambda_k \cdot \mathscr{M}^{-1}$,

$$\frac{\partial\sigma}{\partial\lambda_k} = \frac{Z_f\omega}{E_0^2 N}\,\mathrm{Im}\left[\frac{\partial\not{p}}{\partial\lambda_k}\cdot\not{\mathscr{E}}_0\right] = -\frac{Z_f\omega}{E_0^2 N}\,\mathrm{Im}\left[\not{p}\cdot\frac{\partial\mathscr{M}}{\partial\lambda_k}\cdot\not{p}\right] \tag{3.4}$$

where $\not{p} = [\mathbf{p}_1, \ldots, \mathbf{p}_N]$, $\not{\mathscr{E}}_0 = [\mathbf{E}_0, \ldots, \mathbf{E}_0]$, and $\mathscr{M}$ is a block tensor whose ijth element is $\mathbf{M}_{ij}$. When the design variable is a particle position, $\lambda_k = \mathbf{x}_i$, then $\nabla_{\mathbf{x}_i}\sigma = -(2Z_f\omega/E_0^2 N)\,\mathrm{Im}\,\mathbf{F}_i$ is proportional to the electrostatic force on i. For each frequency ω, we compute $\nabla_{\mathbf{x}_i}\sigma$ for all nanoparticles simultaneously using 1 matrix/vector multiply via an Ewald summation method we developed for dynamic simulations of polarizable nanoparticles in electric and magnetic fields.[124] This calculation is typically negligible compared to the time to compute $\not{p}$, which requires a matrix/vector solve. When the design variable is a particle's radius, $\lambda_k = a_i$, or a particle's dielectric parameters, $\lambda_k = \omega_{p,i}$, γ_i, $\varepsilon_{\infty,i}$, only the ii block of $\partial\mathscr{M}/\partial\lambda_k$ is nonzero and $\partial\sigma/\partial\lambda_k = -(Z_f\omega/E_0^2 N)\,\mathrm{Im}\,[(\mathbf{p}_i\cdot\mathbf{p}_i)\partial M_{ii}/\partial\lambda_k]$. (Note $\mathbf{p}_i\cdot\mathbf{p}_i \neq |\mathbf{p}_i|^2$ for complex vectors). These derivatives require no significant computation.

With efficient calculation of these derivatives, we can then perform simulated annealing optimization, discussed in detail in Section 3.5.3. At each iteration of the optimization, design parameters are updated by a contribution in the gradient descent direction and by a stochastic contribution. The size of both the gradient descent step and the stochastic update can both be tuned.

3.3.3 Physicochemical Design of Quasi-2D Stratified Metasurfaces

We first demonstrate our optimization routine by crafting the extinction spectrum of a quasi-2D metasurface composed of 2D hexagonal layers of plasmonic nanoparticles, as shown in Fig. 3.2. Such metasurfaces have been assembled via sequential deposition of nanoparticle monolayers, where each monolayer comprises nanoparticles of different size and chemical composition.[84,85,126–129] Stratified metasurfaces can also be assembled from dispersions of multiple particle sizes via evaporative assembly with controlled evaporation rate.[130–134] We consider a 15-layer material of nanoparticles positions fixed to a face centered cubic (FCC) lattice oriented with the z-axis normal to the 111 plane. All particles within the same layer n are identical, with radius a_n and plasma frequency ω_n, but layers are different from one another. All particles have identical damping coefficient $\gamma = 0.1\omega_p^*$ and high-frequency permittivity $\varepsilon_\infty = \varepsilon_f$.

We use our optimization tool to determine the set of a_n and $\omega_{p,n}$ that results in a metasurface with a rectangular extinction cross-section, having equi-intensity extinction across a specific frequency interval and zero extinction outside of this interval (red curve in 3.2). This particular extinction spectrum is characteristic of a band-stop filter, which selectively blocks frequencies of light within the stopband and transmits all other frequencies. Krivina and coworkers created stopband materials from films containing a mixture of ITO nanoparticles of varying Sn-doping amounts whose individual LSPR frequencies spanned the stopband.[126] Motivated by this, we set the initial values of the plasma frequency $\omega_{p,n}$ of each layer to span our target stopband equally. Because the peak height h of the single-nanoparticle extinction spectrum scales as $h \sim \omega_p^2 a^3$, we set the initial values

of the radius of each layer to $a_n \sim \omega_{p,n}^{-2/3}$. We then use steepest descent optimization over 10000 iterations to update each a_n and $\omega_{p,n}$, i.e. a 30-dimensional optimization problem. Figure 3.2A shows the evolution of the metamaterial's extinction spectrum over the course of the optimization and Figure 3.2C shows the evolution of a_n and $\omega_{p,n}$. While the $a_n \sim \omega_{p,n}^{-2/3}$ scaling is mostly preserved in the final material, a_n and $\omega_{p,n}$ for most layers increase significantly over the course of the optimization, which results in a σ that is very close to σ_t. While the initial values of a_n and $\omega_{p,n}$ are initially spread out, the final values show clustering among the layers at the edges of the stopband, which all have around the same a_n and $\omega_{p,n}$. Note that, the clean ordering between layer number and a_n and ω_n values is a result of the ordering in the initial values by layer number. A.1 shows the results of the same optimization as 3.2, but with the same initial values randomized among the layers. This optimization results in the same $a_n \sim \omega_{p,n}^{-2/3}$ scaling and clustering a_n and ω_n at the stopband edges, but the values remain randomized among the layers. We interpret this as evidence that, while nanoparticles couple strongly within the same layer, there is no significant layer/layer plasmonic coupling. This is confirmed in A.2, where the ensemble spectrum nearly equal to the linear superposition of isolated layer spectra.

3.3.4 Tuning the Bandstop Functionality of Stratified Metasurfaces

Our inverse design scheme now provides a straightforward way to tune the extinction spectrum of a stratified metasurface simply by inputting different target extinction spectra. Figure 3.3 shows that inverse design is highly flexible in the spectral features it can reproduce. For the optimization in Fig. 3.2, the target σ_t has a single stopband of bandwidth $0.4\omega_p^*$ centered around a frequency of $0.5\omega_p^*$. Figure 3.3 shows examples where we use inverse design to tune the bandcenter frequency, the bandwidth, and the number of stopbands. In 3.3A, the metasurface has a bandcenter of $0.8\omega_p^*$ and a much larger bandwidth of $1.2\omega_p^*$. The metasurface in 3.3B has a bandcenter shifted to $0.8\omega_p^*$ with the same bandwidth of $0.4\omega_p^*$ as in 3.2. Finally in 3.3C, the metasurface has three distinct stopbands each of bandwidth $0.3\hat{\omega}$. In all cases, the optimizer converges to solutions where the resonant frequencies of individual layers, $\omega_{\text{res},n}$, span the stopbands and the radius scales as $a \sim \omega_{\text{res},i}$ (to ensure equi-intensity extinction (SI Fig. A.3)). This is nontrivial because as a increases, the area fraction of the layer increases which shifts $\omega_{\text{res},i}$.

3.3.5 Inverse Design of the Microstructure of 3D Metamaterials

In Figures 3.2–3.3, nanoparticle positions were fixed and we used inverse design to determine the size and dielectric parameters of the nanoparticles within the metasurfaces. Now, we fix the size and dielectric parameters and use inverse design to determine the nanoparticle positions within a metamaterial. We consider a monodisperse collection of N identical nanoparticles with the same a, ω_p, γ, and ε_∞ at a fixed volume fraction ϕ. We allow nanoparticles to take any position $\mathbf{x}$ in a cubic, triply-periodic box that does not overlap with another nanoparticle. For N nanoparticles, this corresponds to a $3N$-dimensional optimization problem as the optimizer searches for the configuration with an extinction cross-section closest to the target.

Figure 3.4 shows an optimization at $\phi = 0.10$ for a bandstop extinction spectrum with bandcenter $\Omega = 0.5\hat{\omega}$ and bandwidth $W = 0.4\hat{\omega}$, the same target as in 3.4. We initialize the nanoparticles to random, nonoverlapping positions (Fig. 3.4B). This configuration has a single extinction peak with a Lorentzian-like lineshape (dark blue in Fig. 3.4A), characteristic of the LSPR of Drude nanoparticles. Over many iterations, the optimizer evolves the nanoparticle configurations according to the simulated annealing scheme Section 3.5.3, and the extinction spectrum approaches the target. The final configuration (Fig. 3.4C) has a $\sigma(\omega)$ that is very close to the target. Compared to the

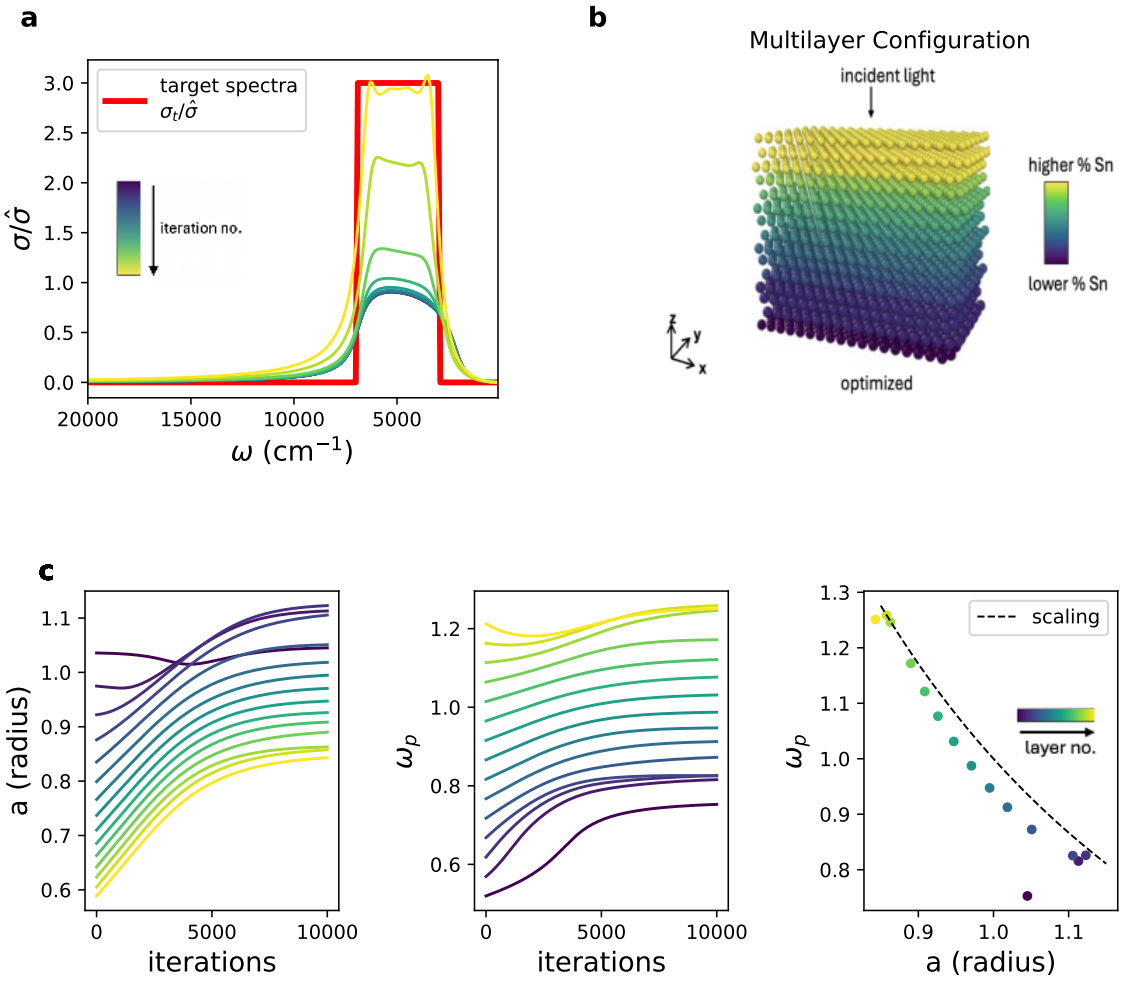

Figure 3.2: Inverse design of a stratified plasmonic metasturface. $\gamma = 0.1\omega_p^*$ and $\varepsilon_\infty = \varepsilon_f$ are fixed for all nanoparticles and the optimizer updates the radius a and plasma frequency ω_p of each layer. **A:** Evolution of the extinction cross-section σ of the metasurface as a function of incident frequency ω over optimization iterations (colors) The target spectrum is in red. **B:** Snapshot of the final metasurface configuration, with each nanoparticle colored by its ω_p. **C:** a and ω_p for each layer (colors) as a function of optimization iteration and the final set of $(a, omega_p)$ plotted together. Dashed line indicates $a \sim \omega_p^{-2/3}$ scaling. Quantities are nondimensionalized by $\omega_p^* = \sqrt{\varepsilon_0/\varepsilon_f}\omega_p$ and $\hat{\sigma} = \sqrt{\varepsilon_f \mu_f}\omega_p^*$.

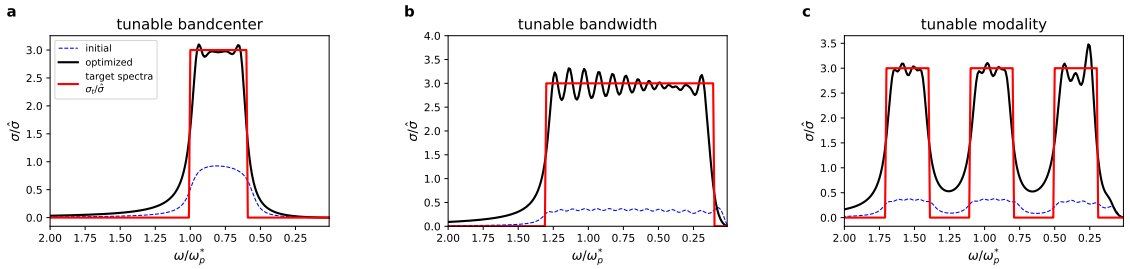

Figure 3.3: Tuning the extinction cross-section σ of stratified plasmonic metasurfaces. Panels show the target extinction (red), the metasurface extinction for initial values of a_n and $\omega_{p,n}$ (blue), and the metasurface extinction for the final optimized a_n and $\omega_{p,n}$ (black). The target spectra are **A:** bandcenter $\Omega = 0.8\hat{\omega}$ and bandwidth $W = 0.4\hat{\omega}$; **B:** bandcenter $\Omega = 0.8\hat{\omega}$ and bandwidth $W = 1.2\hat{\omega}$; **C:** three stopbands of bandwidth $W = 0.3\hat{\omega}$ and bandcenters $\Omega = 0.35,\ 0.95,\ 1.55\hat{\omega}$. All nanoparticles have fixed $\gamma = 0.1\hat{\omega}$ and $\varepsilon_\infty = \varepsilon_f$. The nondimensionalization is $\hat{\omega} = \sqrt{\varepsilon_0/\varepsilon_f}\,\omega_{p,0}$ and $\hat{\sigma} = \sqrt{\varepsilon_f \mu_f}\hat{\omega}$.

well-dispersed initial configuration (Fig. 3.4B), nanoparticles in the final configuration (Fig. 3.4C) arrange in aggregated, chain-like structures.

We repeat this optimization for the same target σ_t at several different volume fractions between $\phi = 0.05$ and 0.40. Though ϕ spans almost an entire order of magnitude, Figure 3.5A shows that, with inverse design, we can construct metamaterial configurations possessing the target spectrum. This is not typical behavior for suspensions of plasmonic nanoparticles. We have previously shown that the extinction spectrum of hard sphere and sticky sphere colloidal liquids and colloidal gels is very sensitive to ϕ and that increasing ϕ results in significant redshift of σ.[31] Because inverse design guarantees that the metamaterials at each ϕ possess nearly identical extinction spectra, Figure 3.5 demonstrates that such a redshift is not universal. There are arrangements of nanoparticles at essentially any ϕ for which σ is nearly independent of *phi*. Presumably then, nanoparticles arrange themselves to counteract the natural tendency to redshift with increasing ϕ.

We performed structural analysis to analyze if there are any common features between them that lead to this band-stop property. Through radial distribution function (RDF) and coordination no. for all ϕ, we did not find anything significant to report (Figure A.4).

The target σ_t here in Figure 3.5 is the same as the target for the stratified metasurface in Figure 3.2. For the stratified metasurface, the optimizer was able to craft the bandstop spectrum by distributing the resonance frequencies of each layer across the stopband. This was simple to do by directly adjusting the plasma frequency of the nanoparticles, which shifts their ω_{res}. Here for the 3D metamaterials, all nanoparticles have identical ω_p. However, the optimizer is still able to find configurations with resonance frequencies that span the stopband. To understand this, we compute the distribution of individual nanoparticle resonances $\omega_{\text{res},i}$. Although the overall extinction spectrum $\sigma = \sum_i \sigma_i/N$ is a many-bodied, emergent property of the nanoparticle ensemble, it can be decomposed into contributions from individual nanoparticles σ_i. We have previously shown that, although the ensemble σ may have a complex lineshape with multiple peaks, each individual σ_i can cleanly be assigned a single resonance frequency $\omega_{\text{res},i}$.[31] The probability density function $P(\omega_{\text{res}})$

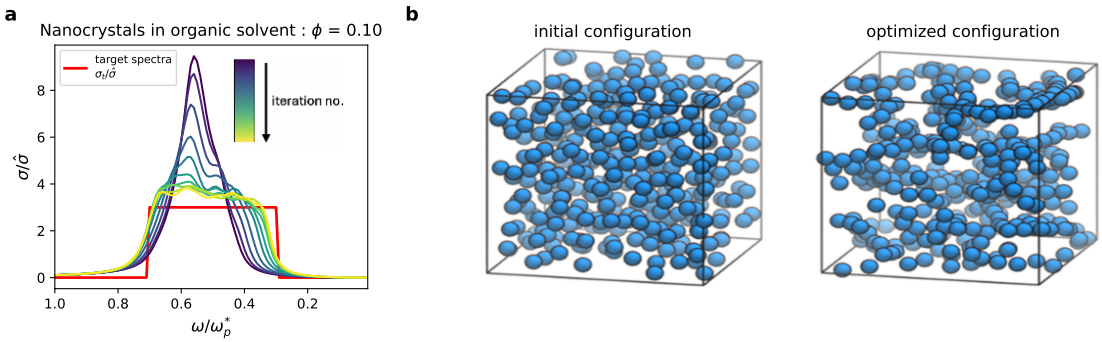

Figure 3.4: Inverse design of the microstructure of a 3D plasmonic metamaterial. **A:** Evolution of the extinction cross-section σ as a function of incident frequency ω over optimization iterations (colors). The target spectrum is in red. **B:** Snapshots of the initial and final nanoparticle configurations. All $N = 360$ nanoparticles have fixed radius, $\gamma = 0.1\omega_p^*$, and $\varepsilon_\infty = \varepsilon_f$ and the volume fraction is $\phi = 0.10$. Quantities are nondimensionalized by $\omega_p^* = \sqrt{\varepsilon_0/\varepsilon_f}\omega_p$ and $\hat{\sigma} = \sqrt{\varepsilon_f\mu_f}\omega_p^*$.

and the cumulative distribution function (CDF) $C(\omega_{\text{res}})$

$$C(\omega_{\text{res}}) = \int_{\omega_{\text{res}}}^{\infty} d\omega\, P(\omega) \tag{3.5}$$

of the set of ω_{res} are extremely useful for interpreting the ensemble extinction spectrum. Figure 3.5B shows the CDF for the final metamaterial structures at each ϕ, the CDF for the initial random configuration at $\phi = 0.10$, and the range of . Compared to a typical colloidal dispersion (i.e. the initial configuration for $\phi = 0.10$), which has a narrow distribution of ω_{res} in Figure 3.5B, the final CDFs of all ϕ have ω_{res} broadly distributed across the stopband interval. Almost no nanoparticles have a resonance frequency outside of the stopband. Therefore, we conclude that the optimizer is finding highly heterogeneous nanoparticle configurations with a diversity of local structural motifs, each of which promote a different resonance frequency.

For position design, we find that the magnitude of the noise term, T, in the simulated annealing scheme is a crucial hyperparameter. If $T = 0$, the nanoparticles arrest in a local minimum and the optimization is unable to converge sufficiently. If T is too large, nanoparticles simply diffuse around as hard spheres and make no progress to minimizing the objective function. Only for intermediate T does the optimization converge. We can draw a comparison to the temperature dependence of colloidal crystallization for attractive nanoparticles with Brownian motion. If T is large, the equilibrium phase is a colloidal fluid and nanoparticle do not assemble. If T is too small, nanoparticle will rapidly aggregate and arrest in disordered or defective configurations, often a percolated colloidal gel or an amorphous colloidal glass. Only for an intermediate range of T, the "crystallization slot", are the interparticle forces strong enough to promote self-assembly but weak enough to allow rearrangements and avoid arrest. The noise term in our simulated annealing scheme functions analogously to Brownian motion and thus T should be set to find the "slot" between Brownian-dominated and gradient-dominated displacements. In all of the inverse design calculations in Figures 3.4–3.6, we set $T = 0.2a_0$, though we stress that the best value depends on the step size η and the choice of objective function f.

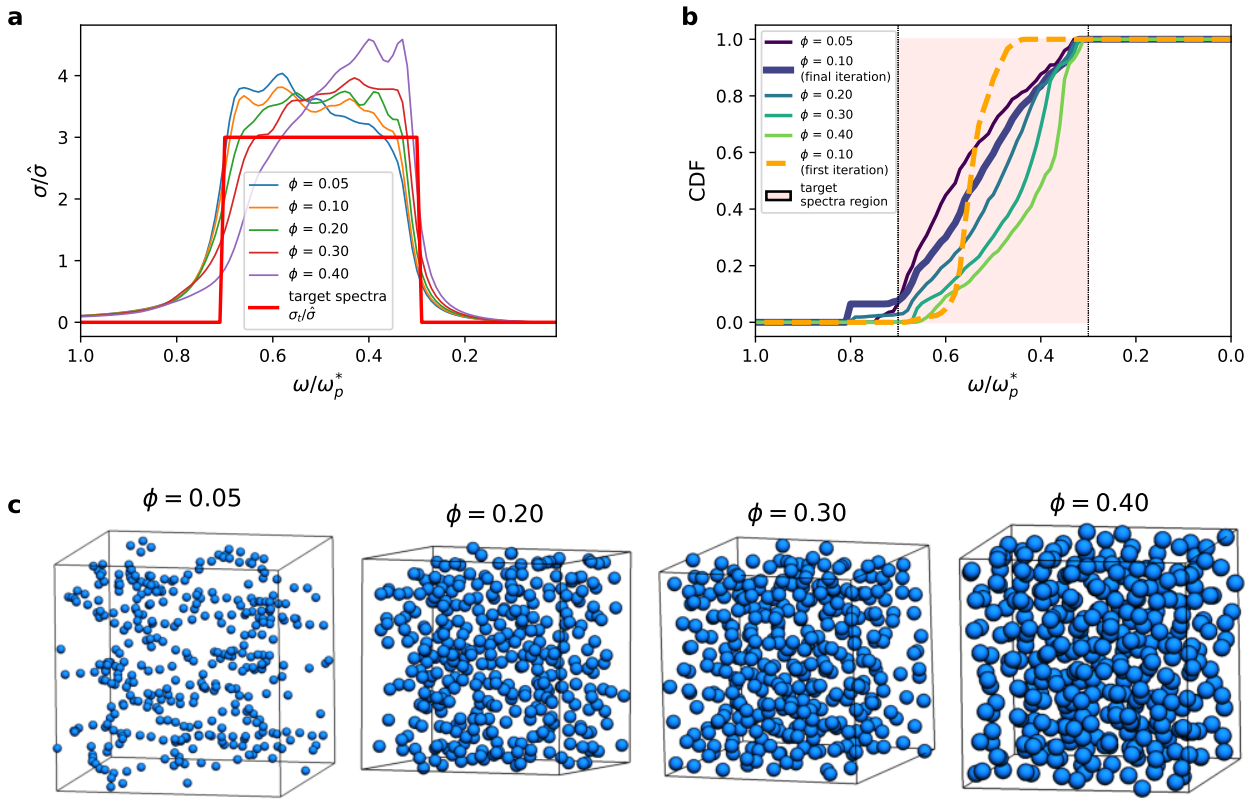

Figure 3.5: Inverse design of metamaterial structures across a range of volume fractions ϕ. **A:** The final optimized extinction cross-section σ as a function of incident frequency ω for each volume fraction ϕ (colors). The target spectrum is in red. **B:** The cumulative distribution function (CDF) of nanoparticle resonance frequencies $\omega_{\text{res},i}$ for each metamaterial from **A**. The shaded region indicates the range of frequencies in the stopband of the target spectrum. **C:** Snapshots of the final metamaterial configurations.

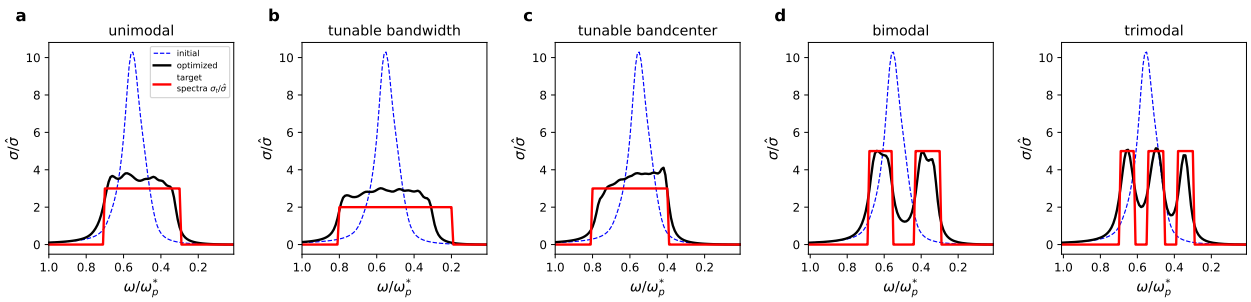

Figure 3.6: Tuning the extinction cross-section σ of 3D plasmonic metamaterials. Panels show the target extinction (red), the metamaterial extinction for initial configurations (blue), and the metamaterials extinction for the final optimized configuration (black). The target spectra are **A:** bandcenter $\Omega = 0.5\omega_p^*$ and bandwidth $W = 0.4\omega_p^*$; **B:** bandcenter $\Omega = 0.6\omega_p^*$ and bandwidth $W = 0.4\omega_p^*$; **C:** bandcenter $\Omega = 0.5\omega_p^*$ and bandwidth $W = 0.6\omega_p^*$; **D:** two stopbands of bandwidth $W = 0.13\omega_p^*$ and bandcenters $\Omega = 0.365,\ 0.625\omega_p^*$; and **E:** three stopbands of bandwidth $W = 0.08\omega_p^*$ and bandcenters $\Omega = 0.34,\ 0.5,\ 0.66\omega_p^*$. All other system parameters are identical to those in Figure 3.4.

3.3.6 Tuning Bandstop Functionality of 3D Metamaterials

Similar to the design of dielectric parameters to tune the extinction spectra in Figure 3.3, we used our inverse tool to design the nanoparticle microstructure to tune bandcenter frequency, bandwidth, and number of stopbands of σ. Figure 3.6A repeats the optimization from Fig. 3.4 for a bandcenter $\Omega = 0.5\omega_p^*$ and bandwidth $W = 0.4\omega_p^*$. In Fig. 3.6B, we shift the target bandcenter to $\Omega = 0.6\omega_p^*$ and repeat the optimization, designing a new microstructure with a spectrum close to the new target. In Fig. 3.6C, we increase the bandwidth to $W = 0.6\omega_p^*$. The optimizer converges to a microstructure with a large bandwidth close to the target, though the metamaterial's extinction between $0.2\omega_p^* \leq \omega \leq 0.3\omega_p^*$ is far below the target. We hypothesize this is due to the difficulty in shifting the ω_{res} of any nanoparticle below $0.3\omega_p^*$. Fig. 3.6D shows a metamaterial designed to have two distinct stopbands, and Fig. 3.6E a metamaterial with three distinct stopbands. In both cases, the metamaterial's extinction closely matches the target spectra. Compared to the unimodal bandstop materials, in which the ω_{res} are distributed evenly over the stopbands, the bimodal and trimodal materials primarily have nanoparticles resonating only in the stopband intervals. Very few nanoparticles resonate in the intervals between the stopband (the passbands) and so the extinction in the passbands is small.

Figure 3.6 demonstrates that even monodisperse collections of plasmonic nanoparticles can display extraordinarily complex spectral properties. And, that we can use inverse design to systematically design and probe materials with exotic optical properties. Additionally, the results of Figures 3.2–3.6 demonstrate that both physicochemical design (of nanoparticle size and dielectric parameters) and structure design (of nanoparticle positions) can be leveraged to produced metamaterials with similar spectral functionality. We note that, although we have considered them separately here, the radius, dielectric parameters, and positions of all nanoparticles can be optimized simultaneously (a 7N-dimensional optimization) in our inverse design routine.

3.3.7 Inverse Design of the Near-field Intensity Spatial Profile

The inverse design framework extends naturally to other optical figures of merit, provided we can compute the derivative $\partial f/\partial\lambda$. This derivative is straightforward when extinction cross-section is the figure of merit because of its connection to the electrostatic force, but a bit of care is needed for other figures of merit. As derived in Section 3.5.5, the general form of the derivative of $f(\lambda, \mathscr{P}(\lambda))$, which may depend explicitly on a design variable λ and implicitly through the dipoles $\mathscr{P}(\lambda)$, is

$$\frac{df}{d\lambda_k} = \frac{\partial f}{\partial \lambda_k} - \frac{\partial f}{\partial \mathscr{P}} \cdot \mathscr{M}^{-1} \cdot \frac{d\mathscr{M}}{d\lambda_k} \cdot \mathscr{P} \tag{3.6}$$

Note that for $f = \sigma$, $\partial\sigma/\partial\lambda_k = 0$, $\partial\sigma/\partial\mathscr{P}'' \sim \mathscr{E}$, and the derivative reduces to (3.4). Because $\mathscr{M}$ is $3N$-by-$3N$ and N is generally very large, we do not construct either $\mathscr{M}$ or $\mathscr{M}^{-1}$ explicitly. Rather we compute the dot product of $\mathscr{M}^{-1} \cdot \mathscr{V}$ with a vector $\mathscr{V}$ iteratively, e.g. using GMRES. If $\mathscr{V} = d\mathscr{M}/d\lambda \cdot \mathscr{P}$ in (3.6), this requires a matrix/vector solve for each λ_k on every iterations, which is cost-prohibitive for many design variables (e.g. the $3N$ position components of all nanoparticles). Rather, we select $\mathscr{V} = df/d\mathscr{P}$ in (3.6), which requires only a single matrix/vector solve per iteration, independent of the number of λ_k. This approach to computing derivatives is termed an "adjoint method" or "adjoint optimization", though any gradient-based optimization scheme can employ adjoint calculations. Adjoint methods are the predominant strategy employed in topology optimization of optical metamaterials,[68,135–137] but have not been applied to nanoparticle-based metamaterials. A complete description of our adjoint approach is found in Section 3.5.5–Section 3.5.7.

We utilize the adjoint method to design $E(\mathbf{x}) = |\mathbf{E}(\mathbf{x})|$, the spatial profile of the electric field intensity around plasmonic nanoparticles (termed the "near-field"). We imagine a collection of nanoparticles confined in the $z = 0$ plane. For any configuration, the nanoparticles generate a near-field profile, which we calculate in the $z = 1$ plane just atop the nanoparticle surfaces. We choose a target profile $E_t(\mathbf{x})$ and then use inverse design to determine the nanoparticle configuration with an $E(\mathbf{x})$ that is closest to $E_t(\mathbf{x})$. We could still use the integrated squared error $\int d\mathbf{x}(E - E_t)^2$ as the objective function. However, this biases E towards specific values. In typical use cases, e.g. sensing via SERS or SEIRA, we seek to maximize E in certain locations and minimize it in others. We therefore use the more flexible objective function

$$f(\lambda) = \int d\mathbf{x}\, g(\mathbf{x})\, E(\mathbf{x}, \lambda), \qquad g(\mathbf{x}) = \begin{cases} -1, & \mathbf{x} \text{ in hot region} \\ 1, & \mathbf{x} \text{ in cold region} \end{cases} \tag{3.7}$$

which maximizes E in the "hot" regions and minimizes it in "cold" regions. The target spatial profile is therefore encoded entirely in the function $g(\mathbf{x})$. We choose a polka dot pattern for g comprising a square array of 16 circles of radius $4a$ at area fraction 0.05. We then use the inverse design optimizer to find the nanoparticle configuration maximizing E inside the polka dots and minimizing E in the interstices.

Figure 3.7 shows the results of this optimization. Because the nanoparticle dipole moments depend on both the frequency and the polarization state of incident light, so too does $E(\mathbf{x})$. Figure 3.7 therefore shows 4 optimizations performed at two different frequencies, above and below the isolated nanoparticle LSPR frequency $\approx 0.58\omega_p^*$, and two different polarizations, in-plane and out-of-plane. Though the nanoparticles localize to the polka dots, the optimization is highly nontrivial because plasmonic coupling changes the dipole magnitudes and resonance frequency of nanoparticles as they approach each other. For example, for x-polarized light (Fig. 3.7C–D), the nanoparticles

preferentially orient orthogonal to $\mathbf{E}_0$. For z-polarized light (Fig. 3.7A–B), the nanoparticles have no preferential alignment, consistent with the symmetry of the setup (there is no reason for the nanoparticles to break symmetry.) Additionally the magnitude of E in the hot spots are much larger for z-polarized light than x-polarized light. This is primarily a simple consequence of the fact that for an electic dipole, while both the poles and the equator are local maxima in field intensity, the pole intensity is double the equatorial intensity. While there are qualitative differences between the two polarizations, we do not observe significant differences in the optimized structures between the two frequencies. The E magnitudes are much larger for $\omega = 0.7\omega_p^*$ compared to $0.4\omega_p^*$. In all cases, the optimizer finds configurations that have very large E within the polka dots and very small E in the interstices.

3.4 Conclusion

In this paper, we developed an inverse framework for designing plasmonic nanoparticle metamaterials using gradient-based numerical optimization. We derived expressions for the derivatives of optical figures of merit with respect to nanoparticle radius, dielectric parameters, and position and explained how to rapidly compute them. We then used our inverse method to design a variety of 2D and 3D metamaterials with complex extinction spectra and electric field spatial profiles.

However, there remains the challenge of how to self-assemble the optimized structures output from our inverse design tool. In fact,

In other words, further investigation is needed into the interaction energies between the NPs and whether that supports the self-assembly into optimized configurations. A study has modeled this through a combination of pair potential functions that include Morse potential to capture particle attraction, Coulomb potential parametrized by screening parameter κ and charges q to account for electrostatic repulsions and spring bond potential to maintain the particles in place and prevent drifting.[138] Gradients with respect to these parameters can be computed via differentiability capability of JAX-MD[138,139]. Including the potential parameter optimization alongside the inverse design framework would allow to further explore the assembly-structure relationship.

This study exclusively uses linearly polarized light. The framework however can be extended to use circularly polarized light to explore chiroptical responses of the configurations. Chiral nanomaterials are well documented to be promising for several applications.[140,141] Additionally, certain plasmonic nanomaterials can exhibit chirality through different interactions with left-handed and right-handed circularly polarized light. Hence there is potential to extend this framework to design chiral plasmonic materials. Given how interpreting chiroptical responses is non-trivial,[140] utilizing this inverse design framework is promising to accelerate this understanding.

A further limitation of the current inverse design framework is that all optimization is performed using linearly polarized light at normal incidence to the configuration. In practice, common light source such as sunlight is unpolarized.[66] Additionally, polarizations maybe incident on the materials at various angles. As a result, the optical response from the framework would vary with polarizations and incidence angles. To account for it, modifications to the objective function and the MPM framework are needed to compute gradients during the optimization, such that the optical response is agnostic to the polarizations and their incidence angles. Incident angle agnostic materials can then be further investigated using different optical properties of reflectance and transmittance, that can then be optimized through the adjoint method.

Using this framework, we demonstrate how plasmonic NPs couple to maximize near-field intensity

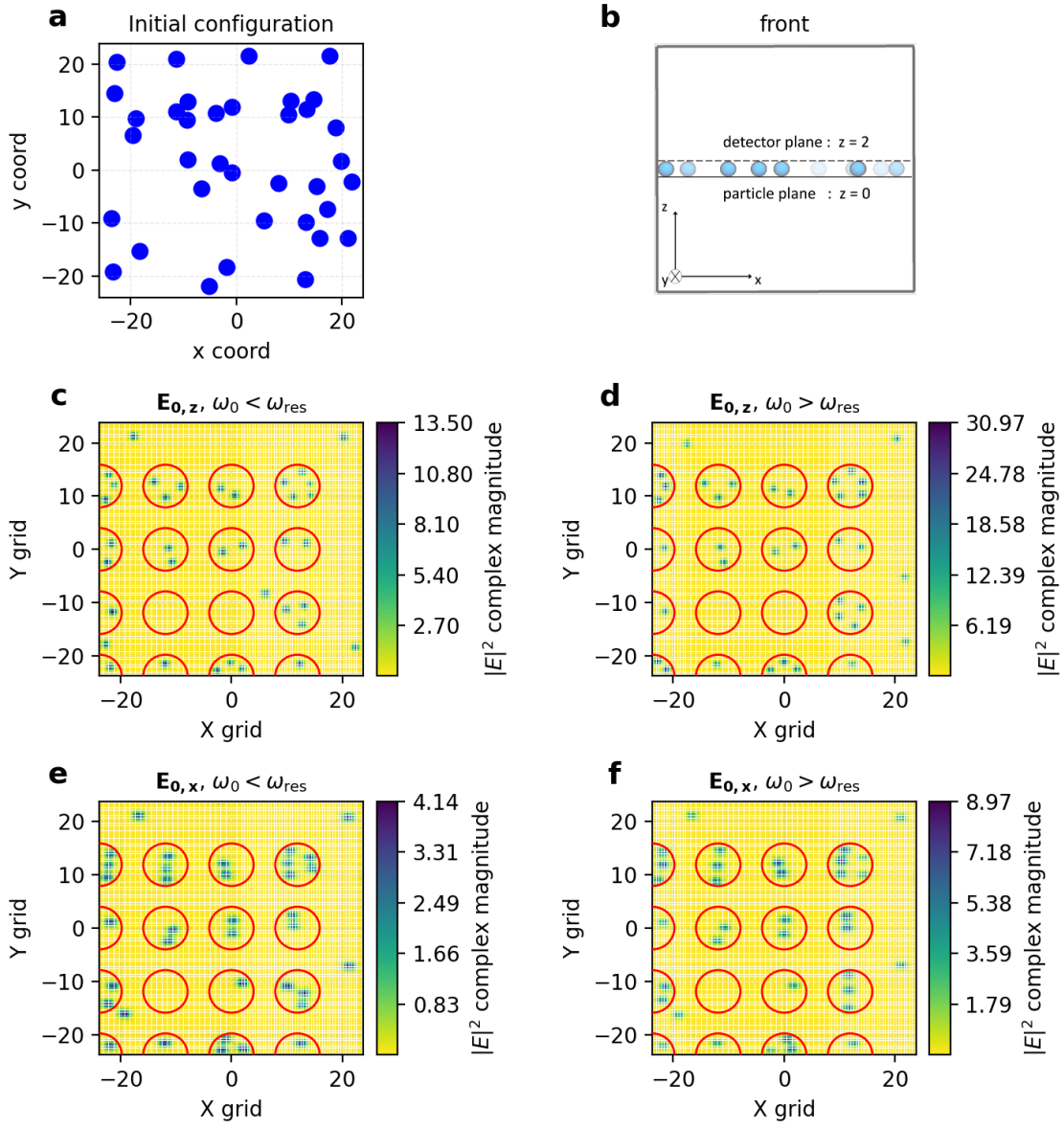

Figure 3.7: Inverse design of the near-field intensity E. All nanoparticles have $\gamma = 0.10\omega_p^*$ and $\varepsilon_\infty = \varepsilon_f$ and are at area fraction $\phi = 0.05$. The figure shows : a) Initial configuration in the xy plane; b) schematic of the particle and the detector planes : front view of the simulation box in the xz plane, with the 100×100 detector grid points $\mathbf{x}_E$ in the xy plane parallel to the particle plane; White boundaries indicate hot regions within which the optimizer tries to maximize E. Each panel indicates the final optimized near-field E-profile for **A:** $\mathbf{E}_0 = E_0\hat{\mathbf{e}}_z$ and $\omega = 0.4\omega_p^*$; **B:** $\mathbf{E}_0 = E_0\hat{\mathbf{e}}_z$ and $\omega = 0.7\omega_p^*$; **C:** $\mathbf{E}_0 = E_0\hat{\mathbf{e}}_x$ and $\omega = 0.4\omega_p^*$; and **D:** $\mathbf{E}_0 = E_0\hat{\mathbf{e}}_x$ and $\omega = 0.7\omega_p^*$.

within target regions defined by the polka dot pattern. We observe that field intensity is sensitive to polarization direction, and that at a probe frequency, larger than single NP ω_{res}, field intensity enhances around the target regions. Assembly of these NPs can be further investigated with different target patterns by modifying the field mask g_k. Optimizing positions for different target patterns will further show how NPs will assemble at the macroscale across the full particle plane and at the microscale of the target region.

While we are able to design configurations with thousands of NPs and parameters with large degrees of freedom with gradient-descent optimization, the current workflow only runs on CPUs. It is computationally demanding and time-consuming for larger system-size and gradient-descent even with simulated annealing scheme is prone to be stuck in a local minima.[42] This work can also be extended by using alternative optimization method such as Bayesian optimization.[142] Alternative NP geometries other than sphere, such as nanoshells, nanorods, while not correctly supported in MPM, can also be investigated as potential plasmonic NPs.

3.5 Methods

3.5.1 Dielectric Model

We describe the dielectric function of the nanoparticles using Drude model which solves for electric permittivity $\varepsilon_p(\omega)$. $\varepsilon_p(\omega)$ is identical for all nanoparticles

$$\varepsilon_p(\omega) = \varepsilon_\infty - \frac{\varepsilon_0 \omega_p^2}{\omega^2 + i\gamma\omega} \tag{3.8}$$

Key dielectric parameters that will be tested closely are ε_∞, which is the high-frequency permittivity, γ the damping coefficient, ω_p the plasma frequency in vacuum. ε_0 is vacuum permittivity and ε_f is the background permittivity. To account for difference between ε_0 and ε_f , ω_p is non-dimensionalized as $\omega_p^* = \omega_p \sqrt{\frac{\varepsilon_0}{\varepsilon_f}}$. Peak features of ω_{res}, h, W of an isolated nanoparticle can be calculated using Equation (3.9). These equations are important to give an initial guess for the parameters in our optimization routine.

$$\omega_{res} = \omega_p^* \sqrt{\frac{1}{2 + \frac{\varepsilon_\infty}{\varepsilon_f}}} \quad h = \frac{9\sqrt{\varepsilon_f \mu_f}\omega_p^{*2}}{\gamma(2 + \frac{\varepsilon_\infty}{\varepsilon_f})^2} \quad W = \gamma \tag{3.9}$$

3.5.2 Mutual Polarization Method for Optical Simulations

When the wavelength of incident light is much larger than the nanoparticle radius, solutions to Maxwell's equations for the electric field $\mathbf{E}(\mathbf{x})$ in the material can be inferred from the Laplace equation for electrostatics. In this quasistatic limit, the electric field (and its gradients) can be written as a sum of the incident field and scattered fields from multipole moments

$$\mathbf{E}(\mathbf{x}) = \mathbf{E}_0 + \frac{1}{4\pi\varepsilon_f} \sum_i \nabla\nabla \frac{1}{r_i} \cdot \mathbf{p}_i \tag{3.10}$$

where $\mathbf{r}_i = \mathbf{x} - \mathbf{x}_i$ is the position relative to the center of i, $r_i = |\mathbf{r}_i|$, and $\mathbf{p}_i$ is the currently unknown dipole moment of i. The particle moments are, in turn, induced by the local electric field

$$\mathbf{p} = 4\pi a^3 \varepsilon_f \alpha \mathbf{E}(\mathbf{x}), \quad \alpha = \frac{\varepsilon_p/\varepsilon_f - 1}{\varepsilon_p/\varepsilon_f + 2} \tag{3.11}$$

In the quasistatic limit considered here, the external field does not spatially vary and the external field gradient is zero, $\nabla \mathbf{E}_0 = 0$, though the local field gradient is nonzero, $\nabla \mathbf{E}(\mathbf{x}) \neq 0$. Though this induces quadrupole moments in each nanoparticle, quadrupoles and higher-order moments are neglected here. Equations Equation (3.10)-Equation (3.11) form a linear system of equations for the unknown dipoles in terms of the external field

$$\mathscr{E}_0 = \mathscr{M}_{Ep} \cdot \mathscr{p}. \tag{3.12}$$

where $\mathscr{p} \equiv [\mathbf{p}_1, \ldots, \mathbf{p}_N]^T$ is a $3N$-by-1 list of particle dipoles, $\mathscr{E}_0 \equiv [\mathbf{E}_0, \ldots, \mathbf{E}_0]^T$ is the incident field repeated N times, and $\mathscr{M}_{Ep}$ is a $3N$-by-$3N$ tensor that couples the external field gradient to the particle dipoles. In a triply-periodic geometry, we can express $\mathbf{M}_{Ep,ij}$, the ij block of $\mathscr{M}_{Ep}$, as

$$\mathbf{M}_{Ep,ij} = \frac{3\delta_{ij}\mathbf{I}}{4\pi a^3(\varepsilon_p - \varepsilon_f)} + \frac{9}{a^2 \varepsilon_f V} \sum_{\mathbf{q} \neq 0} \frac{e^{i\mathbf{q}\cdot\mathbf{r}_{ij}}}{q^2} j_1^2(qa) \hat{\mathbf{q}}\hat{\mathbf{q}} \tag{3.13}$$

where δ_{ij} is the Kronecker δ-function, j_ℓ is the spherical Bessel function of degree ℓ, and $V = L^3$. The sums are over wavevectors $\mathbf{q} = [2\pi q_1/L, 2\pi q_2/L, 2\pi q_3/L]$, where q_i are integers. While Equation (3.13) is consistent with Equation (3.10) for non-overlapping particles $r \geq 2a$, it contains a regularization term for overlapping particles $r < 2a$. This regularization guarantees that $\mathscr{M}_{Ep}$ is positive-definite for all possible configurations in the $\omega \to 0$ limit and ensures that $\mathscr{M}$ never becomes ill-conditioned.[38]

Inverting the matrix equation, we can write the dipoles in terms of the applied field

$$\mathscr{p} = \mathscr{C} \cdot \mathscr{E}_0, \quad \mathscr{C} = \mathscr{M}_{Ep}^{-1} \tag{3.14}$$

where $\mathscr{C}$ is a $3N$-by-$3N$ tensor with 3-by-3 blocks denoted $\mathbf{C}_{ij}$. We can also write the ensemble average dipole $\mathbf{p} \equiv \sum_i \mathbf{p}_i/N$ as a linear function of the applied field

$$\mathbf{p} = \mathbf{C} \cdot \mathbf{E}_0 \tag{3.15}$$

where $\mathbf{C} = \sum_{ij} \mathbf{C}_{ij}/N$ is the average $\mathbf{C}_{ij}$ tensor. The linear relation Equation (3.15) between dipoles and incident field always holds, but the accuracy of $\mathscr{C}$ and $\mathbf{C}$ increases as the level of moment truncation increases.

We do not compute $\mathscr{M}$ or $\mathscr{C}$ explicitly. Rather, we compute only matrix-vector products, e.g. $\mathscr{M} \cdot \mathscr{p}$, using a rapid spectrally-accurate Ewald method discussed elsewhere[38,143,144] and solve for the particle moments numerically using an iterative linear solver, GMRES. By solving for the dipoles induced by three orthogonal incident field polarizations $\mathbf{E}_0 = \hat{\mathbf{e}}_x$, $\hat{\mathbf{e}}_y$, and $\hat{\mathbf{e}}_z$, we construct the entire $\mathbf{C}$ tensor.

The effective extinction cross-section per nanoparticle volume, σ, of the nanoparticle ensemble is

$$\sigma(\omega) = \frac{1}{N} \sum_i \frac{3\sqrt{\mu_f}\omega}{4\pi a^3 \sqrt{\varepsilon_f} E_0^2} \operatorname{Im}\left[\mathbf{p}_i(\omega) \cdot \mathbf{E}_0\right] \equiv \frac{1}{N} \sum_i \sigma_i(\omega) \tag{3.16}$$

and can be written in terms of extinction contributions from each nanoparticle σ_i. Note that though σ_i is assigned to nanoparticle i, it is a collective quantity that is a function of the positions of all other nanoparticles. Both $\sigma(\omega)$ and $\sigma_i(\omega)$ are spectra, and we define an ensemble resonance frequency ω_{res} and individual particle resonance frequencies $\omega_{\text{res},i}$ as the frequency of maximum extinction cross-section. Resonant frequency distributions are constructed by binning $\omega_{\text{res},i}$ in bins of width $0.01\omega_p^*$.

$$\omega_{\text{res}} = \arg\max \sigma(\omega), \quad \omega_{\text{res,i}} = \arg\max \sigma_i(\omega) \tag{3.17}$$

True field $\mathbf{E}$ at a single point $\mathbf{x}_0$ is a sum of the incident field $\mathbf{E}_0$ and the scattered field $\mathbf{E}_{sc}$. Scattered field magnitude is much larger than the incident field magnitude ($\mathbf{E}_{sc} \gg \mathbf{E}_0$). Hence field is approximated as $\mathbf{E} \approx \mathbf{E}_{sc}$. Electric field at a single point from a nearby NP i is then represented as below

$$\mathbf{E}_{sc,i} = \frac{1}{4\pi\varepsilon_m \mathbf{r}_{ij}^3}(\mathbf{I} - 3\hat{\mathbf{r}}_{ij}\hat{\mathbf{r}}_{ij})\mathbf{p_1} \tag{3.18}$$

Contribution from multiple NPs (i) at the single point is the sum of $\mathbf{E}_{sc,i}$ represented as below

$$\mathbf{E} = \sum_i^N \mathbf{M}_i^{sc}\mathbf{p_i} \quad \mathbf{M}_i^{sc} = \frac{1}{4\pi\varepsilon_m \mathbf{r}_{ij}^3}(\mathbf{I} - 3\hat{\mathbf{r}}_{ij}\hat{\mathbf{r}}_{ij}) \tag{3.19}$$

Equation for $\mathbf{M}_i^{sc}$ comes from Equation (3.13). It represents the field at a single point due to dipole moment of the particles i. This is discussed further in Section 3.5.7.

MPM code is available at github.com/zeesherman/mutual-polarization

3.5.3 Optimization via Simulated Annealing

A key component of our inverse design optimization scheme is the design variables (θ). These include the dielectric parameters of the Drude model $\omega_p, \gamma, \varepsilon_\infty$ introduced in section Section 3.5.1.

The plasma frequency ω_p is bounded between 0.1 to ∞ and the particle radius a is constrained between 0.1 to 2. The choice of initial values for ω_p and a is discussed in section Section 3.3. The parameters γ and ε_∞ are fixed at 0.1 and 1 respectively. Additionally, particle positions are also included in the design space. The parameters are updated using a simple iterative scheme of steepest-descent gradient method with a defined step-size (η) to reach a target spectra from model spectra. $\nabla\Gamma$ is computed in the optimization routine

$$\theta_{i+1} = \theta_i - \eta\nabla\Gamma + \mathbf{W} \tag{3.20}$$

Equation (3.20) is a differential equation in which stochastic noise $\mathbf{W}$ is added. Each design variable (θ_i) is perturbed at every iteration by adding a random noise from a uniform distribution $\mathbf{W_i} \sim U(-\frac{T}{2}, \frac{T}{2})$, where T is an arbitrary value used to control the noise amplitude. Uniformly distributed noise is represented as

$$\langle \mathbf{W_i} \rangle = 0, \langle \mathbf{W_i W_j} \rangle = \alpha\mathbf{I}, \alpha = \frac{T^2}{12} \tag{3.21}$$

$\mathbf{I}$ in the Covariance term $\langle \mathbf{W_i W_j} \rangle$ indicates that noise is uncorrelated between parameters. Each component $\mathbf{W_i}$ is independently and identically distributed (i.i.d) with zero mean and variance α. The variance $\alpha = \frac{T^2}{12}$ follows directly from properties of the uniform distribution on $(-\frac{T}{2}, \frac{T}{2})$.

Addition of stochastic noise is to help prevent convergence to a local minima. This approach resembles simulated annealing, where perturbations allows the optimization to explore the design landscape broadly.

For dielectric design in Figure 3.2 and Figure 3.3, a step-size η of 0.0001/N is used, where N is the total no. of particles in the configuration. A step-size of 0.01 is used for updating particle positions in Figure 3.4 and Figure 3.5, while a step-size of 10 is used for adjoint optimization of near-field intensity in Figure 3.7.

3.5.4 Computing Gradients of Extinction Cross-Section

We want to generate a target spectra based on the desired application discussed earlier. This could be spectra for any optical property such as extinction, reflectance, near field intensity. We choose extinction cross-section per nanoparticle volume calculated from induced dipoles as the target spectra $\sigma_t(\omega)$.

Initial guess to the scheme is a model extinction spectra $\sigma(\omega, \chi, \lambda, a)$ which is a function of design variables $\theta \equiv (\chi, \lambda, a)$. $\chi = [(x_1, y_1, z_1), (x_2, y_2, z_2), ..., (x_N, y_N, z_N)]^T$ is the position coordinates of N nanoparticles and $\lambda = [\lambda_1, \lambda_2, ..., \lambda_N]^T$: is the dielectric parameters of each nanoparticle from the Drude model $(\omega_p, \gamma, \varepsilon_\infty)$ and a is the radius of each nanoparticle. We can vary the dielectric parameters continuously to access the material space.

With the design variables, we can calculate the model extinction using MPM. We can minimize the error between the model spectrum and target spectrum using integrated square error. Objective function is $\Gamma[\sigma(\omega;\theta), \sigma_t(\omega)]$.

$$\Gamma[\sigma(\omega;\theta), \sigma_t(\omega)] = \int_0^\infty d\omega(\sigma(\omega;\theta) - \sigma_t(\omega))^2 \tag{3.22}$$

We use a gradient-based minimization scheme, which involves calculating $\nabla\Gamma$ with respect to design parameters

$$\nabla\Gamma[\sigma(\omega;\theta), \sigma_t(\omega)] = 2\int_0^\infty d\omega(\sigma(\omega;\theta) - \sigma_t(\omega))\nabla\sigma \tag{3.23}$$

To calculate this, $\nabla\sigma$ needs to be computed. Substituting particles dipoles Equation (3.15) in Equation (3.16) for a single nanoparticle, we get

$$\nabla\sigma = \frac{3\sqrt{\mu}_f\omega}{4\pi a^3\sqrt{\varepsilon_f}E_0^2} Im\nabla\mathscr{M}_{\mathscr{E}_\mathscr{P}} : \mathscr{P}\mathscr{P} \tag{3.24}$$

To calculate $\nabla\mathbf{M}_{Ep,ij}$ with respect to dielectric parameters λ, we only consider the field gradient index i and equate the moment index j to i. This reduces the potential tensor to its diagonal components, M_{ii}, because the dielectric parameters appear exclusively in the i^{th} component of polarizability α_i (Equation (3.11)). In other words, if dielectric parameter λ of each particle can vary independently, derivative of $\mathscr{M}$ with respect to λ is only nonzero for the $\mathscr{M}$ block, which is an isotropic tensor. $\mathscr{M}$ is derived after expanding dipole moment Equation (3.11) and re-arranging for $\mathbf{E_0}$Equation (3.10).

$$M_{ii} = \frac{1}{4\pi a^3\varepsilon_f\alpha_i}\mathbf{I}, \frac{\partial\mathscr{M}}{\partial\lambda_i} = -\frac{3}{4\pi a^3\varepsilon_f\alpha_i}\frac{\partial\varepsilon_i}{\partial\lambda_i} \tag{3.25}$$

Here $\varepsilon_i(\omega)$ is the Drude dielectric function of particle i. The partial derivatives with respect to the

dielectric parameters $\omega_{p_i}, \gamma_i, \varepsilon_{\infty,i}$ are given by

$$\frac{\partial \varepsilon_i}{\partial \omega_{p_i}} = \frac{-2\omega_{p_i}}{\omega^2 + i\gamma_i\omega}, \frac{\partial \varepsilon_i}{\partial \gamma_i} = \frac{i\omega_{p_i}^2}{\omega(\omega + i\gamma_i)^2}, \frac{\partial \varepsilon_i}{\partial \varepsilon_{\infty,i}} = 1 \tag{3.26}$$

The gradient operator with respect to λ and radius (a), is therefore defined independently for each nanoparticle.

$$\nabla_{a,\lambda} = [\frac{\partial}{\partial a_1}, \frac{\partial}{\partial \omega_{p_1}}, \frac{\partial}{\partial \gamma_1}, \frac{\partial}{\partial \varepsilon_{\infty,1}}, \frac{\partial}{\partial a_2}, \frac{\partial}{\partial \omega_{p_2}}, \frac{\partial}{\partial \gamma_2}, \frac{\partial}{\partial \varepsilon_{\infty,2}}, \ldots, \frac{\partial}{\partial a_N}, \frac{\partial}{\partial \omega_{p_N}}, \frac{\partial}{\partial \gamma_N}, \frac{\partial}{\partial \varepsilon_{\infty,N}}]^T \tag{3.27}$$

Gradient of $\mathscr{M}$ with respect to particle positions, has been derived previously using the key relation $\nabla_{x_i}\mathscr{M}^- = (\nabla_{x_i}\mathscr{M}) : \mathscr{M}^-\mathscr{M}^-$.[124] The authors showed that $\nabla_{x_i}\mathscr{M} : \mathscr{P}\mathscr{P}$ is twice the electrostatic forces on the particles, which we can already compute efficiently. Hence using $\nabla\mathscr{M}$ we can compute $\nabla\Gamma$ for the optimization routine.

3.5.5 Computing Gradients of General Optical Figures of Merit via an Adjoint Method

To calculate gradient of the figure of merit (FOM) of extinction cross-section, $\nabla\sigma$ Equation (3.16), we needed only one matrix/vector solve to calculate the dipoles $\mathscr{P}$ since $\mathscr{M}^{-1}$ is paired with an $\mathscr{E}_0$. Meaning we solve the system of linear equations to compute dipoles once instead of explicitly calculating $\mathscr{M}^{-1}$.

However to calculate error metric of FOM of near-field intensity $|\mathbf{E}|^2$, $\mathscr{M}^{-1}$ is unpaired in gradient $\nabla\Gamma$. This requires an impractical computational burden to handle. To calculate we used adjoint-method, which formulates the problem so that only two matrix/vector solves are required. One is the forward matrix-vector solve same as extinction cross-section, where we compute for dipoles $\mathscr{P}$. Second matrix-vector solve is for an adjoint variable Λ defined as

$$\frac{\partial f}{\partial \mathscr{P}} = \mathscr{M} \cdot \Lambda$$

A general objective function that depends on parameters λ and NP dipoles $\mathscr{P}$ is defined as

$$f(\lambda, \mathscr{P}(\lambda))$$

To calculate error metric for optimization, we need total derivative of f w.r.t. λ. Using chain rule,

$$\frac{df}{d\lambda} = \frac{\partial f}{\partial \lambda} + \frac{\partial f}{\partial \mathscr{P}} \cdot \frac{d\mathscr{P}}{d\lambda}$$

Substituting for $\mathscr{P} = \mathscr{M}^{-1} \cdot \mathscr{E}_0$

$$\frac{df}{d\lambda} = \frac{\partial f}{\partial \lambda} - \frac{\partial f}{\partial \mathscr{P}} \cdot \mathscr{M}^{-1} \cdot \frac{d\mathscr{M}}{d\lambda} \cdot \mathscr{P}$$

For a general objective function, calculating $\mathscr{M}^{-1}$ explicitly is expensive, scaling as $O(N^3)$ where N is no. of particles. Instead of calculating it directly, we compute its action on a vector $\mathbf{v}$ by solving a linear system. We make sure that $\mathbf{v}$ isn't dependent on λ. If it was dependent say in $\frac{d\mathscr{M}}{d\lambda}$, it would scale with N and be just as expensive to compute. We introduce an adjoint variable to represent this dot product as $\Lambda = \frac{\partial f}{\partial \mathscr{P}} \cdot \mathscr{M}^{-1}$. We then use a matrix/vector solve to solve for Λ and

eventually calculate $\frac{df}{d\lambda}$ needed to compute error gradient.

$$\frac{df}{d\lambda} = \frac{\partial f}{\partial \lambda} - \Lambda \cdot \frac{d\mathscr{M}}{d\lambda} \cdot \mathscr{P} \tag{3.28}$$

3.5.6 Complex Differentiability in Computing Gradients of General Optical Figures of Merit

Since $\mathscr{P}$ is a complex variable$\mathscr{P} = \mathscr{P}^{'} + i\mathscr{P}^{''}$, $f(\mathscr{P})$ is also complex. For a complex derivative $f'(\mathscr{P})$ to exist, real and imaginary parts of $\mathscr{P}$ must satisfy Cauchy-Riemann equations. However, the complex conjugate function $f(\mathscr{P}) = \mathscr{P}^*$ is not differentiable with respect to $\mathscr{P}$ according to the Cauchy-Riemann equations. To avoid this, instead of treating the complex variable $\mathscr{P}$ as a single independent variable of f, we treat its real $\mathscr{P}^{'}$ and $\mathscr{P}^{''}$ imaginary components, as independent variables. The objective function is theCrefore written as

$$f = f(\lambda, \mathscr{P}^{'}, \mathscr{P}^{''})$$

$\mathscr{P}^{'}$ and $\mathscr{P}^{''}$ are both real and continuously differentiable variables that can be treated independently to avoid any issues with complex differentiability. Expanding the total derivative using the chain rule gives

$$\frac{df}{d\lambda} = \frac{\partial f}{\partial \lambda} + \frac{\partial f}{\partial \mathscr{P}\prime} \cdot \frac{d\mathscr{P}\prime}{d\lambda} + \frac{\partial f}{\partial \mathscr{P}\prime\prime} \cdot \frac{d\mathscr{P}\prime\prime}{d\lambda} \tag{3.29}$$

To evaluate this further, we use chain rule from Section 3.5.5

$$\frac{d\mathscr{P}}{d\lambda} = -\mathscr{M}^{-1} \cdot \frac{d\mathscr{M}}{d\lambda} \cdot \mathscr{P}$$

Since

$$\frac{d\mathscr{P}}{d\lambda} = \frac{d\mathscr{P}\prime}{d\lambda} + i\frac{d\mathscr{P}\prime\prime}{d\lambda}$$

The derivatives of the real and imaginary part can be obtained as

$$\frac{d\mathscr{P}\prime}{d\lambda} = \mathrm{Re}\left[-\mathscr{M}^{-1} \cdot \frac{d\mathscr{M}}{d\lambda} \cdot \mathscr{P}\right] \quad \text{and} \quad \frac{d\mathscr{P}\prime\prime}{d\lambda} = \mathrm{Im}\left[-\mathscr{M}^{-1} \cdot \frac{d\mathscr{M}}{d\lambda} \cdot \mathscr{P}\right]$$

Substituting these into Equation (3.29) gives

$$\frac{df}{d\lambda} = \frac{\partial f}{\partial \lambda} - \mathrm{Re}\left[\frac{\partial f}{\partial \mathscr{P}\prime} \cdot \mathscr{M}^{-1} \cdot \frac{d\mathscr{M}}{d\lambda} \cdot \mathscr{P}\right] - \mathrm{Im}\left[\frac{\partial f}{\partial \mathscr{P}\prime\prime} \cdot \mathscr{M}^{-1} \cdot \frac{d\mathscr{M}}{d\lambda} \cdot \mathscr{P}\right] \tag{3.30}$$

Similar to Equation (3.28), two adjoint variables are defined and computed using matrix-vector solves

$$\Lambda_1 = \frac{\partial f}{\partial \mathscr{P}\prime} \cdot \mathscr{M}^{-1} \quad \Lambda_2 = \frac{\partial f}{\partial \mathscr{P}\prime\prime} \cdot \mathscr{M}^{-1} \tag{3.31}$$

The final gradient of the general objective function is theCrefore

$$\frac{df}{d\lambda} = \frac{\partial f}{\partial \lambda} - \mathrm{Re}\left[\Lambda_1 \cdot \frac{d\mathscr{M}}{d\lambda} \cdot \mathscr{P}\right] - \mathrm{Im}\left[\Lambda_2 \cdot \frac{d\mathscr{M}}{d\lambda} \cdot \mathscr{P}\right] \tag{3.32}$$

3.5.7 Computing Gradient of Near-field Intensity

We now focus on the objective function based on near-field intensity, defined as $f = |\mathbf{E}|^2 = \mathbf{E} \cdot \mathbf{E}^*$, at a single point $\mathbf{x}_0$. As mentioned in Equation (3.19), field is a linear function of all dipoles. At a single point $\mathbf{x}_0$

$$\mathbf{E}(\mathbf{x}_0) = \sum_i \mathbf{M}_i^{\text{sc}} \cdot \mathbf{p}_i \tag{3.33}$$

For this objective function, the adjoint variables shown in Equation (3.31) require calculating $\frac{\partial \mathbf{E}^2}{\partial \mathbf{p}'}$ and $\frac{\partial \mathbf{E}^2}{\partial \mathbf{p}''}$ which follows from the chain rule

$$\frac{\partial \mathbf{E}^2}{\partial y} = 2\,\text{Re}\left[\mathbf{E} \cdot \frac{\partial \mathbf{E}^*}{\partial y}\right]$$

Re-writing chain-rule in terms of particles parameters and dipoles

$$\frac{\partial \mathbf{E}^2}{\partial \lambda_i} = 2\,\text{Re}\left[\mathbf{E} \cdot \frac{\partial \mathbf{E}^*}{\partial \lambda_i}\right], \quad \frac{\partial \mathbf{E}^2}{\partial \mathbf{p}_i'} = 2\,\text{Re}\left[\mathbf{E} \cdot \frac{\partial \mathbf{E}^*}{\partial \mathbf{p}_i'}\right], \quad \frac{\partial \mathbf{E}^2}{\partial \mathbf{p}_i''} = 2\,\text{Re}\left[\mathbf{E} \cdot \frac{\partial \mathbf{E}^*}{\partial \mathbf{p}_i''}\right] \tag{3.34}$$

To evaluate this further, the rules of complex differentiability are applied to $\mathbf{p} = \mathbf{p}' + i\mathbf{p}''$ and $\mathbf{p}^* = \mathbf{p}' - i\mathbf{p}''$

$$\frac{\partial \mathbf{p}_i^*}{\partial \mathbf{p}_i'} = 1, \quad \frac{\partial \mathbf{p}_i^*}{\partial \mathbf{p}_i''} = -i$$

Applying this to Equation (3.33) gives derivative of the field :

$$\frac{\partial \mathbf{E}^*}{\partial \mathbf{p}_i'} = \mathbf{M}_i^{\text{sc}}, \quad \frac{\partial \mathbf{E}^*}{\partial \mathbf{p}_i''} = -i\mathbf{M}_i^{\text{sc}}$$

This is substituted in the chain-rule Equation (3.34). We use the fact that $\text{Im}\, iz = -\,\text{Re}\, z$

$$\frac{\partial \mathbf{E}^2}{\partial \mathbf{p}'} = 2\,\text{Re}\,\mathbf{M}_i^{\text{sc}} \cdot \mathbf{E}, \quad \frac{\partial \mathbf{E}^2}{\partial \mathbf{p}''} = 2\,\text{Im}\,\mathbf{M}_i^{\text{sc}} \cdot \mathbf{E} \tag{3.35}$$

The two systems of equations with adjoint variables are

$$\mathbf{M}_i^{\text{sc}} \cdot \Lambda_1 = 2\,\text{Re}\,\mathbf{M}_i^{\text{sc}} \cdot \mathbf{E} \quad \mathbf{M}_i^{\text{sc}} \cdot \Lambda_2 = 2\,\text{Im}\,\mathbf{M}_i^{\text{sc}} \cdot \mathbf{E} \tag{3.36}$$

Before solving for the adjoint variables, we first derive the explicit derivative $\frac{\partial f}{\partial \lambda}$ in Equation (3.32) for positions ($\mathbf{x}_i$) and material parameters (λ_i). From Equation (3.19), $\mathbf{M}_i^{\text{sc}}$ depends on positions $\mathbf{x_i}$ through $\mathbf{r}_i = \mathbf{x}_0 - \mathbf{x}_i$. Taking the partial derivative of Equation (3.33) with respect to positions ($\frac{\partial}{\partial \mathbf{x_i}} = \nabla_{\mathbf{x}_i}$) reduces to taking the partial derivative of $\mathbf{M}_i^{\text{sc}}$, which is represented in gradient notation as

$$\nabla_{\mathbf{r}_i} \mathbf{M}_i^{\text{sc}} = -\nabla_{\mathbf{x}_i} \mathbf{M}_i^{\text{sc}}$$

As a result

$$\nabla_{\mathbf{x}_i} \mathbf{E} = -\nabla_{\mathbf{r}_i} \mathbf{M}_i^{\text{sc}} \cdot \mathbf{p}_i$$

Substituting into Equation (3.34) with respect to positions gives

$$\frac{\partial \mathbf{E}^2}{\partial \mathbf{x}_i} = -2\,\text{Re}[\mathbf{E} \cdot (\nabla_{\mathbf{r}_i} \mathbf{M}_i^{\text{sc}})^* \cdot \mathbf{p}_i^*]$$

Simplifying using tensor-notation gives

$$\frac{\partial \mathbf{E}^2}{\partial \mathscr{X}} = -\mathscr{M}^{sc} : \mathscr{P}^* \mathscr{E}$$

We have omitted Re for simplification. Since $\mathbf{M}_i^{\text{sc}}$ is independent of material parameters including radius

$$\frac{\partial \mathbf{E}^2}{\partial \lambda_i} = 0$$

We then solve Equation (3.36) for Λ_1 and Λ_2 which are substituted into Equation (3.32). For particle positions $\mathbf{x}_i$, the real and imaginary terms of Equation (3.32) reduces to a calculation between dipoles and adjoint variables, where $\frac{\partial}{\partial \mathbf{x}} = \nabla_{\mathbf{x}}$

$$\frac{d|\mathbf{E}|^{\mathbf{2}}}{d\mathbf{x}} = \nabla_{\mathbf{x}} |\mathbf{E}|^2 - \operatorname{Re} \nabla_{\mathbf{x}} \mathscr{M} : \mathscr{P} - \operatorname{Im} \nabla_{\mathbf{x}} \mathscr{M} : \mathscr{P} \tag{3.37}$$

For material parameters λ_j (dielectric parameters, radius) the gradient follows same framework of Equation (3.32). Since $\frac{\partial M}{\partial \lambda_j}$ is only non-zero for $\mathbf{M}_{jj}$ block, the derivative reduces to

$$\frac{\partial}{\partial \lambda_j} \mathscr{M} : \mathscr{P} = \frac{\partial M_{jj}}{\partial \lambda_j} \sum_i (\mathbf{p}_i \cdot \Lambda_{1,i}) \tag{3.38}$$

where the sum runs over for all particles i sharing the same material parameter j. The full gradient then is

$$\frac{d|\mathbf{E}|^2}{d\lambda} = -\operatorname{Re} \frac{\partial M_{jj}}{\partial \lambda_j} \sum_i (\mathbf{p}_i \cdot \Lambda_{1,i}) - \operatorname{Im} \frac{\partial M_{jj}}{\partial \lambda_j} \sum_i (\mathbf{p}_i \cdot \Lambda_{2,i}) \tag{3.39}$$

For field mapping in Figure 3.7, the objective function sums field intensity over a grid of points ($\mathbf{x}_k$) instead of a single grid point ($\mathbf{x}_0$). It is weighed by a field mask g_k, where g_k assigns -1 inside the target field pattern and +1 outside the pattern

$$f = \sum_k g_k |\mathbf{E}(\mathbf{x}_k)|^2 \quad g_k = \begin{cases} -1 \in \text{pattern} \\ 1 \notin \text{pattern} \end{cases} \tag{3.40}$$

Since g_k is independent of positions and material parameters, it carries through as a pCrefactor in the gradient. The partial derivatives with respect to $\mathbf{p}'$ and $\mathbf{p}''$ is a sum of field intensity over all grid points k

$$\frac{\partial |\mathbf{E}(\mathbf{x}_k)|^2}{\partial \mathbf{p}'} = 2 g_k \operatorname{Re} \sum_{k=1}^{N_E} \mathbf{M}_{ik}^{\text{sc}} \cdot \mathbf{E}(\mathbf{x}_k) \tag{3.41}$$

$$\frac{\partial |\mathbf{E}(\mathbf{x}_k)|^2}{\partial \mathbf{p}''} = 2 g_k \operatorname{Im} \sum_{k=1}^{N_E} \mathbf{M}_{ik}^{\text{sc}} \cdot \mathbf{E}(\mathbf{x}_k) \tag{3.42}$$

This is similarly re-written into a system of equations with two adjoint variables that can be solved using two matrix-vector solves and used in Equation (3.32) to calculate the gradient of this objective function

$$\mathbf{M}_i^{\text{sc}} \cdot \Lambda_1 = 2 g_k \operatorname{Re} \sum_{k=1}^{N_E} \mathbf{M}_{ik}^{\text{sc}} \cdot \mathbf{E}(\mathbf{x}_k) \quad \mathbf{M}_i^{\text{sc}} \cdot \Lambda_2 = 2 g_k \operatorname{Im} \sum_{k=1}^{N_E} \mathbf{M}_{ik}^{\text{sc}} \cdot \mathbf{E}(\mathbf{x}_k) \tag{3.43}$$

3.5.8 Details of Stratified Metasurface Design

Stratified metasurface is made up of M layers of Drude nanoparticles. The layer spacing is $h = 2.526$. In each layer, particles are arranged on a hexagonal lattice and their positions are fixed. All particles with the same layer n are identical with radius a_n and plasma frequency ω_n, but each layer is generally different from other layers. All particles have a damping coefficient of $\gamma = 0.1$ and $\varepsilon_\infty = 1$.

For the design, each layer has an ordered FCC(111) oriented lattice with 36 NPs. Electric field is linearly polarized in the x-direction $\mathbf{E_{0,x}}$ with infinite periodicity in x, y directions. Position coordinates of all NPs are fixed. We only vary the dielectric design parameters plasma frequency (ω_p) and radius (a) between layers, while fixing $\varepsilon_\infty/\varepsilon_f$ and γ/ω_p^* for all layers to 1 and 0.1 respectively. We initialize the values for (ω_p) and radius using analytic expressions of $\omega_{res,i}$ and h for a single Drude nanoparticle.[31] Each layer's plasma frequency is defined as $\omega_{\text{res},i} = \omega_{p,i}^* \frac{1}{\sqrt{2+\frac{\varepsilon_\infty}{\varepsilon_f}}}$ (1) $\omega_{res,i}$ of each layer is calculated by dividing the target spectra ($\sigma_t/\hat{\sigma} = 3$; $0.3 \leq \omega/\omega_p^* \leq 0.7$) into number of values equal to the number of layers. Using fixed $\varepsilon_\infty/\varepsilon_f$ it is simplified as $\omega_{p,i}^* = \sqrt{3}\omega_{res,i}$. Using analytic equation for height ($h = \sigma_t = 3$), we calculated the radius for each layer a_i

$$h = \frac{9\sqrt{\varepsilon_f \mu_f}\,\omega_{p,i}^{*2}\,a_i^3}{\gamma\left(2+\frac{\varepsilon_\infty}{\varepsilon_f}\right)^2} \quad c(\text{constant terms}) = \frac{9\sqrt{\varepsilon_f \mu_f}}{\gamma\left(2+\frac{\varepsilon_\infty}{\varepsilon_f}\right)} \quad a_i = \left(\frac{h}{c\omega_{p,i}^{*2}}\right)^{1/3} \tag{3.44}$$

It can be seen from Equation (3.44) that a_i is related to $\omega_{p,i}^*$ as $a_i \propto 1/\omega_{p,i}^{*\,2/3}$. We observed an inverse relationship in-line with above relation between the two parameters in previous simulations. Hence, we also initialize the $\omega_{p,i}^*$ and a_i for each layer according to this relationship, which can be seen in iteration 0 in Figure 3.2c. In Figure 3.2a, initial σ spectra is much lower than σ_t. The σ spectra reaches σ_t with fluctuations over the course of 10000 iterations. It can be seen that radius (a) and ω_p increase during course of the optimization for most of the layers Figure 3.2c. Configuration for the optimized extinction or final iteration is shown in Figure 3.2b. The highest layer in yellow has the largest ω_p corresponding to $\%Sn$ doped in ITO plasmon nanoparticle. Lower layers have lower $\%Sn$ and largest size. This trend can also be confirmed from Figure 3.2c.

3.5.9 Details of 3D Metamaterial Design

We initialize a 3D box composed of 360 Drude nanoparticles randomly placed with periodic boundary conditions. Configuration is generated for several volume fractions ($\phi = 0.05, 0.1, 0.2, 0.3, 0.4$). For all configurations, magnitude of the noise term is set as $T = 0.2a_0$. Optimization is run on all of the volume fractions for more than 2000 iterations with a step-size of 0.01 for updating particle positions All volume fractions were optimized up to a different final iteration.

3.5.10 Details of Near-Field Intensity Design

To demonstrate near-field intensity optimization, our chosen problem is as follows : we have a 2D monolayer with 36 NPs in the xy plane, covering an area fraction of $\phi = 0.05$. Each NP is randomly placed in the plane to form a disordered arrangement. The z-coordinate of the particles is zeroed out, in the optimization scheme to ensure it has degrees of freedom only in the x and y positions. A detector plane parallel to the monolayer plane is placed right at the circumference of the NP spheres with non-dimensional radius of 1 shown in Figure 3.7b. Detector plane is a uniform grid with 100×100 grid points $\mathbf{x}_E$. We overlay a field mask g_k on the detector plane (Section 3.5.7). A

target field pattern of 16 polka dots is chosen with 4 polka dots in each row. Radius of each polka dot is chosen as $a_t = 4$ to allow enough spacing between them. Field mask g_k is -1 in the area of each polka dot and +1 in the spacings between them. Circumference of each polka dot is shown in red circles in Figure 3.7c-f. The chosen objective function for our optimization is product of g_k and near-field intensity (Equation (3.40)).

Goal of the optimization is to minimize the objective function or in other words, maximize near-field intensity in the polka dots region by updating the position of the NPs in the initial disordered arrangement. We demonstrate this optimization for probe frequencies of $\omega_0 = 0.4$and$\omega_0 = 0.7$ for linear polarizations ($\mathbf{E_{0,z}}$ and $\mathbf{E_{0,x}}$).(Figure 3.7c-f) All optimizations use a step-size of 0.005 and steepest-descent with simulated annealing scheme ($\mathbf{W} = 0.4$) detailed in Equation (3.20). We have tuned these parameters to reduce numerical instability from the optimizer.

Chapter 4

Inverse Design of Incident Angle Dependence of Optical Metamaterials

The optical properties of quasi-2D metasurfaces are typically quite sensitive to the angle θ of the incident light relative to the surface normal, with $\theta = 0$ indicating normal-incident light. A common example is the variety of colors observed from the reflecting light off a CD, which contains μm-scale structural features, as its tilt angle varies. Even flat interfaces between two surfaces of different refractive indices show strongly angle-dependent behavior. One example of angle-dependent phenomena is total internal reflection (TIR). When light moves from a medium of higher refractive index to one of lower refractive index, it is not transmitted into the second medium once the incidence angle θ exceeds the critical angle θ_c,. and is instead reflected entirely. Metasurfaces are also known to exhibit angle-dependent TIR phenomena.[145]

The sun subtends an angle of $\Delta\theta = \pm 0.27^\circ$ in the sky, and sunlight reaching the ground is also scattered by the atmosphere. Additionally, position of the sun changes throughout the day. Thus even direct sunlight reaches the surface across a wide range of incidence angles and is never perfectly normally incident ($\theta = 0$). Since sunlight is such a common and practically important light source, angle of incidence dependence is a very important design consideration. Xiao, Yablonovitch, Braun and co-workers investigated spectral splitting of sunlight using a metasurface. Sunlight is directed through this metasurface and split onto two laterally placed photovoltaic sub-cells, such that the visible band of the solar spectrum is directed to the visible sub-cell and infrared light is directed to the infrared sub-cell.[66] Normally-incident light was used to design the metasurface. It was then tested with light illuminated at an angle of $\theta = 1^\circ$. To test this, figure of merit of spectral splitting efficiency is used, which is the average fraction of incident light, across sampled wavelengths, that is transmitted to the correct sub-cell. Visible light ($\lambda \leq 760$ nm) is transmitted to the visible sub-cell and infrared light is transmitted to the infrared sub-cell ($\lambda > 760$ nm). Spectral splitting efficiency at normal incidence is around 70%, which lowers to 50% at $\theta = 1^\circ$. A splitting efficiency of 50% is equivalent to no splitting. Fig 6 of the paper shown here as Figure 4.1A, B shows that diffracted light of different colors (shown as the simulated optical intensity colored profile) in the sub-cell region undergoes a lateral shift when the incidence angle goes from normal to 1°, causing each sub-cell to receive a different part of the solar spectrum than at normal incidence. As a result, the diffracted visible light illuminates the infrared sub-cell in red instead of the visible sub-cell in blue. Going above $\theta = 1^\circ$ reduces the splitting efficiency further, demonstrating that the metasurface cannot be used for light incident beyond $\theta = 1^\circ$. Additionally, this study also demonstrates that incidence angle is coupled with other parameters of the material to determine the optical response, in this case spectral splitting efficiency. This can be seen in *Fig S7* in the paper (Figure 4.1C) where the spectral splitting efficiency is reported for two metasurfaces with different pixel sizes of $1\mu m$ and $5\mu m$. Efficiency drops drastically for both the $1\mu m$ and $5\mu m$ metasurface. As a result, both have degraded performance with increase in angle of incidence.

Several studies report similar degradation in the performance of spectral splitters designed at normal incidences, even for small deviations from normal incidence.[146,147] Schubert and coworkers optimized spectral splitter design to accommodate a wider range of oblique incidence angles and

evaluated using the figure of merit of current density (current flowing through a cross-sectional area) as a function of angle of incidences.[148] They find that for a range of small angles of incidence, current density is high within the range but degrades quickly outside of it, whereas for a range of large angles, current density is lower but doesn't degrade as fast outside the range. They also aim to design a solar spectral splitter with high spectral splitting efficiency across a wide range of incident angles.

In contrast to previous examples, where angle dependence degraded performance, other efforts have deliberately designed metasurfaces with strong angle and polarization-dependent responses that can be precisely controlled. Incidence angle also affects the optical properties of magnetically self-assembled nanoparticles, which falls into two categories of materials. First are the magnetic, non-plasmonic nanoparticles, that can form photonic crystals with strong light-matter interactions. Second are the magnetoplasmonic nanoparticles, that are plasmonic with each particles own localized surface plasmon resonance and so do not need to form crystals to have strong light-matter interactions. Controlling how NPs self-assembled in an external magnetic field respond to incidence angle, can allow control over the color of the NPs, which makes it promising for applications in color displays, sensors, pigments, and dyes. Dynamically tunable structural colors have been extensively reviewed ([149–152]) and are a promising future step for the work detailed later in this chapter.

For example, Ag/Fe_3O_4 core-shell NPs with 80 nm Ag core and 75 nm thick Fe_3O_4 shells self-assemble into 1D chains under an external magnetic field. Wu and co-workers explain why this geometry produces such strong angle dependence. They show that when angle is 90°, quadrupole plasmonic mode dominates the extinction spectra and when angle is 0°, the dipole plasmonic mode dominates it. Near-field coupling between the neighboring particles is shown to be much stronger at 90°. The extinction and reflectance spectra of the Ag/Fe3O4 solution,(Figure 4.1E, F) and the electric field distribution around the NPs, vary as the angle changed from 0°to 90°. As the reflectance spectrum shifts, the solution's color changes from yellow to green to light brown.[153]

Anisotropy of metasurfaces, or their polarization dependent response has clear advantages. It is useful for applications such as colorimetric sensors of various shapes and for devices whose optical response changes in response to external stimuli[154]. However, this same sensitivity, while it serves as a feature for such tunable applications, also motivates the need to design materials with deliberate control over the polarization response. Investigating anisotropic geometries such as rods is therefore a promising area to explore, both for exploiting and controlling this sensitivity. For gold nanorods, this anisotropy can be controlled by changing the spacing between rods and their dimensions,[155] or through nanorod alignment.[156]

In this chapter, we aim to investigate the optical response of metamaterials with spherical NP building blocks used in Chapter 3 in the presence of incident light at different angles or polarization direction. In Chapter 3 we designed optical metamaterials via nanoparticle self-assembly under illumination with linearly polarized light. The optical extinction cross-section and near-field intensity response were therefore reported with respect to a single, linear polarization. We did not investigate the optical response when light is incident at an angle, or when the polarization is parallel or perpendicular to the plane of incidence. Investigating this dependence is crucial for designing optical metamaterials for applications such as spectral splitting of sunlight in multi-junction photovoltaic cells and color filters.

Using MPM detailed in Chapter 3, we illuminate our multilayer metasurface (Figure 4.2A) with light at two different incidence angles, $\theta = 0$ (normal incidence) and $\theta = 90$ (grazing incidence). In the quasistatic limit, where wavelength of light is much bigger than nanoparticle radius, where we

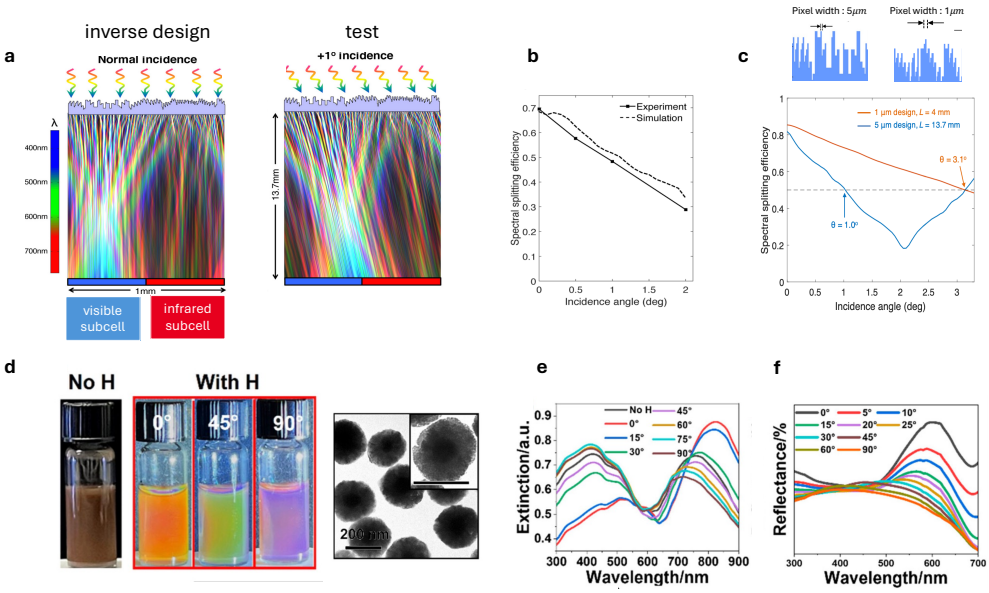

Figure 4.1: **A:** Color profile of the simulated optical intensity between the metasurface and the sub-cells, under normal and 1° incidence illumination. The color at a point in space denotes the wavelengths with large relative intensity. Wavelengths corresponding to different colors are added using their RGB color values. **B:** Spectral-splitting efficiency vs incidence angle. **C:** Comparison of the angular response of the optimized metasurface with 5 µm pixel size and and the optimized structure with 1 µm pixel size and 4 mm distance. The dashed curve marks 50% efficiency, at which no net splitting occurs. Panels **A, B, C** Reprinted with permission from ref[66]. Copyright 2016 American Chemical Society; **D:** Photographs of an aqueous solution of Ag/Fe_3O_4 nanoparticles before and after exposure to a magnetic field of varying directions (0, 45, 90°) and TEM image of Ag/Fe_3O_4 nanoparticles. **E:** Extinction spectra of the nanoparticle solution under a magnetic field with varying angle θ (between unpolarized light and nanochains) from 0 to 90°. **F:** Reflectance spectra of the nanoparticle solution under a magnetic field with varying α from 0 to 90°. Panels **D, E, F** Reprinted with permission from ref[153]. Copyright 2023 American Chemical Society;

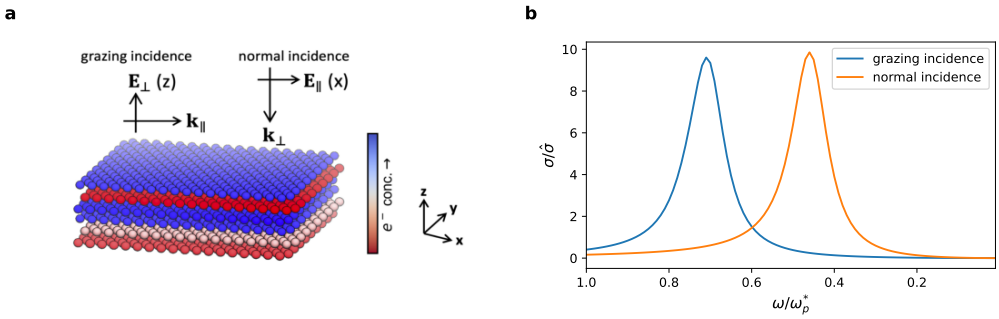

Figure 4.2: **A:** Multi-layer metasurface of plasmonic NPs illuminated with perpendicular polarization (grazing incidence) and parallel polarization (normal incidence) **B:** Extinction cross-section for grazing and normal incidence.

perform our simulations, this is entirely captured by two polarization directions. Their propagation vectors are grazing the surface ($\mathbf{E}_\perp(\mathbf{z})$) and normal to it ($\mathbf{E}_\parallel(\mathbf{x})$). (Figure 4.2a) Extinction cross-sections for both polarizations are not overlapping. Extinction at normal incidence (orange curve in Figure 4.2B, denoted as σ_x) is red-shifted, with respect to extinction at grazing incidence (blue curve in Figure 4.2B, denoted as σ_z). Hence, the plasmonic NP multilayer metasurface shares the same qualitative sensitivity to polarization direction, or in other words the angle of incidence spanning from 0°to 90°between parallel and perpendicular polarization, as the spectral splitters, magnetoplasmonic NPs, and nanorods discussed above, although the underlying mechanisms of dependence differs in each case.

All of these are examples of forward design. In this chapter, we aim to optimize materials that account for the incidence angle or have an optical response that is agnostic to it, through the inverse design framework detailed in Chapter 3. We build upon two key components of this framework, the steepest-descent and adjoint methods of optimization, in this chapter.

This chapter is laid out as follows: we propose a modified objective function with the aim of achieving identical extinction cross-section responses for parallel and perpendicular polarization. We demonstrate the framework with the modified objective function for multilayer metasurfaces, targeting extinction spectra corresponding to a single NP and to a band-stop filter. We discuss the contribution of each layer to the overall optimized extinction spectrum. We then lay out the stratified-medium calculation, which we use to calculate reflectance and transmittance, and investigate its underlying assumption and relation to the angle of incidence. Finally, we optimize for reflectance through the adjoint method. This is demonstrated for normal incidence (0°).

4.1 Objective Function Incorporating Incidence Angle

In Chapter 3, we demonstrated how to control the extinction cross-section of a plasmonic metamaterial by minimizing the integrated squared error $f(\lambda)$ between the simulated $\sigma(\omega;\lambda)$ and the target $\sigma_t(\omega)$ extinction spectra

$$f(\lambda) = \int_0^\infty d\omega \left(\sigma(\omega;\lambda) - \sigma_t(\omega)\right)^2 \tag{4.1}$$

where $\lambda = [\lambda_1, \ldots, \lambda_M]$ is a set of M design parameters that can include the position of a nanoparticle i $\mathbf{x}_i$, its radius a_i, plasma frequency $\omega_{p,i}$, damping coefficient γ_i, and high-frequency permittivity $\varepsilon_{\infty,i}$. A straightforward way to incorporate incidence angle into the optimization is to simply use a target spectrum that depends on ω and θ and integrate over both variables

$$f(\lambda) = \int_0^{\pi/2} d\theta \int_0^{\infty} d\omega \Big(\sigma(\omega, \theta; \lambda) - \sigma_t(\omega, \theta)\Big)^2 \tag{4.2}$$

To compute (4.2), we must evaluate $\sigma(\omega, \theta; \lambda)$ on a grid of M_ω values of ω and M_θ values. This requires $M_\omega M_\theta$ matrix/vector solves (Equation (3.12)) per optimization iteration, which is a factor of M_θ slower than the optimizations in Chapter 3. Because $M_\theta \approx 10$–100 and the solves are fast with MPM, (4.2) is not completely cost-prohibitive, but it is slow.

In the case where we desire a target σ_t that is completely independent of θ, we can use a simpler objective function that has the same minimum as (4.2). First, notice that if θ is defined relative to a plane normal vector $\hat{\mathbf{n}}$, σ can be decomposed into contributions from in-plane and out-of-plane polarizations

$$\sigma \sim \operatorname{Im}\left[\mathbf{p} \cdot \mathbf{E}_0\right] = \operatorname{Im}\left[\mathbf{C} : \mathbf{E}_0\mathbf{E}_0\right] = \operatorname{Im}\left[C_\perp \sin^2\theta + C_\parallel \cos^2\theta\right] = \sigma_\perp \sin^2\theta + \sigma_\parallel \cos^2\theta \tag{4.3}$$

where $\sigma_\parallel$ is the extinction cross-section for $\mathbf{E}_0$ in the material plane (grazing incidence with $\mathbf{k}_\parallel$) and $\sigma_\perp$ is the extinction cross-section for $\mathbf{E}_0$ orthogonal to the material plane (normal incidence with $\mathbf{k}_\perp$) (in the $\hat{\mathbf{n}}$ direction). If $\sigma_\perp = \sigma_\parallel$, then σ is independent of θ. With this, we propose the following objective function

$$f(\lambda) = \eta \int_0^{\infty} d\omega \left(\frac{\sigma_\parallel(\omega; \lambda) + \sigma_\perp(\omega; \lambda)}{2} - \sigma_t(\omega)\right)^2 + (1 - \eta) \int_0^{\infty} d\omega \left(\sigma_\perp(\omega; \lambda) - \sigma_\parallel(\omega; \lambda)\right)^2 \tag{4.4}$$

To minimize f, the optimizer will attempt to minimize both integrals in (4.4), with the parameter η setting the relative weighting between the two. The second term in (4.4) reduces the mismatch between $\sigma_\parallel$ and $\sigma_\perp$, enforcing that the metamaterial is not sensitive to θ. Thus,

$$f_\theta(\lambda) = \int_0^{\infty} d\omega \left(\sigma_\perp(\omega; \lambda) - \sigma_\parallel(\omega; \lambda)\right)^2 \tag{4.5}$$

is a measure of the "isotropic error", i.e. how far away the metamaterial is from no θ dependence. When $\eta = 0$, $f = f_\theta$ and the overall objective function is equal to the isotropic error. The first term in (4.4) is similar to that in Equation (3.3) and reduces the mismatch between the metamaterial's extinction spectrum and the target spectrum. Thus,

$$f_t(\lambda) = \int_0^{\infty} d\omega \left(\frac{\sigma_\parallel(\omega; \lambda) + \sigma_\perp(\omega; \lambda)}{2} - \sigma_t(\omega)\right)^2 \tag{4.6}$$

is a measure of the "target error". When $\eta = 1$, $f = f_t$. The derivative of this objective function is

$$\begin{aligned}\frac{\partial f}{\partial \lambda} = \eta \int_0^{\infty} d\omega \left(\frac{\sigma_\parallel(\omega; \lambda) + \sigma_\perp(\omega; \lambda)}{2} - \sigma_t(\omega)\right) \left(\frac{\partial \sigma_\parallel}{\partial \lambda} + \frac{\partial \sigma_\perp}{\partial \lambda}\right) \\ + 2(1 - \eta) \int_0^{\infty} d\omega \Big(\sigma_\perp(\omega; \lambda) - \sigma_\parallel(\omega; \lambda)\Big) \left(\frac{\partial \sigma_\parallel}{\partial \lambda} - \frac{\partial \sigma_\perp}{\partial \lambda}\right)\end{aligned} \tag{4.7}$$

The extinction derivatives $\partial\sigma_{\parallel}/\partial\lambda$ and $\partial\sigma_{\perp}/\partial\lambda$ are computed with the same method as Equation (3.4) discussed in Section 3.3.2.

4.1.1 Inverse Design of Quasi-2D Metasurfaces with Incident Angle Independent Refractive Index

We first demonstrate the optimization routine with the modified objective function by using a quasi-2D metasurface composed of 2D hexagonal layers of plasmonic structures, similar to the metasurface used in Chapter 3 and fig. 3.2. We consider a 4-layer material with nanoparticle positions fixed to a face-centered cubic (FCC) lattice oriented with the z-axis normal to the (111) plane. All particles within the same layer n are identical, with radius a_n, plasma frequency ω_n, damping coefficient γ_n, and high-frequency permittivity $\varepsilon_{\infty,n}$, but layers differ from one another.

We use our optimization framework established in Chapter 3 along with the modified objective function Equation (4.4) and its gradient Equation (4.7) with an extinction spectrum of a single isolated Drude nanoparticle (red curve in Figure 4.3). This spectrum is calculated using analytic expressions for a single Drude nanoparticle truncated at the dipole level.[31]

$$\begin{aligned} \omega_{\text{res}} &= \omega_p^* \sqrt{\frac{1}{2+\frac{\varepsilon_\infty}{\varepsilon_f}}}, \qquad h = \frac{9\sqrt{\varepsilon_f \mu_f}\,\omega_p^{*2}}{\gamma\left(2+\frac{\varepsilon_\infty}{\varepsilon_f}\right)^2}, \qquad W = \gamma \\ \sigma(\omega) &= f(\omega;\omega_{\text{res}},W,h) = \frac{h}{1+\left(\frac{\omega_{\text{res}}}{W}\right)^2\left(\frac{\omega}{\omega_{\text{res}}}-\frac{\omega_{\text{res}}}{\omega}\right)^2} \end{aligned} \tag{4.8}$$

For the model spectrum, the initial values of the dielectric parameters are randomized. The bounds of the parameters and initial model choices are unconstrained for all Drude parameters $(\omega_p, \gamma, \varepsilon_\infty)$ and discussed in Section 4.2.2. The positions of the NPs are fixed. We then use steepest-descent optimization over 10000 iterations to update a_n and Drude parameters for both $\eta = 0.5$ (equally weighted error) and $\eta = 1.0$ (target error). Figure 4.3A and C show the evolution of the metamaterial's extinction spectrum over the course of the optimization for $\eta = 0.5$ and $\eta = 1.0$, respectively. For $\eta = 1$, as the isotropic error integral goes to 0 in Equation (4.4), now representing the original objective function used in Chapter 3, the extinction spectrum approaches the target. The optimized extinction spectrum (in yellow) in Figure 4.3C is decomposed into individual contributions of grazing (σ_z) and normal incidence (σ_x) in Figure 4.3D. The two spectra don't overlap, showing the absence of the isotropic integral term. Extinction progresses, starting with two peaks for normal and grazing incidence, and gets close to the target for $\eta = 0.5$ in Figure 4.3A; on decomposition (Figure 4.3B), the peaks overlap. This shows that, using the modified objective function with equally weighted error, the extinction response is now nearly independent of the electric field polarization.

It can be seen in Figure 4.3B that each individual extinction spectrum has three peaks. We speculate that each peak could be from extinction of an individual layer in the metasurface. We want to see how all layers contribute individually such that we are able to get overlap between grazing (σ_z) and normal incidence (σ_x) for $\eta = 0.5$. We investigate the individual layer contribution to both the grazing (σ_z) and normal extinction (σ_x) in Figure 4.4.

We use the optimized parameters in each layer and re-calculate their individual extinctions with grazing and normal incidence field. Similar to Figure 4.3, we re-calculate the overall extinction for grazing and normal incidence field as well. Overall σ_z (Figure 4.4A) and σ_x (Figure 4.4B) (spectra

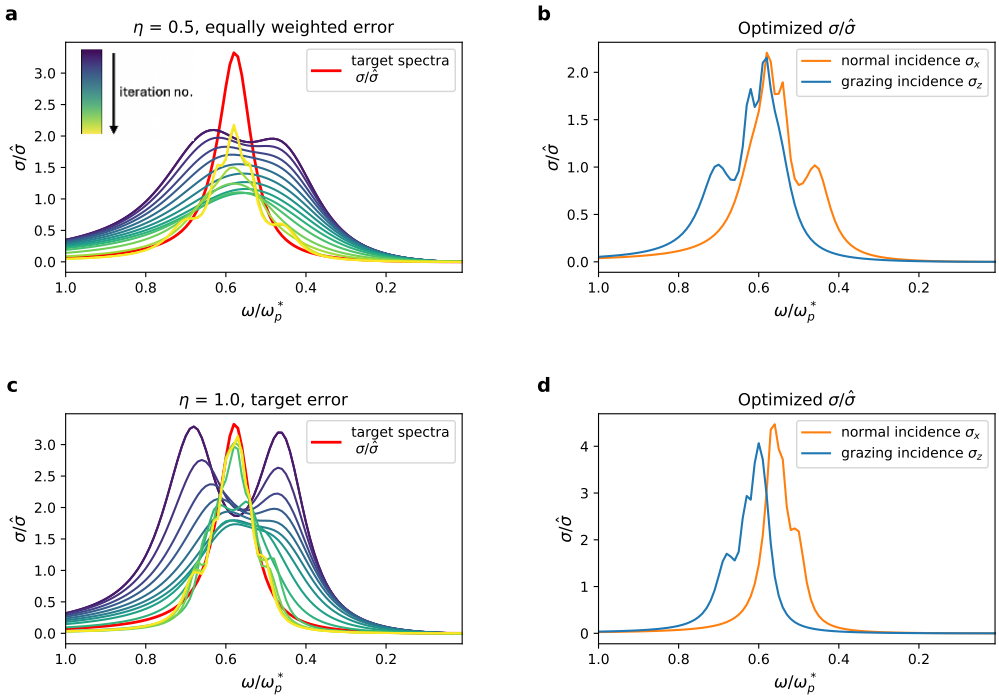

Figure 4.3: Inverse design of a stratified 4-layer plasmonic metasurface via the modified objective function with weighting parameter η, shown for equally weighted error ($\eta = 0.5$, top row) and target error ($\eta = 1$, bottom row). **A, C:** Evolution of the metasurface extinction spectrum σ, log-spaced over 10000 iterations, alongside the target spectrum (extinction of a single Drude NP calculated from analytical equations[31]), for $\eta = 0.5$ (**A**) and $\eta = 1$ (**C**). **B, D:** Individual contributions of grazing and normal incidence extinction to the optimized spectra, for $\eta = 0.5$ (**B**) and $\eta = 1$ (**D**). Quantities are non-dimensionalized by $\omega_p^* = \sqrt{\frac{\varepsilon_0}{\varepsilon_f}}\,\omega_p$ and $\hat{\sigma} = \sqrt{\varepsilon_f \mu_f}\omega_p^*$, respectively.

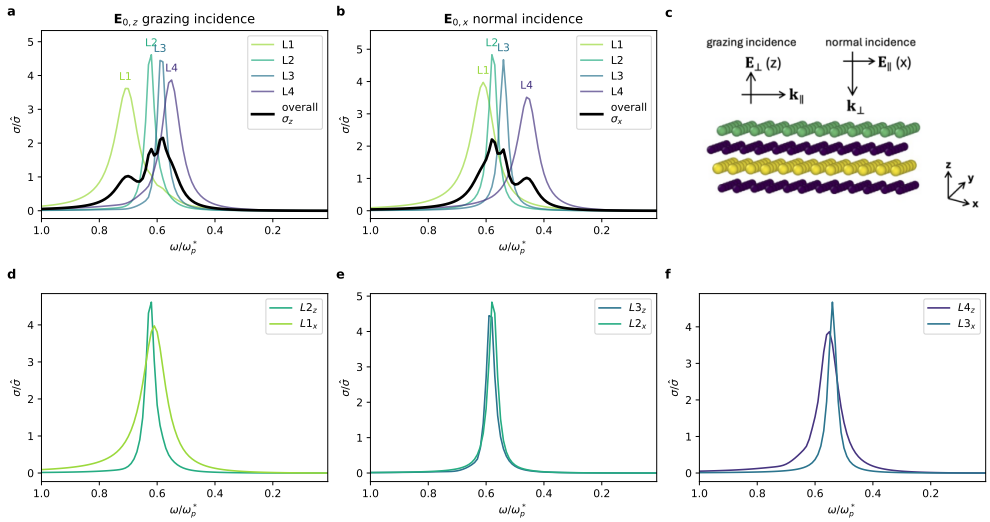

Figure 4.4: Optimized metasurface extinction in Figure 4.3 decomposed to layer-by-layer contribution from **A** : grazing incidence $\mathbf{E}_{0,z}$ and overall extinction σ_z; **B:** normal incidence $\mathbf{E}_{0,x}$ and overall extinction σ_x; **C:** snapshot of the 4-layer plasmonic metasurface colored by NP radius; Shift-by-one in extinction position between layers **D:** L_2 with $\mathbf{E}_{0,z}$ (shorthand $L_{2,z}$) and L_1 with $\mathbf{E}_{0,x}$ (shorthand $L_{1,x}$); **E:** $L3_z$, $L2_x$ and **F:**$L4_z, L3_x$

in black) are mirror images of each other. Resonance frequency ω_{res} for the highest peak in the overall extinction in both cases remains at the same frequency ≈ 0.6. Each extinction peak by layer is labeled in decreasing order of ω_{res}, starting with $L1$ (in light green) up to $L4$ (in purple). This convention is intentionally chosen to explain the mechanism. As demonstrated in Chapter A, the ordering of layers doesn't have a significant impact on the overall extinction due to insignificant coupling between the layers.

With grazing incidence, $\mathbf{E}_{0,z}$, all extinction-by-layer peaks (annotated in Figure 4.4A) are slightly blue-shifted compared to extinction-by-layer peaks with normal incidence $\mathbf{E}_{0,x}$. The overall peaks span about the same range of frequency for both polarizations. We can also see that the overall σ peaks are a sum of the individual layer extinctions. $L2$ and $L3$ contribute the most to the overall peaks in both cases, while $L1$ and $L4$ have their peaks further out.

When polarization changes from grazing to normal incidence all layer-by-layer peaks redshift-by-one. Individual layer N with extinction from grazing incidence overlaps with layer $N-1$ from normal incidence (Figure 4.4D, E, F). For example, the peak of $L2_z$ is replaced by $L1_x$. Their overlap is shown in Figure 4.4D. Similar overlap between $L3_z$, $L2_x$ (Figure 4.4E) and $L4_z$, $L3_x$ (Figure 4.4F) indicates that peaks undergo a shift-by-one and overlap with adjacent peaks, leading to overlap between the overall σ_z and σ_x. This demonstrates our goal of an optical response that is independent of polarization direction with our modified objective function at $\eta = 0.5$.

We see that there is systematic improvement in the overlap between the extinction responses for grazing and normal incidence polarization when we use 15 layers instead of 4 layers (Figure 4.5B). In this case, η is still 0.5, which is enough to let the initial model spectrum (blue) in Figure 4.5A reach very close to the target spectrum during the optimization due to the greater number of

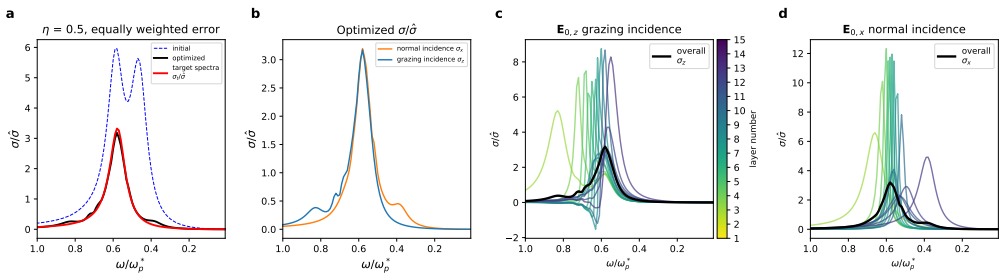

Figure 4.5: Inverse design of a stratified 15-layer plasmonic metasurface via the modified objective function with $\eta = 0.5$: **A:** target extinction (red), the metasurface extinction for initial values (blue), and for the final optimized structure (black); **B:** Individual contributions of grazing and normal incidence extinction to the optimized spectra; optimized spectra decomposed into layer-by-layer contribution from **C:** grazing incidence $\mathbf{E}_{0,z}$ and overall extinction σ_z; **D:** normal incidence $\mathbf{E}_{0,x}$ and overall extinction σ_x

layers. A similar decomposition of the optimized spectrum into σ_z and σ_x, and into individual layer extinctions, shows a similar redshift-by-one peak when going from grazing incidence (Figure 4.5C) to normal incidence (Figure 4.5D). Adjacent peaks between the two polarizations appear to overlap more with a greater number of layers, leading to a systematic improvement in the overlap between σ_z and σ_x.

4.1.2 Bandstop Functionality of Quasi-2D Metasurfaces with Incident Angle Independent Refractive Index

Similar to Section 3.3.3, we use the optimization tool, now with the modified objective function, to determine a set of a_n and $\omega_{p,n}$ that results in a metasurface with a rectangular extinction cross-section, having equi-intensity extinction across a specific frequency interval and zero extinction outside of this interval, characteristic of a band-stop filter introduced in Section 3.3.3. We use the same motivation to set the plasma frequency $\omega_{p,n}$ of each layer so as to span our target stopband equally, and use the scaling relation $a_n \sim \omega_{p,n}^{-2/3}$ to set the initial values of the radius. The initial values and range for this optimization are listed in Section 4.2.2. Using steepest-descent optimization without a simulated annealing scheme, and now with the modified objective function, we ran these optimizations for 200 iterations to update each a_n and $\omega_{p,n}$ for a 4-layer stratified metasurface. With $\eta = 1$, the optimized spectrum (in black) reaches close to the target (Figure 4.6C). We hypothesize that the peaks in the optimized spectrum may be due to contributions of each of the four layers. On decomposing it into σ_x and σ_z (Figure 4.6D), we see that they do not overlap, similar to Figure 4.3D. With $\eta = 0.5$, the optimized spectrum (in black) reaches close to the target as well (Figure 4.6A) and decomposes into σ_x and σ_z, whose peaks are much closer, approaching a polarization-agnostic extinction response. While this is not a perfect overlap, we ran this for only 200 iterations and only for 4 layers. We hypothesize that the extinction overlap would systematically improve by tuning some of these variables in the future.

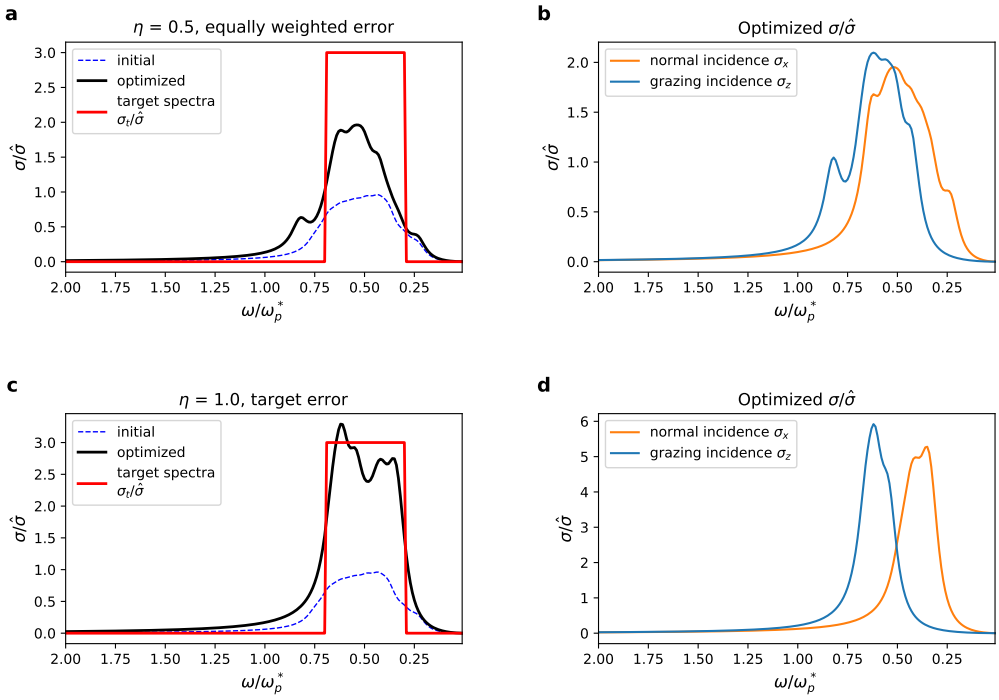

Figure 4.6: Inverse design of a stratified 4-layer plasmonic metasurface via the modified objective function, with weighting parameter η, shown for equally weighted error ($\eta = 0.5$, top row) and target error ($\eta = 1$, bottom row). $\gamma = 0.1\omega_p^*$ and $\varepsilon_\infty = \varepsilon_f$ are fixed for all nanoparticles and the optimizer updates the radius a and plasma frequency ω_p of each layer. **A, C:** target extinction with bandstop functionality (red), the metasurface extinction for initial values of a_n and $\omega_{p,n}$ (blue), and the metasurface extinction for the final optimized a_n and $\omega_{p,n}$ (black), for $\eta = 0.5$ (**A**) and $\eta = 1$ (**C**). **B, D:** individual contributions of grazing and normal incidence extinction to the final optimized spectra, for $\eta = 0.5$ (**B**) and $\eta = 1$ (**D**); Quantities are non-dimensionalized by $\omega_p^* = \sqrt{\frac{\varepsilon_0}{\varepsilon_f}}\,\omega_p$ and $\hat{\sigma} = \sqrt{\varepsilon_f \mu_f}\omega_p^*$, respectively.

4.1.3 Tuning the Bandstop Functionality of Quasi-2D Metasurfaces with Incident Angle Independent Refractive Index

Similar to Section 3.3.4, we can use our inverse design scheme with the modified objective function to tune the extinction spectrum of a stratified metasurface simply by inputting different target extinction spectra. Figure 4.7 shows that the framework remains flexible in the spectral features it can produce, with examples where we use inverse design to tune the bandcenter frequency, the bandwidth, and the number of stopbands, with $\eta = 0.5$. Figure 4.8 shows the same but with $\eta = 1$, i.e., the same as the original objective function. It is shown here to compare σ_x and σ_z.

In Figure 4.7A, the metasurface has a bandcenter of $0.8\omega_p^*$ and a much larger bandwidth of $1.2\omega_p^*$. Figure 4.7B and Figure 4.8A have a bandcenter shifted to $0.8\omega_p^*$ with the same bandwidth of $0.4\omega_p^*$ as in Figure 4.6. Finally, in Figure 4.7C and Figure 4.8C, the metasurface has three distinct stopbands each of bandwidth $0.08\hat{\omega}$. In all cases, the optimizer progresses close to target spectra and converges to solutions where the resonant frequencies of individual layers, $\omega_{\text{res},n}$, span the stopbands.

The optimized spectra, decomposed into σ_z and σ_x, are close to each other in all cases and approach overlap. While the overlap is not perfect, with peaks corresponding to each layer, it shows that the optimizer is working well to achieve a similar extinction response irrespective of polarization (Figure 4.7B, D, F). In contrast, σ_z and σ_x remain further apart with $\eta = 1$ (Figure 4.8B, D), demonstrating this improvement as well. The larger bandwidth of $1.2\omega_p^*$ is not included with $\eta = 1$ in Figure 4.8 due to parameters reaching the bounds of their range during optimization. Further debugging is needed to run the optimization.

4.1.4 Designing Angle Agnostic Materials for Optical Properties: Reflectance, Transmittance

We demonstrated, through the target extinction spectrum of a single NP and stopband functionality, that the extinction cross-section can be independent of polarization direction for a stratified metasurface that is at the reference plane. The hyperparameter η drives the optimizer to get $\sigma_{\parallel} \sim \sigma_{\perp}$, signaling that the metasurface is now isotropic. An isotropic material is one that has optical properties that do not depend on the direction from which they are measured, while properties will change with direction in an anisotropic material. Since σ is calculated from dipoles using $\sigma(\omega) = \alpha\omega\text{Im}[\mathbf{p}(\omega) \cdot \mathbf{E_0}]$, it follows that the dipoles $\mathbf{p}(\omega)$ are equivalent for both polarizations. The effective refractive index (n_{eff}) of a stratified medium layer is determined by the average dipole of plasmonic colloids through its effective permittivity.

$$n_{eff} = \frac{1}{\sqrt{\varepsilon_0}} \sqrt{\varepsilon_f + \frac{N}{V} \frac{\mathbf{p}(\omega)}{\mathbf{E_0}}} \tag{4.9}$$

It implies that $n_{eff,\parallel} \sim n_{eff,\perp}$. Here ε_f is the background permittivity, N is the number of colloidal particles in a medium layer, and V is the simulation box volume. Since $n_{eff,\parallel} \sim n_{eff,\perp}$, the effective medium (not necessarily the individual NPs) will show an isotropic response. As a result, polarization normal to the plane of incidence (s-polarization) and polarization parallel to the plane (p-polarization) will have the same refractive index $n_{eff,\parallel} \sim n_{eff,\perp} = n_{eff}$, and the Fresnel equations for isotropic media can be used to calculate reflectance and transmittance. These calculations for a stratified medium are discussed in detail in Section 4.2.1.

Our stratified multilayer metasurface consists of layers of NPs stacked together. When approxi-

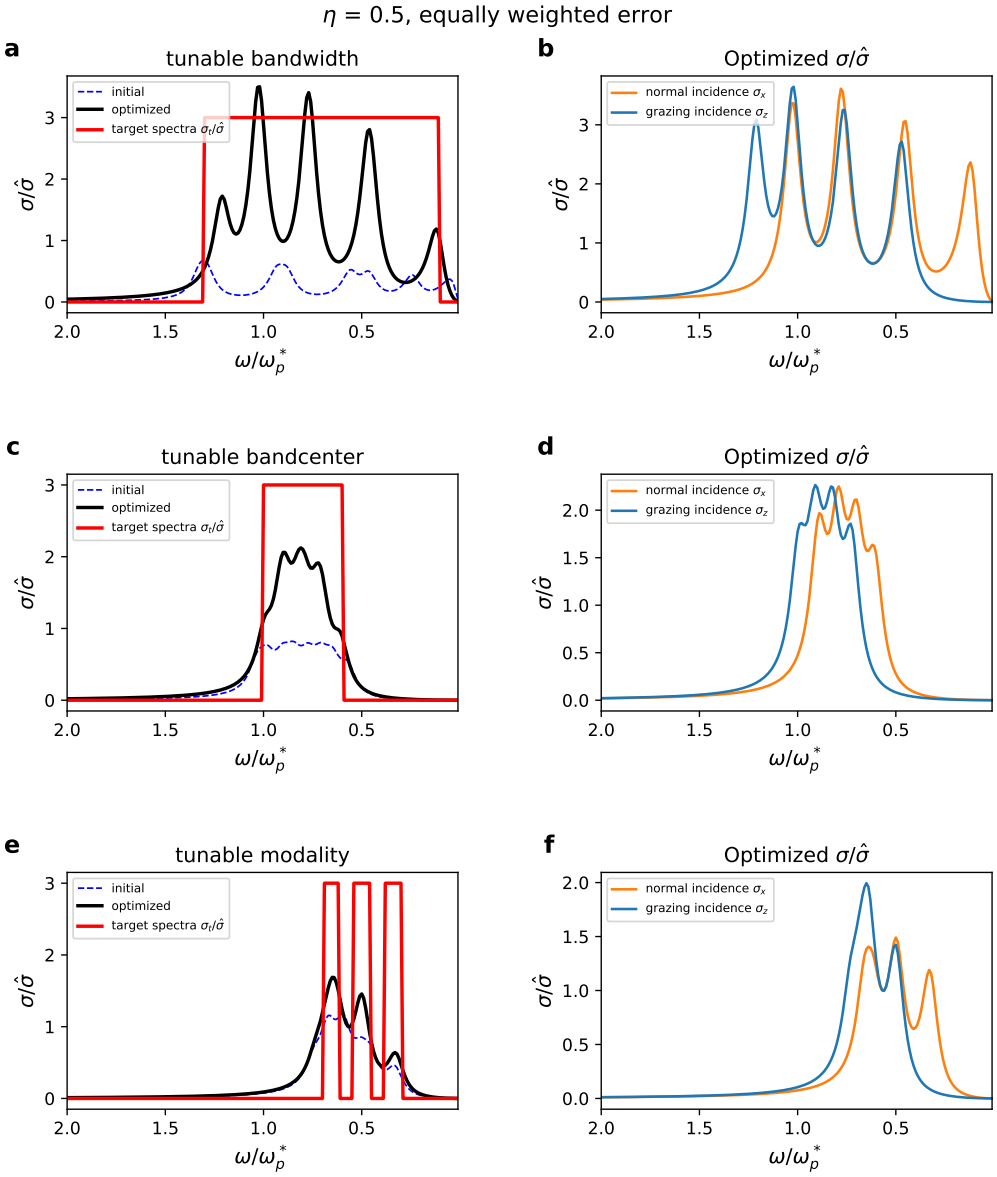

Figure 4.7: Tuning the extinction cross-section σ of stratified plasmonic metasurfaces for $\eta = 0.5$. Panels show the target extinction (red), the metasurface extinction for initial values of a_n and $\omega_{p,n}$ (blue), and the metasurface extinction for the final optimized a_n and $\omega_{p,n}$ (black). The target spectra are **A:** bandcenter $\Omega = 0.8\hat{\omega}$ and bandwidth $W = 1.2\hat{\omega}$; **C:** bandcenter $\Omega = 0.8\hat{\omega}$ and bandwidth $W = 0.4\hat{\omega}$; **E:** three stopbands of bandwidth $W = 0.08\hat{\omega}$ and bandcenters $\Omega = 0.34$, 0.50, $0.66\hat{\omega}$. **B, D, F:** Individual contributions of grazing and normal incidence extinction to the optimized spectra. All nanoparticles have fixed $\gamma = 0.1\hat{\omega}$ and $\varepsilon_\infty = \varepsilon_f$. The nondimensionalization is $\hat{\omega} = \sqrt{\varepsilon_0/\varepsilon_f}\,\omega_{p,0}$ and $\hat{\sigma} = \sqrt{\varepsilon_f \mu_f}\hat{\omega}$.

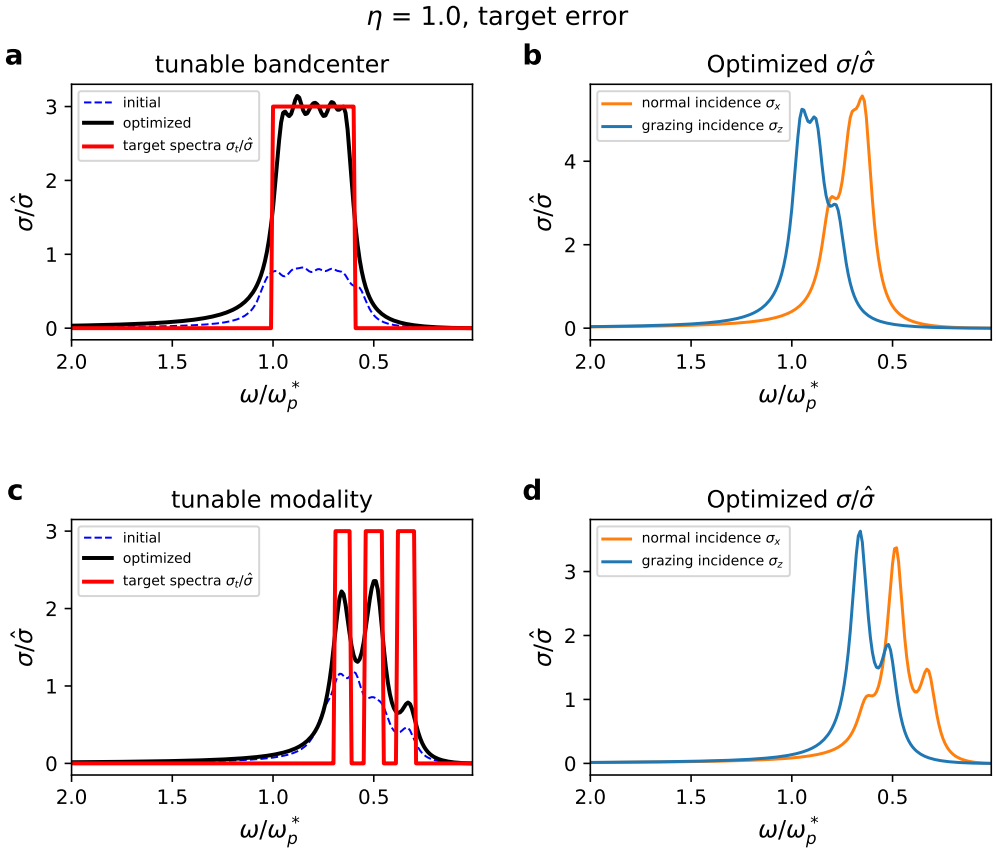

Figure 4.8: Tuning the extinction cross-section σ of stratified plasmonic metasurfaces for $\eta = 1$. Panels show the target extinction (red), the metasurface extinction for initial values of a_n and $\omega_{p,n}$ (blue), and the metasurface extinction for the final optimized a_n and $\omega_{p,n}$ (black). The target spectra are **A:** bandcenter $\Omega = 0.8\hat{\omega}$ and bandwidth $W = 0.4\hat{\omega}$; **C:** three stopbands of bandwidth $W = 0.08\hat{\omega}$ and bandcenters $\Omega = 0.34, 0.50, 0.66\hat{\omega}$. **B, D:** Individual contributions of grazing and normal incidence extinction to the optimized spectra. All nanoparticles have fixed $\gamma = 0.1\hat{\omega}$ and $\varepsilon_\infty = \varepsilon_f$. The nondimensionalization is $\hat{\omega} = \sqrt{\varepsilon_0/\varepsilon_f}\,\omega_{p,0}$ and $\hat{\sigma} = \sqrt{\varepsilon_f \mu_f}\hat{\omega}$.

mated as a slab through stratified media, the metasurface as a whole has an anisotropic response. Reflectance and transmittance will still depend on θ_0. This is because, while the isotropic slab sees the same n_{eff} at any incidence angle, Snell's law shows that the transmitted angle depends on the incidence angle, and both terms appear in the calculation of the Fresnel coefficients. Hence, overall, the stratified medium is still dependent on θ_0.

With the original $f(\lambda)$, the optical response is anisotropic ($\sigma_{\parallel} \neq \sigma_{\perp}$) and the reflectance and transmittance will still depend on θ_0. We speculate that there may be a scenario where the anisotropic response and the dependence on θ_0 cancel out such that the overall response of the slab becomes independent of θ_0. This is an area of ongoing work.

4.1.5 Optimization of Reflectance Using the Adjoint Method

Since the macroscopic quantities of reflectance, transmittance, and absorbance are fractions that add up to 1 ($R+T+A=1$), we select reflectance to guide the discussion of the optimization of all three quantities. To achieve a desired optical spectrum of reflectance as a function of θ_0, and learn about the structure of the slab, we can implement our inverse design framework. The objective function f will include the figure of merit of reflectance. Taking its gradient requires explicitly calculating $\mathscr{M}^{-1}$, just like taking the gradient of near-field intensity in Section 3.5.7.

For this optimization, we need to be able to compute the following gradients: $\frac{df}{d\mathbf{p}}, \frac{df}{dx}$. The following need to be calculated to compute the objective function, for example $f = \int_0^\infty d\omega (R - R_{tgt})^2$:

$$\frac{df}{dx} = \frac{df}{dR} \cdot \frac{dR}{dx} \tag{4.10}$$

$$\frac{dR}{dx} = \frac{dR}{dn} \cdot \frac{dn}{dx} \tag{4.11}$$

$$\frac{dn}{dx} = \frac{dn}{dC} \cdot \frac{dC}{dx} \tag{4.12}$$

$$\tag{4.13}$$

We use the adjoint method laid out in Sections 3.5.5 to 3.5.7 for reflectance.

Propagating these gradients and running inverse design is performed by Kenny Lam (a PhD student in the lab). Gradients have been propagated for proof-of-concept optimization examples. One example is a $1D$ optimization with the design parameter given by the position coordinates along the z-axis, at *normal incidence,* $\theta_0 = 0$.

Optimization of reflectance at normal incidence is being explored with various design parameters and a greater number of NPs at different position coordinates. Additionally, work is being done on gradient propagation of design variables in reflectance and transmittance for non-normal incidence angles. Initial work has been done for isotropic media, which will eventually be extended to anisotropic materials. This will be continued by Kenny Lam and will contribute to the overall goal of designing materials that are either agnostic to, or account for, the incidence angle of light.

4.2 Methods

4.2.1 Optical Properties of Stratified Media

A stratified medium is defined as a medium with constant properties throughout each plane perpendicular to a fixed direction. It is a stack of thin, plane-parallel layers that are homogeneous,

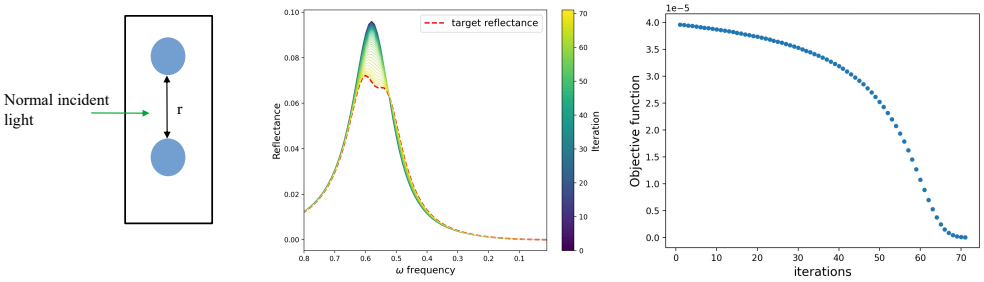

Figure 4.9: 1-D optimization of reflectance with the position coordinate along the z-axis as the design parameter, in the presence of light at normal incidence ($\theta_0 = 0$). Optimization results courtesy of Kenny Lam.

i.e. each layer has a uniform refractive index and thickness.[157]

We want to calculate the optical properties of reflectance R, transmittance T, and absorbance A through our multi-layer system with plasmonic NPs. All M layers in the system are isotropic media, each with permittivity ε_i, permeability μ_0, refractive index $n_i = \sqrt{\varepsilon_i \mu_0}/\sqrt{\varepsilon_0 \mu_0} = \sqrt{\varepsilon_i/\varepsilon_0}$, and thickness h_i. The first and last layers are semi-infinite (Figure 4.10).

As the incident light wave goes through the medium, part of it is reflected, transmitted, and absorbed. The corresponding quantities are as follows:

$$R = |\frac{\mathbf{E}_R}{\mathbf{E}_0}|^2 = \frac{1}{E_0^2}(\mathbf{E}_R \cdot \mathbf{E}_R^*) \tag{4.14}$$

$$T = \frac{n_M}{n_1}|\frac{\mathbf{E}_T}{\mathbf{E}_0}|^2 = \frac{n_M}{n_1}\frac{1}{E_0^2}(\mathbf{E}_T \cdot \mathbf{E}_T^*) \tag{4.15}$$

$$A = 1 - R - T \tag{4.16}$$

Hence, the goal of this section is to show how to calculate the electric fields of the reflected ($\mathbf{E}_R$) and transmitted ($\mathbf{E}_T$) light through stratified medium calculations.

For our calculations, the material plane of the system is the y-z plane. Incident light is polarized in the x-direction as $\hat{\mathbf{e}}_x$. The incident light angles are defined as $0 \leq \theta_0 \leq \pi/2$ with respect to the x-axis. $\mathbf{k}_i^{\pm}$ is the wavevector in layer i with wavenumber $k_i = |\mathbf{k}_i^{\pm}| = \omega\sqrt{\varepsilon_i \mu_0}$, where ω is the incident light frequency, and a harmonic time-dependence of $e^{-i\omega t}$ is assumed on all fields.

After the incidence of light at θ_0, the angle in layer i follows Snell's law, which relates the incident wave to the refracted and transmitted waves.

$$\theta_i = \sin^{-1}\left[\frac{n_1}{n_i}\sin\theta_0\right] \tag{4.17}$$

The phase of the plane wave, or light wave, is given by $e^{i(k_i x \cos\theta_i)}$. The field amplitude in a layer traveling towards the interface is denoted as $\mathbf{E}_i^+$, and the amplitude reflected away from the interface is denoted as $\mathbf{E}_i^-$. $\mathbf{E}_1^+ = \mathbf{E}_0$ and there is no reflection from a semi-infinite layer M. So $\mathbf{E}_M^- = 0$.

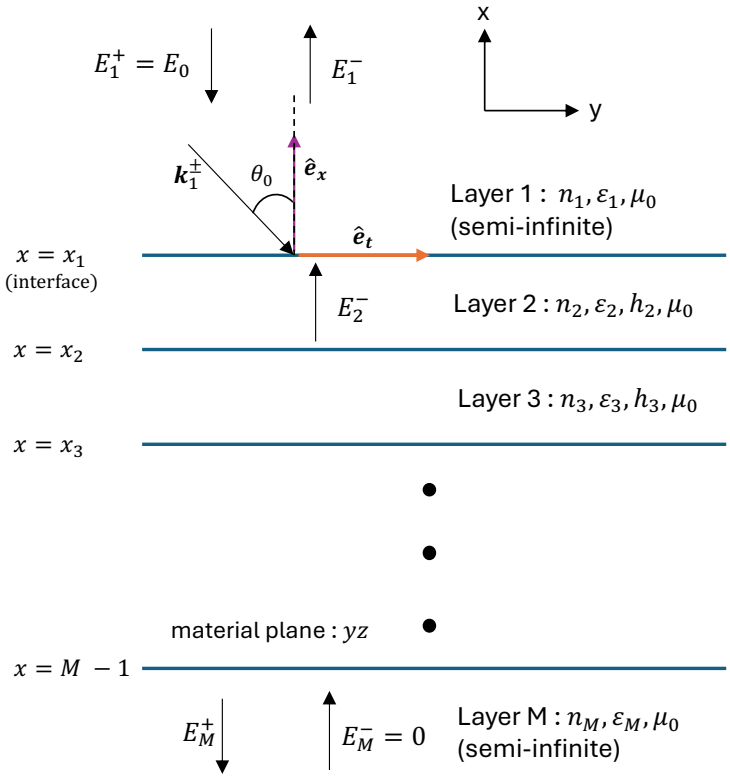

Figure 4.10: Stratified media schematic for M layers with $\hat{\mathbf{e}}_x$ normal direction

The total field in each layer is then given as:

$$\mathbf{E}_i(x) = \mathbf{E}_i^+ e^{ik_i x \cos\theta_i} + \mathbf{E}_i^- e^{-ik_i x \cos\theta_i}$$

Faraday's law for a plane wave states that $\mathbf{B} = n\mathbf{k} \times \mathbf{E}$, so:

$$\mathbf{B}_i(x) = n_i \hat{\mathbf{k}}_i^+ \times \mathbf{E}_i^+ e^{ik_i x \cos\theta_i} + n_i \hat{\mathbf{k}}_i^- \times \mathbf{E}_i^- \cos\theta_i e^{-ik_i x \cos\theta_i}$$

We consider the case of normal incidence with $\theta_0 = 0$. The total field simplifies as:

$$\mathbf{E}_i(x) = \mathbf{E}_i^+ e^{ik_i x} + \mathbf{E}_i^- e^{-ik_i x} \tag{4.18}$$

$$\mathbf{B}_i(x) = n_i \mathbf{E}_i^+ e^{ik_i x} - n_i \mathbf{E}_i^- e^{-ik_i x} \tag{4.19}$$

The boundary conditions at interface x_i between layers i and $i+1$ for the tangential component of the electric field are given by Faraday's law. It requires that there is no discontinuity in the electric field across the interface. The interface in the schematic is along y. Hence:

$$(\mathbf{E}_i(y_i) - \mathbf{E}_{i+1}(y_i)) \cdot \hat{\mathbf{e}}_t = 0 \tag{4.20}$$

The boundary conditions for the tangential component of the magnetic field are given by Ampere's law at the interface. There is no discontinuity here as well.

$$(\mathbf{B}_i(y_i) - \mathbf{B}_{i+1}(y_i)) \cdot \hat{\mathbf{e}}_t = 0 \tag{4.21}$$

There are two boundary conditions for the normal direction ($\hat{\mathbf{e}}_x$) as well, but they are not reported here since they are not used to solve for $\mathbf{E}_R$ and $\mathbf{E}_T$.

Substituting Equations (4.18) and (4.19) into Equations (4.20) and (4.21) respectively gives the following system of $2(M-1)$ equations:

$$E_i^+ e^{ik_i y_i} + E_i^- e^{-ik_i y_i} - E_{i+1}^+ e^{ik_{i+1} y_i} - E_{i+1}^- e^{-ik_{i+1} y_i} = 0 \tag{4.22}$$

$$n_i E_i^+ e^{ik_i y_i} - n_i E_i^- e^{-ik_i y_i} - n_{i+1} E_{i+1}^+ e^{ik_{i+1} y_i} + n_{i+1} E_{i+1}^- e^{-ik_{i+1} y_i} = 0 \tag{4.23}$$

E_1^+ and E_M^- are known quantities, as listed earlier. In Figure 4.10 we have $M-1$ interfaces and two boundary conditions for each interface. The total number of equations is $2(M-1)$, needed to solve for $2(M-1)$ variables, which include the field amplitudes of the middle layers and $\mathbf{E}_R$, $\mathbf{E}_T$. This can be solved through a linear system $\mathbf{A} \cdot \mathbf{E} = \mathbf{b}$ to get $\mathbf{E}_R$ and $\mathbf{E}_T$.

$$\mathbf{A} \cdot \mathbf{E} = \mathbf{b} \tag{4.24}$$

$$\begin{bmatrix} A_{1,1} & A_{1,2} & A_{1,3} & \cdots & A_{1,2M-2} \\ A_{2,1} & A_{2,2} & A_{2,3} & \cdots & A_{2,2M-2} \\ A_{3,1} & A_{3,2} & A_{3,3} & \cdots & A_{3,2M-2} \\ \vdots & \vdots & \vdots & \ddots & \vdots \\ A_{2M-3,1} & A_{2M-3,2} & A_{2M-3,3} & \cdots & A_{2M-3,2M-2} \\ A_{2M-2,1} & A_{2M-2,2} & A_{2M-2,3} & \cdots & A_{2M-2,2M-2} \end{bmatrix} \begin{bmatrix} E_R \\ E_2^+ \\ E_2^- \\ E_3^+ \\ \vdots \\ E_{M-1}^+ \\ E_{M-1}^- \\ E_T \end{bmatrix} = \begin{bmatrix} -1 \\ -n_1 \\ 0 \\ 0 \\ \vdots \\ 0 \\ 0 \\ 0 \end{bmatrix} \tag{4.25}$$

To solve the matrix, the following additional parameters need to be determined: n_i, C, k_i. The ef-

fective refractive index of a stratified medium layer is determined by the average dipole of plasmonic colloids through its effective permittivity.

$$n_i = \sqrt{\frac{\varepsilon_i}{\varepsilon_0}} = \frac{1}{\sqrt{\varepsilon_0}}\sqrt{\varepsilon_f + \frac{N}{V}C} \tag{4.26}$$

$C = \langle p \rangle / E_0$ is the dielectric capacitance. C can be calculated from MPM or other optical simulation methods.

k_i in the exponential term is the wavenumber, calculated as $k_i = \omega\sqrt{\varepsilon_i \mu_0}$. We know the effective refractive index is $n_i = \sqrt{\frac{\varepsilon_i}{\varepsilon_0}}$. Substituting this into k_i gives:

$$k_i = n_i k_0$$

Hence, the wavenumber in any layer i can be calculated by multiplying the wavenumber in vacuum by the layer's effective refractive index.

Using these and solving the system of equations gives $\mathbf{E}_R$ and $\mathbf{E}_T$.

If the incident light is not at normal incidence (represented by θ_i), the boundary conditions will change. s- and p-polarization will no longer be the same. When the incident light is polarized perpendicular to the plane of incidence, it is s-polarized. In this case, $\hat{\mathbf{E}}_0 = -\hat{\mathbf{e}}_z$ and the boundary conditions are:

$$E_i^+ e^{ik_i y_i \cos\theta_i} + E_i^- e^{-ik_i y_i \cos\theta_i} - E_{i+1}^+ e^{ik_{i+1} y_i \cos\theta_{i+1}} - E_{i+1}^- e^{-ik_{i+1} y_i \cos\theta_{i+1}} = 0 \tag{4.27}$$

$$\begin{aligned} n_i E_i^+ \cos\theta_i e^{ik_i y_i \cos\theta_i} - n_i E_i^- \cos\theta_i e^{-ik_i y_i \cos\theta_i} \\ -n_{i+1} E_{i+1}^+ \cos\theta_{i+1} e^{ik_{i+1} y_i \cos\theta_{i+1}} + n_{i+1} E_{i+1}^- \cos\theta_{i+1} e^{-ik_{i+1} y_i \cos\theta_{i+1}} = 0 \end{aligned} \tag{4.28}$$

If the incident light is polarized parallel to the plane of incidence, it is said to be p-polarized with $\hat{\mathbf{B}}_0 = \hat{\mathbf{e}}_z$. The boundary conditions are:

$$n_i E_i^+ e^{ik_i y_i \cos\theta_i} + n_i E_i^- e^{-ik_i y_i \cos\theta_i} - n_{i+1} E_{i+1}^+ e^{ik_{i+1} y_i \cos\theta_{i+1}} - n_{i+1} E_{i+1}^- e^{-ik_{i+1} y_i \cos\theta_{i+1}} = 0 \tag{4.29}$$

$$\begin{aligned} E_i^+ \cos\theta_i e^{ik_i y_i \cos\theta_i} - E_i^- \cos\theta_i e^{-ik_i y_i \cos\theta_i} \\ -E_{i+1}^+ \cos\theta_{i+1} e^{ik_{i+1} y_i \cos\theta_{i+1}} + E_{i+1}^- \cos\theta_{i+1} e^{-ik_{i+1} y_i \cos\theta_{i+1}} = 0 \end{aligned} \tag{4.30}$$

System of equations then need to be resolved. This brute force approach requires solving a large number of equations. A cheaper alternative to calculate these reflectance and transmittance coefficients could be the transfer matrix or Jones matrix (K_i) approach. It relates the field coefficients in one layer to the next through a 2×2 matrix. If there are N layers, N matrix ($K_N \cdots K_2 K_1$) can be multiplied to calculate $\mathbf{E}_R$ and $\mathbf{E}_T$. While this is not discussed in detail and demonstrated in this chapter, future work involves exploring this technique as we simplify the method to calculate reflectance and transmittance coefficients. Simplifying the method with faster matrix calculation will help speed-up the following optimization calculations. Details for taking the gradient of reflectance through adjoint and its propagation will be discussed in a separate venue.

4.2.2 Optimization

For Figure 4.3, the plasma frequency ω_p and ε_∞ are bounded between 1 and ∞, γ is bounded between 0.1 and ∞, and the particle radius a is constrained between 0.1 and 2. Each layer's

parameters start from $(a_0, \omega_{p,0}, \gamma_0, \varepsilon_{\infty,0}) = (1, 1, 0.1, 1)$ and are offset from each other by a random number from a uniform distribution $\sim U(-0.025, 0.025)$. As a result, the layers do not start with the same set of parameters, but the parameters are close in value.

For Figure 4.5 with stop-band functionality, same as Section 3.5.3 in Chapter 3, the plasma frequency ω_p is bounded between 0.1 and ∞ and the particle radius a is constrained between 0.1 and 2. Same as in Chapter 3, the choice of initial values for ω_p and a is the same (Section 3.3), and the parameters γ and ε_∞ are fixed at 0.1 and 1, respectively.

4.3 Conclusions

In this chapter, we were able to build on our inverse design framework to design plasmonic NP-based materials with isotropic optical extinction. We demonstrated it for a single-NP extinction target and stopband functionality, and tuned those targets to varying degrees to test our framework. We derived a linear system of equations to solve for reflectance at normal incidence and laid out a starting point for non-normal incidence angles. Since we are able to calculate reflectance and transmittance, we next want to optimize using them as the figure of merit with our modified objective function for both grazing and normal incidence fields. We want to decompose the overall extinction response similarly to see if the response is still isotropic and what kind of structural and dielectric features form a material with isotropic reflectance.

For non-normal incidence angles, propagating the gradient of the objective function of reflectance, which depends on θ_0, directly with respect to design parameters and dipoles is a complex and involved effort that is in progress. Being able to demonstrate this optimization with direct dependence on θ_0 will move the work further towards the goal of designing plasmonic materials that are agnostic to the incident angle.

We have also considered only isotropic materials for calculating reflectance. The next step is to set up a stratified medium calculation for an anisotropic material. The angle of incidence can additionally be accounted for here, and the figure of merit can be propagated for the optimization of an anisotropic material.

Once this optimization framework is developed for direct dependence on θ_0, the ability to optimize with different angles will allow us to design magnetoplasmonic NPs. As mentioned earlier, magnetoplasmonic NPs such as $Ag@Fe_3O_4$ show different solution colors when illuminated with light at different angles. Controlling this will allow us to optimize for the color of plasmons and study the corresponding structure-function properties.

Chapter 5

Reaction Pathway Analysis of PET Deconstruction via Methanolysis and Tertiary Amine Catalysts[1]

5.1 Abstract

Polyethylene terephthalate (PET) is a type of polymer frequently used in plastic packaging that significantly adds the amount of plastic waste found in landfills. One of the ways to recover valuable raw materials from postconsumer plastic is by depolymerizing the PET into its monomeric constituents, which are dimethyl terephthalate (DMT) and ethylene glycol (EG). PET depolymerization is often done in methanolysis with the help of acid or base catalysts. Tertiary amine is one of the most attractive base catalysts for PET depolymerization in methanolysis since it does not lead to generation of potentially environmentally harmful waste, unlike metal-based catalysts. However, the mechanism by which tertiary amine catalyzes PET depolymerization in methanolysis remains unexplored. Developing a detailed mechanistic understanding of this process is important for improved of plastic upcycling, since it opens the possibility of employing various cheaper and more environmentally friendly reaction conditions. Using DFT and transition state analysis, we show that in the presence of tertiary amine catalysts, methanolysis of PET consists of multiple discrete-steps reaction rather than a single concerted step. Furthermore, by comparing our calculations to recent experimental results, we were able to rationalize that the DMT yield from the depolymerization process by relating it to charge polarization within tertiary amine catalysts, thus opening a pathway to identifying atomic descriptors for future catalyst design.

5.2 Introduction

Plastic is made of synthetic polymeric materials with a wide range of applications in our everyday life from textiles to packaging.[159] Since the 1950s, there have been more than 10 billion metric tons of plastic produced, with more than 80% found to have ended up in landfills as waste.[160] With only less than 10 % of the postconsumer waste having been recycled,[161] accumulation of plastic waste is a pollutant that has become harmful to both animals and humans.[162]

Thermoplastic resin polyethylene terephthalate (PET) used primarily in packaging containers, cups or bottles accounts for 10 % of the global plastic resin production.[163] PET also has a high recycling rate of 20 % in the US making it an important polyester of interest for polymer upcycling.[159] PET can be recycled through several methods, including reactive extrusion, mechanical recycling, energy recovery via incineration or chemical recycling through depolymerization to its constituent monomers.[164] One approach within chemical recycling that has gained significant traction for PET depolymerization is solvolysis, which includes methods such as hydrolysis,[165–168] methanolysis,[169–171] glycolysis,[172–174] ammonolysis,[175] aminolysis[176] or in the presence of enzymes.[19]

[1]This chapter was reproduced with permission from Rishabh Sanghavi, Nadia N. Intan, Shaoqu Xie, Hongfei Line and Jim Pfaendtner. Reaction Pathway Analysis of PET Deconstruction via Methanolysis and Tertiary Amine Catalysts. J. Phys. Chem. A 2024, 128 (29), 5883–5891. Copyright 2026 American Chemical Society.[158]

Based on reaction conditions such as heat, catalyst, and solvolysis method, PET breaks to form either terephthalic acid (TA), dimethyl terephthalate (DMT), or bis(hydroxyethyl) terephthalate (BHET) monomer.[170,173,177,178]

Methanolysis of PET is a transesterification reaction that depolymerized PET into ethylene glycol (EG) and DMT monomer that are produced in accordance with the following reaction schematic :

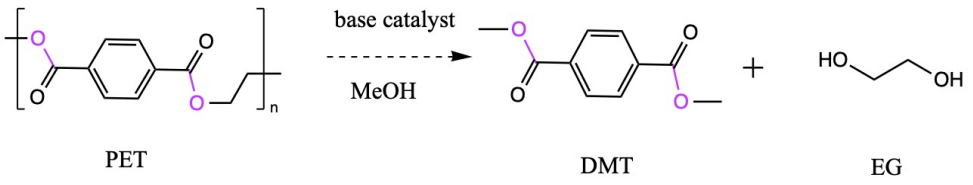

Scheme 5.1: Depolymerization of PET via methanolysis to form DMT and EG

Both EG and DMT monomers in Scheme 5.1 can be recycled back to reform polymer of similar quality as PET.[179] Unfortunately, alcoholysis of PET is a kinetically slow reaction without a catalyst. Much lower yield of DMT and EG are reported for methanolysis of PET in absence of catalyst.[171] It is reported that at 200 ^{0}C in absence of catalyst, methanolysis of PET in 100 ml methanol results in 2.9 % and 3.6 % yield of DMT and EG respectively. Under the same conditions but with the addition of 50 mg of aluminum triisopropoxide (AIP) as catalyst, the yields of DMT and EG increase to 67.3 % and 68.3 % respectively.[171]

Introduction of base catalysts results in the increase of the electrophilicity of the ester group, which results in the ester becoming more prone to nucleophilic attack by the oxygen in the methanol solvent (the ester bond is drawn in purple in Scheme 5.1. The reaction between the ester group of PET and methanol solvent results in the creation of a tetrahedral intermediate, which facilitates proton transfers from methanol to ester. Ester and methanol reaction generates a water molecule in addition to a resultant ester that will rearrange to form ester product and regenerate the catalyst.[180]

Several experimental studies have extensively studied PET methanolysis using basic catalysts such as potassium carbonate,[170] zinc acetate, magnesium acetate or cobalt acetate.[181–184]However, reports on the effectiveness of methanolysis as a means to depolymerize PET are varied and are dependent on experimental conditions some of which include type of metal-based catalyst, molecular weight of PET and use of vapor or supercritical methanol for methanolysis. *In lieu* of using metal-based catalysts during methanolysis process to depolymerize PET, a more environmentally friendly alternative are organic amine-based catalysts. Amines, which are Lewis bases, are known to accelerate the transesterification reactions as catalysts.[185] These hydrogen atoms in both primary and secondary amines may react with the carbonyl group of PET, which results in the amidation process that leads to the formation of amide. The resulting amides are not as strong Lewis bases compared to the original amines.

In contrast, tertiary amines have no hydrogen atoms attached to nitrogen thus, do not readily lead to amidation reactions to form a less basic amide. However, the basicity of tertiary amine catalysts is significantly affected by steric hindrance of nitrogen, which can have an opposing effect on catalyst reactivity.[186] Hence, there are competing factors that make tertiary amines both beneficial and

detrimental as catalysts for PET depolymerization. However, the exact mechanism in which the tertiary amine catalyzes PET depolymerization is yet to be understood, much less the knowledge on how to choose the suitable tertiary amine molecules help catalyze the PET depolymerization reaction. In this study, our goal is to attain a comprehensive understanding of how a tertiary amine catalyzes the PET depolymerization and unveil the important factors of the tertiary amines that determine their efficiency. We use density functional theory (DFT) based methods to study the depolymerization mechanism in the presence of various tertiary amine catalysts. In this study, we select six tertiary amines with recently published experimental data for this reaction.[187] We study PET depolymerization via methanolysis to determine its reaction mechanism. We also explore the effect of methanol solvent and tertiary amine catalysts on the reaction energetics. We then compare our calculated results to that of experimental yield in which we unveil the correlation between the experimental yield and the charge on the N atom of the protonated tertiary amine catalysts. Finally, we propose a descriptor in which prediction on the efficiency of potential catalysts can be used to accelerate the discovery of future catalysts.

The rest of the paper is organized as follows: first, we describe the computational procedure used in this study. Following this, we present our results in which we investigate the PET depolymerization reaction mechanism. We systematically increased the complexity of our system to understand the effect brought by methanol solvent and tertiary amine catalysts on the energetics of PET depolymerization reaction. We finally compare our computational results to previously published experiments to gain insights into factors that affect yield in PET depolymerization. In the end, we provide a quick discussion in which we propose a descriptor that can be employed to quickly predict the effectiveness of other tertiary amines as potential catalysts for PET depolymerization.

5.3 Methods

DFT calculations were carried out using the Gaussian16 software package.[188] Geometry optimizations were performed using the Minnesota M06-2x[189] hybrid exchange–correlation functional together with the 6-31G (d,p)[190,191] basis set for all atoms. The M06-2x hybrid exchange–correlation functional was used because of its wide applications in the main group for thermochemistry and kinetics.[189] The effect of methanol solvent on the depolymerization reaction was studied through the incorporation of the polarizable continuum model (PCM) using the self-consistent reaction field method keyword.[192–196] Prior to precise determination of transition states, reaction mechanisms was explored with constrained geometry optimizations[40] and eventually saddle points on the potential energy surface were determined with full transition state optimization (keyword=TS). Transition states were verified by confirming that there was only one imaginary frequency for the resulting vibrational frequencies calculated (keyword=freq). They were further verified by following the reaction path by performing intrinsic reaction coordinate (IRC)[197] (keyword=IRC) calculations followed by geometry optimization after the IRC calculation is complete. We provide example input files for transition state, intrinsic reaction coordinate scan and geometry optimization calculations in Section B.4

We describe the methanolysis reaction primarily with a simplified set of descriptors (bond distances) that undergo significant change. As shown in Figure 5.1, R1 defines the distance between ester carbonyl carbon and methanol oxygen, while R2 denoted distance between ester oxygen and methanol hydrogen. Later in the study, we added tertiary amine catalyst, which were placed adjacent to the transition state, but not obstructing the reaction pathway. The atomic charges and proton transfer energy were calculated using the CHELPG method[198] at the M06-2x[189] functional and the 6-311++g (d, p)[199,200] basis set. GaussView and PLUMED *version 2.8*[201,202] were used for

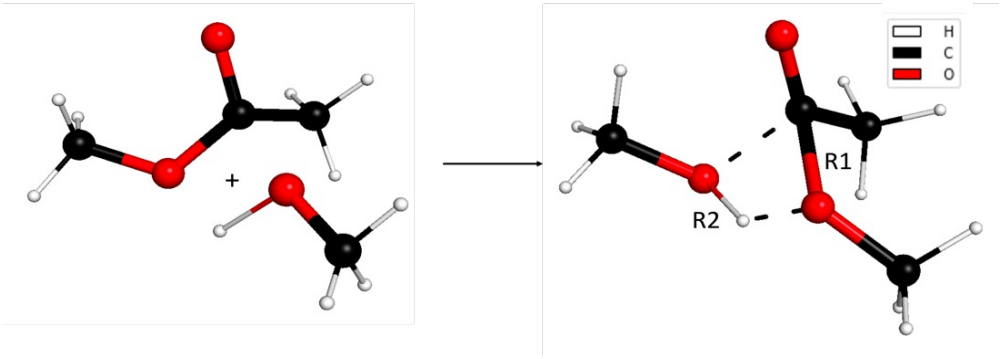

Figure 5.1: Key atomic distances used to describe ester methanolysis reactions in this study.

bond analysis. We note that 6-311++g (d, p) has been used previously to calculate atomic charges using CHELPG method [203,204] and is used additionally for geometry optimization calculations. [205]

5.4 Results

5.4.1 Methyl Ester Base Case: Obtaining Transition State Structure

The methanolysis reaction is complex, requiring multiple concerted bond breaking and forming events. We initially performed a detailed characterization of the methanolysis of methyl ester with a goal of characterizing the simplest methanolysis reaction possible and learning if the model transition state from that reaction could be applied to the study of PET methanolysis. Using constrained geometry optimization, we studied three different approaches of the methanol molecule to the ester linkage, by varying the corresponding distances R1 and R2 in a stepwise fashion $\Delta R = 0.1$) as shown in Figure 5.2.

We first study the scenario in which the methanol oxygen attacks the carbonyl linkage at the carbon atom (R1). (Figure 5.2a) Note that here, the distance between the methanol hydrogen and ester oxygen is monitored, but not controlled (R2 is shown on secondary y-axis in Figure 5.2a). Decreasing the distance progressively increases the potential energy until the energy goes through a maximum around R1=1.2 Å, at which point R2 also drops precipitously. Using the structure with an energy maximum as an initial guess, we performed multiple rounds of attempt/refinement to identify a TS structure with different algorithms for determining saddle points. None of the attempts were successful. We next attempted the same study, but constraining and varying R2 while monitoring R1 (Figure 5.2b). Here, the system never passes through any maximum of energy and there are no apparent reactions occurring. Monitoring the resulting structures clearly indicates the methanol is not oriented in a fashion that can facilitate the required concerted bond breaking and formation events. Hence, R1 and R2 alone are not suitable proxies for the reaction coordinate and therefore cannot be scanned independently to determine an initial guess for transition state finding calculations.

Next, we simultaneously scan both the R1 and R2 together using multiple constraints in the geometry optimization. We established initial distances of R1 and R2 to 2.5 Å and 2.1 Å, respectively, we then simultaneously reduce the distances of both R1 and R2 by steps of 0.1 Å. The relative energy from this simultaneous scan of R1 and R2 is shown in Figure 5.2c. As shown, the relative energy peak 42.6 kcal/mol is observed when R1 and R2 are of 1.7 Å and 1.3 Å, respectively. This

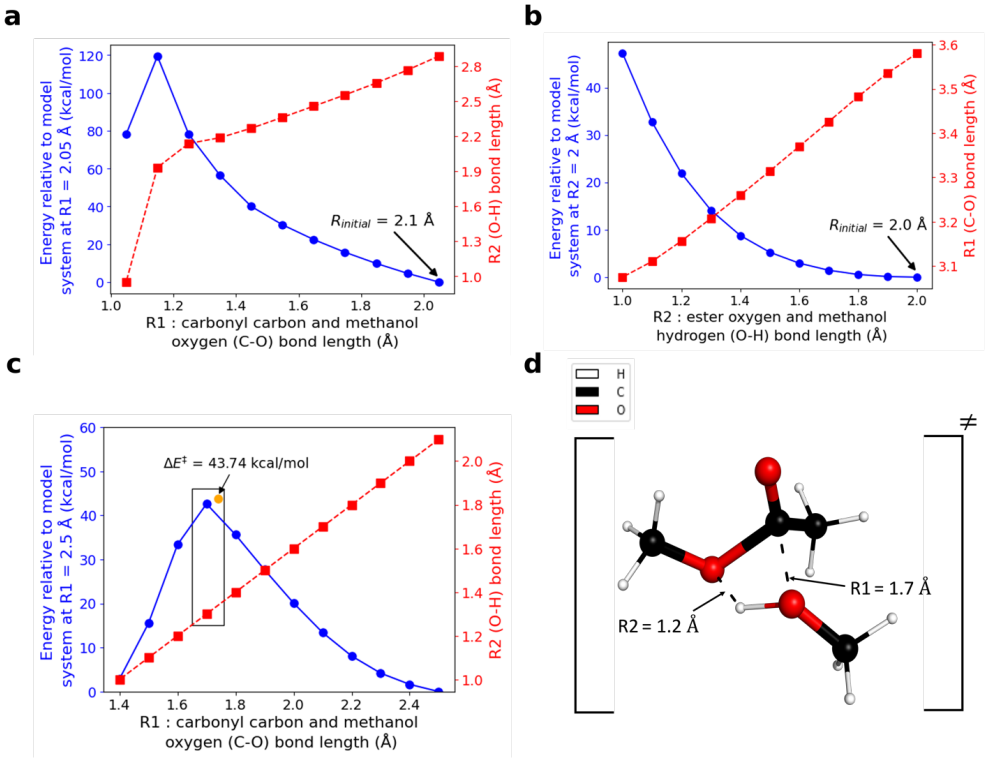

Figure 5.2: The changes in energy and bond length as the result of stepwise scan of a) C-O distance between carbonyl carbon and methanol oxygen (R1), b) O-H distance between ester oxygen and methanol hydrogen (R2), c) R1 and R2 together, where the distances of both R1 and R2 were simultaneously reduced by 0.1 Å. The black box signifies the maximum energy that was achieved when the C-O R1 distance = 1.7 Å and O-H R2 distance = 1.3 Å, respectively. The structure of this maximum energy was used as the initial guess for transition state finding. The transition state structure is shown in d).

configuration is used to search for a transition state and the resulting calculation shows a structure with very similar energy and one imaginary vibrational mode (-1179.9 cm^{-1}). The TS structure (Figure 5.2d) is extremely similar in geometry (R2 is only adjusted by 0.1 Å) and energy (the TS structure is 1.1 kcal/mol higher in energy at 43.7 kcal/mol). We also confirm the configuration at the transition state by doing an intrinsic reaction coordinate scans from the transition state to both the reactant and product states.

For the remainder of this study, we use the transition state configuration shown in Figure 5.2d as the starting point for other systems involving more complex models, such as when we replace the methyl ester with a more realistic representation of PET. In the following sections, we study different surrogates of PET decomposition with a longer alkyl chain length attached like ethyl benzoate, and then introduce a set of tertiary amine catalysts explicitly into the system to study the effect of catalysts on PET depolymerization. Finally, the solvent effect on depolymerization reaction energetics would also be discussed.

5.4.2 Increasing Surrogate Complexity

We now replace methyl ester with a more realistic representative of PET, ethyl benzoate. To determine the ethyl benzoate methanolysis reaction mechanism we began by using the transition state structure described above, we replaced the methyl group connected to the C=O linkage with a benzyl ring. We froze the coordinates of all four atoms involved in the concerted bond breaking and forming and performed a geometry optimization and frequency calculation. The structure showed one imaginary vibrational mode of similar frequency to the TS described above.(Section B.1) Following this, we determined a saddle point TS structure and used the IRC scan as a means to obtain a detailed mechanistic understanding of the methanolysis process while verifying that the obtained TS structure leads to the correct reactants and products.

The reaction between ethyl benzoate and methanol is shown in Figure 5.1a, which progress we track by monitoring the R1 and R2 bonds. The R1 and R2 bonds have been defined in Figure 5.1. Further, we also track the evolution of the improper dihedral formed by the four key atoms defined by R1 and R2, as shown in Figure 5.1a. The improper dihedral is thus defined as the angle between the i, j, k, l planes, where i, j, k, and l refers to methanol hydrogen, ester oxygen, carbonyl carbon and methanol oxygen, respectively.

From Figure 5.3b, we can deduce the order of events in the methanolysis reaction mechanism between ethyl benzoate and methanol to be as follows:

1. The reaction begins as hydrogen of methanol breaks away from methanol oxygen towards ester oxygen leading to decrease in bond distance D1 (blue),
2. Simultaneously, the distance between methanol oxygen and methanol hydrogen increases as shown by D3 (green), until D1 and D3 curves intersect at transition state,
3. After reaching the transition state, the hydrogen continues to move towards ester oxygen and breaks away from methanol, as shown by further decrease in the D1 distance. This corresponds to a decrease in the relative energy.
4. The carbonyl carbon and methanol oxygen then move closer towards each other as shown by the decrease in the D2 (yellow) distance.
5. The C-O ester bond in ethyl benzoate breaks as the carbonyl carbon and ester oxygen move away from each other, shown by the increase in D4 (red). And finally,

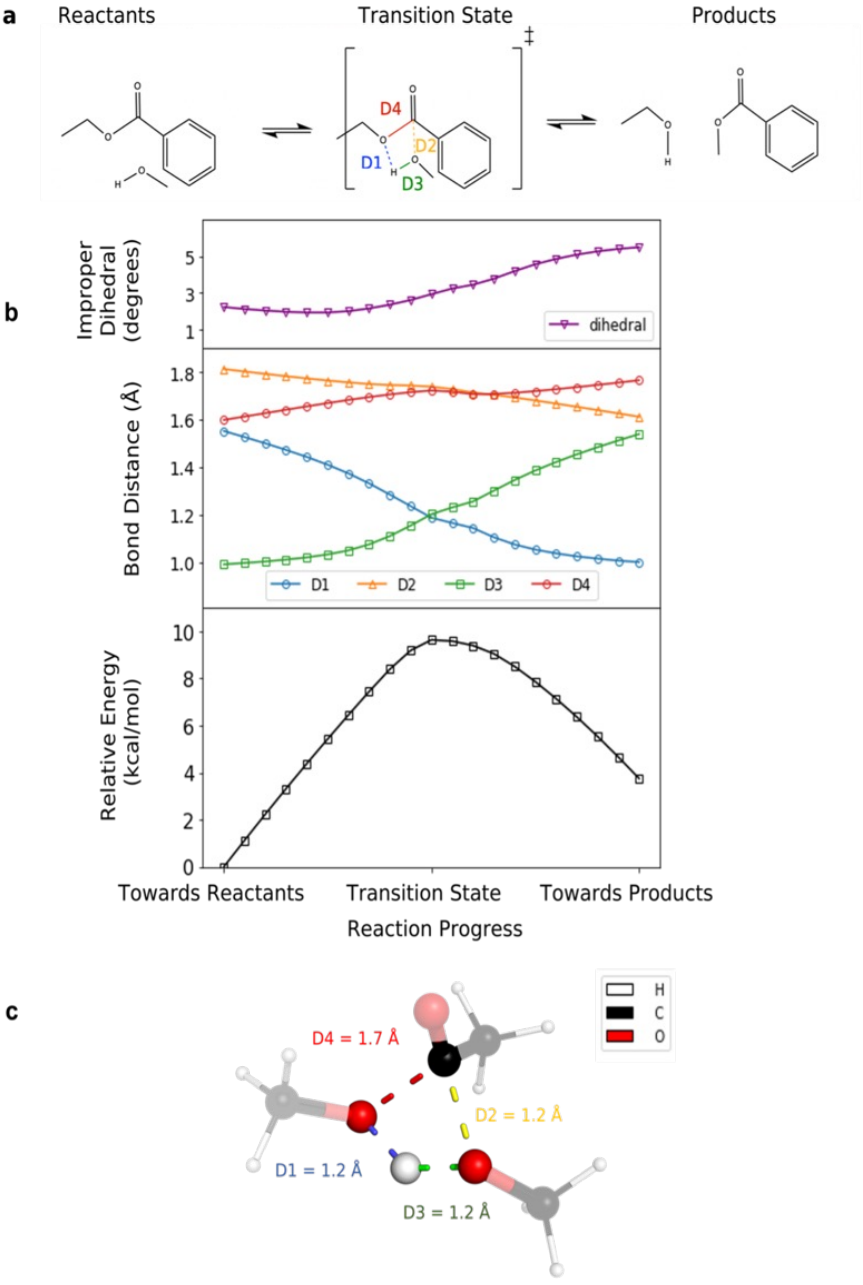

Figure 5.3: a) Overall reaction schematic for ethyl benzoate during methanolysis of ester. The reaction progress is tracked through the evolution of bonds D1 - D4. b) The corresponding bond distances (Å), improper dihedral (degrees) and relative energy (kcal/mol) of reaction with respect to 11^{th} intrinsic reaction coordinate step going towards reactants. And c) the tetrahedral complex model showing bonds D1 - D4.

6. The carbonyl carbon then forms a bond with methanol oxygen to form products methyl benzoate and ethanol.

Figure 5.3b also shows that improper dihedral changes very slightly from ~2^0 to ~6^0 moving from reactant to product complex. This change is relatively small, indicating that the improper dihedral is relatively unchanged in planar configuration of the four atoms described in step 3.) above. The transition state for the methanolysis reaction between ethyl benzoate and a methanol is formed in a concerted fashion as all 4 key bonds in the tetrahedral intermediate (D1-D4) are broken and formed in the same step, as shown in Figure 5.3c.

In Figure 5.3b, we note that the labels 'Towards Reactants' and 'Towards Products' refer to the relative energy of 11^{th} IRC step in the direction of reactants and products respectively. In Gaussian 16, IRC by default takes 10 steps from the transition state. Including the transition state, the 'Towards Reactants' and 'Towards Products' are the 11^{th} IRC step in their respective directions. Each step is represented by a square marker in the relative energy plot in Figure 5.3b.

5.4.3 Effect of Tertiary Amine Catalysts on the PET methanolysis

In this section, we explore role of tertiary amine catalysts in the transesterification reaction of ethyl benzoate and methanol. The work described above indicates that proton transfers from methanol directly to ethyl benzoate oxygen to break the ester bond as detailed in Figure 5.3. Transesterification occurs through a single concerted step. In the model system, the catalyst is on the opposite side of the aromatic ring of ethyl benzoate away from methanol such that it does not directly participate in the proton transfer step of the reaction. It has been proposed that tertiary amine catalysts act as Lewis base in methanol due to free electrons of N atom and could possibly form a hydrogen bond between N of catalyst and H of aromatic ring in ethyl benzoate and another hydrogen bond between H atom on methyl adjacent to N atom and carbonyl carbon to activate the ester bond.[187] Therefore, the role of this catalyst in lowering the activation energy could primarily be expected to be resulting from the activation of ester from these hydrogen bonds.

To understand this effect we introduce a list of tertiary amine catalysts whose effectiveness in depolymerizing PET have been investigated experimentally.[187] The list includes linear, cyclic, aromatic, and diamines, whose chemical structure is given in Figure 5.4. Reported experimental yield of DMT, EG and total yield are shown in Table 5.1 for the list of catalysts. Table 5.1 does not include values for linear TMA as it is not part of the experimental study.[187]

Using ethyl benzoate as representative model for PET, the overall energy landscape of the PET depolymerization through methanolysis in the presence of tertiary amine catalysts are shown in Figure 5.5.

Figure 5.5 clearly shows that the presence of tertiary amine successfully lowered the activation barrier for the transesterification of ethyl benzoate by methanol thus, showing its promising potential to catalyze PET depolymerization in methanolysis. Further, the effectiveness of the tertiary amine in lowering the activation barrier in the ascending order from the lowest activation barrier is TEEDA, DMA, aromatic TMA, TEA, linear TMA, and NMP, respectively. The ordering of the tertiary amine in catalyzing the reaction in Figure 5.5 can be clearly classified based on the structures of the tertiary amines as defined in Figure 5.4, where the lowest transition state is obtained by the diamine type of tertiary amines, that is followed by aromatic, linear, and cyclic types, respectively.

However, we stress that the energies for the transesterification reaction of ethylbenzoate shown in

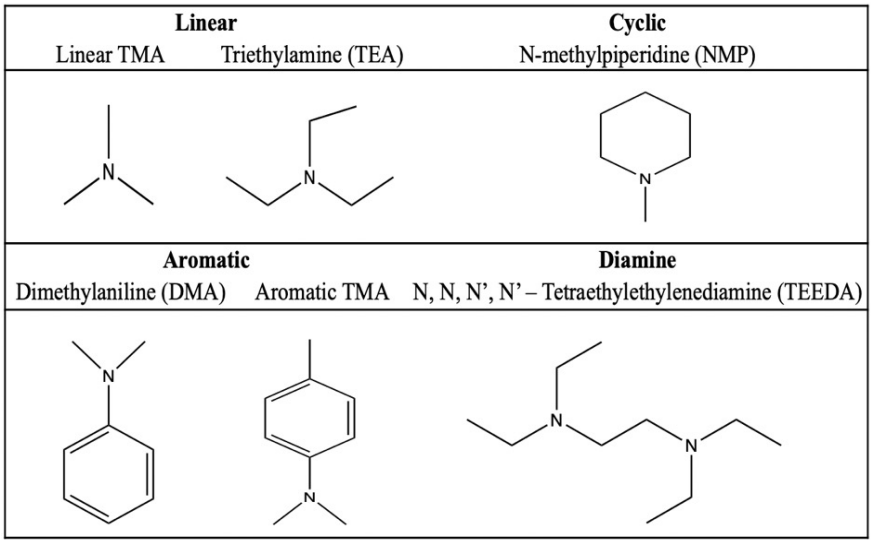

Figure 5.4: Six different tertiary amines used in this study as representatives to understand the effect of amine catalysts on PET depolymerization reaction by methanolysis at the atomistic level.

Figure 5.5 were obtained from calculations in vacuum. PET methanolysis in experiments however occurs in methanol solvent. Product yield results in Table 5.1 were reported for reaction using tertiary amine methanol solution. Hence, we introduce methanol solvent into our study to study the effect of solvation to the PET depolymerization through methanolysis.

5.4.4 Effect of Solvation

To study the effect of methanol on the PET depolymerization reaction during methanolysis, methanol solvent is introduced into the system implicitly. Methanol molecule and ethyl benzoate are present in the system as reactants along with tertiary amine catalyst. The energy landscape of the ethyl benzoate transesterification reaction in the presence of tertiary amines in implicitly treated methanol is shown in Figure 5.6.

Figure 5.6 shows that activation energy barriers for the transesterification reaction in implicit methanol solvent are very similar to those of in vacuum; thus, indicating that the implicit methanol solvent does not have any effect in the transesterification reaction energy barrier.

Unlike in the vacuum calculations, Figure 5.6 shows that no correlation between the structure of tertiary amines and energy at the transition state. Furthermore, the energies at the transition state are indistinguishable for DMA, aromatic TMA and TEA catalysts. There is no obvious reason why the addition of the implicit solvent model should re-order the relative ranking of catalytic effects observed in the reaction mechanism. These results with implicit solvation for the overall methanolysis reaction and a neutral catalyst thus suggest that the key step that defines the rate in the PET depolymerization during methanolysis must lie elsewhere. Based on this interpretation, we next explored the scenario in which the proton transfer step from methanol to ethyl benzoate in the PET depolymerization reaction involves the tertiary amine catalysts.

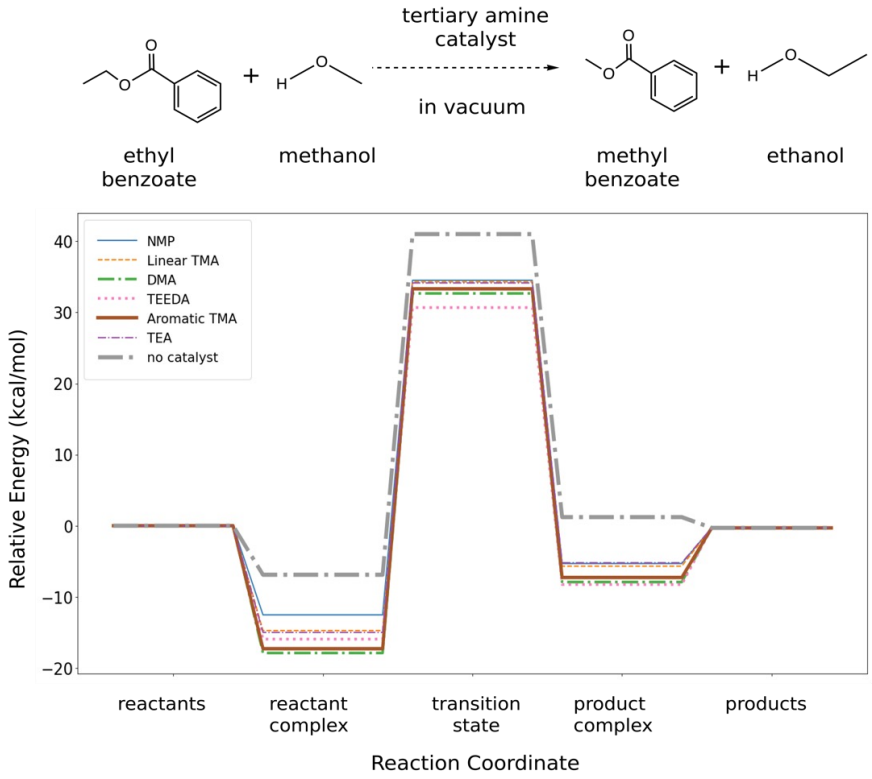

Figure 5.5: The effect of tertiary amine on the energy landscape of transesterification reaction between ethylbenzoate and methanol in vacuum. The energies for reactant, transition, product states were calculated through geometry optimizations. Energies for the reactant complex and product complex were obtained through geometry optimization of the final IRC structures in each respective direction and the reactant/product energies are the summation of the individual species energies.

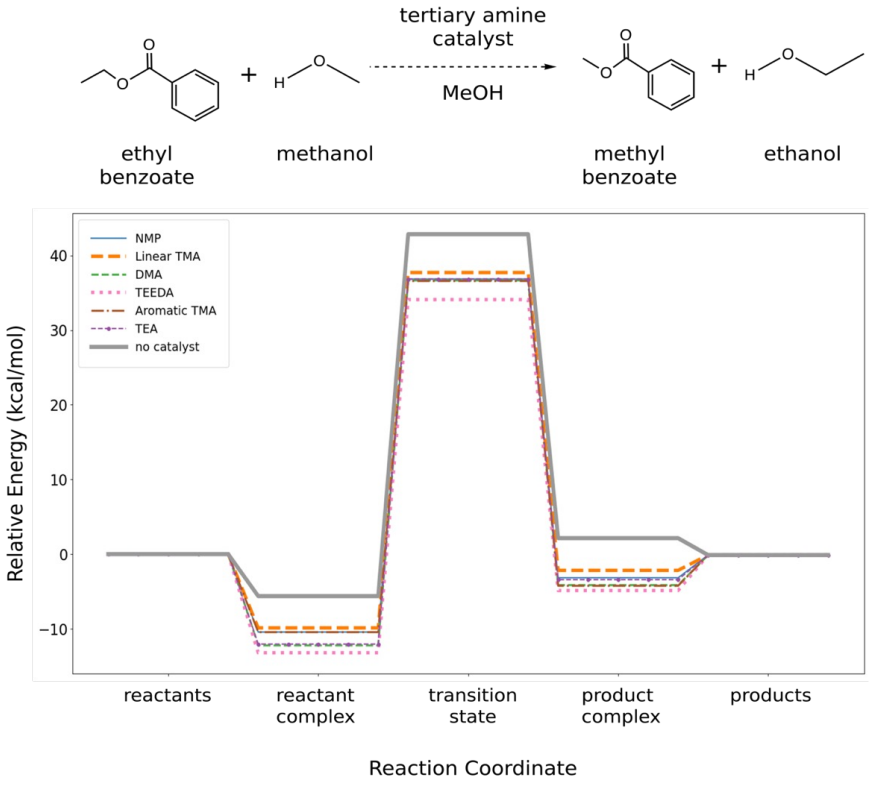

Figure 5.6: The effect of tertiary amine on the energy landscape of transesterification reaction between ethylbenzoate and methanol in implicit methanol solvent. The energies for reactant, transition, product states were calculated through geometry optimizations. Energies for the reactant complex and product complex were obtained through geometry optimization of the final IRC structures in each respective direction.

Table 5.1: Yields of DMT, EG and total yield from depolymerization of 0.1 g PET bottle strips in 20 ml of 0.20 M tertiary amine methanol solution at 160 ^{0}C, 1 hour reaction duration at 700 rpm.[187] Yield is calculated from moles of DMT and EG after the reaction in accordance with the formula shown in Section B.2

		Yields (%)		
Catalyst	Catalyst Configuration	DMT	EG	DMT+EG
NMP	cyclic	100	100	200
TEA	linear	91.2	74.5	165.7
Aromatic TMA	aromatic	25.8	14.3	40.1
DMA	aromatic	6.4	6.8	13.2
TEEDA	diamine	80.1	85.1	165.2

5.4.5 Catalysts Involvement in the Proton Transfer Step

In this section, we explore the scenario in which the tertiary amine catalysts are actively involved in the transesterification reaction of ethyl benzoate and methanol via proton transfer.[206] Rather than having the transesterification as one single concerted step, we split the reaction into two successive parts: first, the proton transfer from the methanol to the ethyl benzoate, which then is followed by the breaking of the ester bond. Furthermore, in the first step, instead of having the proton to transfer directly from the methanol oxygen to the ester of the ethyl benzoate, the proton would first transfer to the amine catalyst before subsequently transferred to the ethyl benzoate. The two discrete steps of the proton transfer in the transesterification of ethyl benzoate in methanol is given in Scheme 5.2.

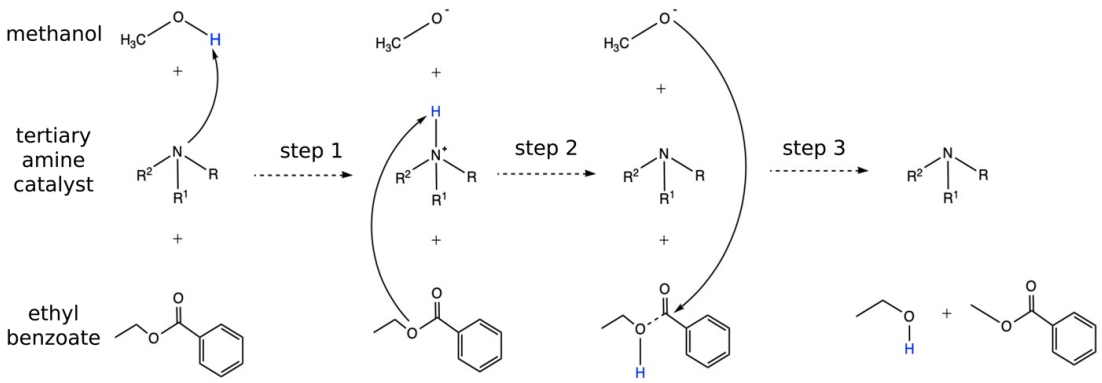

Scheme 5.2: Proposed steps for proton transfer during transesterification of ethyl benzoate in methanol

Although the reaction mechanism presented in Scheme 5.2 seems similar to that presented in fig. 5.2a, where the scanning of R1 bond independent of the R2 results in an unreasonable TS structure due to the very high TS energy of 120 kcal/mol, this reaction pathway merits another exploration as we now have tertiary amine catalysts that are actively involved in the transesterifi-

cation reaction. The reaction energy for the proton transfer from methanol to the tertiary amine as defined by step 1 in Scheme 5.2 in both vacuum and implicit methanol is given in Table 5.2. Note that, in the proton transfer energy calculations, we restrained either the N-H bond in the protonated catalyst, the C-O bond in methanol, or both the N-H and C-O bonds simultaneously during the geometry optimization step.

Table 5.2: The proton transfer energy as defined by Step 1 in Schematic 2 that were calculated using M06-2x/6-311++G(d,p), experimental yield of DMT product from PET depolymerization as obtained from[187] and the charge on N atom in the protonated tertiary amine catalysts as calculated by CHELPG using the M06-2x[189] functional and the 6-311++G (d, p)[198,199] basis set.

		Proton Transfer Energy (kcal/mol)			
Catalysts	Catalyst Configuration	in vacuum	in implicit methanol	Experimental Yield of DMT (%)[30]	Charge on N atom in protonated tertiary amine calculated in implicit methanol
NMP	cyclic	27.7	14.9	100	0.19
Linear TMA	linear	33.4	22.2	-	0.13
TEA	linear	32.8	21.8	91.2	0.16
TEEDA	diamine	29.9	22.5	80.1	-0.14
Aromatic TMA	aromatic	33.3	25.7	25.8	-0.28
DMA	aromatic	26.7	21.1	6.4	-0.30

Unlike in Figure 5.6 where the incorporation of the implicit methanol solvent does not affect the activation energy barriers, Table 5.2 clearly shows that the implicit solvent has substantially lowered the reaction energy for proton transfer. Lower energy indicates that proton transfer from methanol to catalyst is more favorable in implicit methanol than in vacuum. Lower energy also indicates possibility of proton transfer to catalyst first to be a favorable first step for the overall reaction. This will be followed by proton transfer to ester oxygen to form the products. Hence, these results indicate that PET depolymerization in methanolysis could take place through multiple discrete steps instead of a single concerted step.

We compare our results to those of the experimental PET methanolysis.[187] In addition to calculating proton transfer energies, charge on the protonated N atom of the tertiary amine catalyst was also determined. Both the experimental yield of DMT product obtained through PET depolymerization process in methanolysis using different tertiary amine catalysts and the calculated electronic charge on the N atom of the protonated tertiary amine catalysts in implicit methanol solvent of the catalyst are also given in Table 5.2.

First, we noticed that the proton energy transfer bears no correlation with the experimental DMT product yield that is reported in the literature.[187] Second, however, we found that the experimental DMT yield correlates to the charge on the N atom of the protonated tertiary amine. This correlation between the charge on the N atom of the tertiary amine and the experimental DMT yield is only seen for protonated catalyst in implicit methanol. We then calculated the charge on the N atom of the catalyst for the neutral catalysts in both vacuum and implicit methanol, and of the protonated catalysts in vacuum. In all these cases, we have seen no correlation between the charge on the N

atom of the catalyst to the experimental yield. Charges on N atom for all cases are reported in Section B.3.Table 5.2 does not include values for experimental DMT yield of linear TMA as it is not part of the experimental study.[187]

5.4.6 Discussion

Through our systematic investigation, we found that the charge on the N atom of the tertiary amine catalysts correlates directly to the product yield of the PET depolymerization product in experiments. Further, we found that the correlation only exists for protonated catalysts in implicit methanol solvent. In general, our computational investigation into the PET depolymerization reaction in methanolysis in the presence of tertiary amine catalysts reveals several important insights: 1.) the PET depolymerization into DMT and EG in methanolysis (Scheme 5.1) consists of several discrete steps rather than one concerted step, 2.) The tertiary amine catalyst is actively involved in the reaction, in which the proton transfer from methanol to ethyl benzoate occurs via the tertiary amine catalyst, and 3.) The proton transfer from methanol to the tertiary amine catalyst is the first step of the reaction, Finally, 4.) the charge on the N atom of the protonated tertiary amine directly corresponds to the experimental DMT product percentage yield.

The correlation between the charge on the N atom of the protonated tertiary amine and the experimental DMT yield can be explained by the Lewis basicity of the N atom in the tertiary amine. The more basic the N atom of the tertiary amine is, the more capable the tertiary amine molecule in extracting proton from methanol. As a result, more DMT yield can be produced in the PET depolymerization in methanol solvent. In this study, the basicity of the tertiary amine is reflected in the changes in the charge on the N atom from -1 to the result presented in Table 5.2 for each catalyst.

Seeing the direct correlation between the charge on the N atom of the protonated tertiary amine and the experimental DMT yield, we then propose that we can use the charge on the N atom of the protonated tertiary amine catalysts as a descriptor to initially screen tertiary amine catalysts. This allows to gauge the efficiency of the tertiary amine in catalyzing the PET depolymerization reaction in methanolysis. It will aid in initial screening further since it involves only a quick calculation of the charge and eliminates the need for bench experiments.

We note that this direct correlation is specific to the tertiary amine catalysts listed in this study, after investigating their role in catalyzing PET depolymerization in methanolysis. In the future, this conclusion could be further assessed by testing the accuracy of the descriptor, that is the charge on the N atom. It would need to be tested against a wider range of tertiary amine catalysts in which the experimental DMT yields are known. Further, using the charge on the atoms of the protonated catalysts to gauge and screen its efficiency in catalyzing PET depolymerization in methanol can be extended to other types of catalysts, such as of those acetate-based or carbonate-based metal catalysts.[170,181–184]

5.4.7 Conclusions

In this study, we have done a systematic computational investigation into PET depolymerization reaction in methanol solvent. We found that the PET depolymerization reaction in methanol into DMT and EG consists of several discrete reaction steps rather than a single concerted step. Furthermore, in the presence of tertiary amine catalysts, we have found that the proton transfer from the methanol to the tertiary amine catalyst is the first step in the PET depolymerization reaction in methanolysis. By comparing our results to that of experimental yield, we found that

the experimental yield directly correlates to the charge on the N atom of the protonated tertiary amine catalyst. We then propose that we can use the charge on the N atom of the protonated tertiary amine as a descriptor to quickly predict the suitability of other tertiary amine molecules as potential catalysts for PET depolymerization in methanolysis. To be able to find a descriptor that can be used to quickly screen the suitability of potential catalysts for PET depolymerization is of great interest as the efficiency of the potential catalysts can be quickly predicted without the need for experiments which may result in the generation of environmentally harmful waste.

5.4.8 Acknowledgments

This work is supported by NSF award EFRI-2132219. The work was facilitated using computational, storage, and networking infrastructure provided by the Hyak supercomputer system, supported in part by the University of Washington and the UW Student Technology Fee Proposal program (award 2015-028).

Chapter 6

Conclusions and Outlooks

The work presented here has advanced the ability to design plasmonic nanoparticle-based metamaterials, by providing a robust framework of electromagnetic simulation MPM and gradient-based inverse design method. This is used to design various 2D and 3D metamaterials with large number of NPs and highly dimensional parameter space with complex extinction spectra and electric field spatial profiles. We are also able to optimize experimentally measurable optical properties of reflectance and transmittance using this method.

The gradient-based inverse design method can be further developed to incorporate the ability to direct the assembly of the NPs. As mentioned initially, colloids ability to self-assemble into microstructures in a static or dynamic way can be controlled through several factors such as colloidal interactions, thermodynamic driving forces, kinetics, how NPs are synthesized. Colloidal interactions between NPs can be modeled through interaction potentials. Gradients with respect to potential parameters controlling these interactions can be computed and optimized for the optical properties. This would give insight into the assembly-structure relationship of plasmonic NPs. Bilayer and multilayer structures at various spacings have been optimized for pair-potential parameters using inverse design.[138] This can be combined with our electromagnetic simulation framework and used to design 2D and 3D metamaterials with structural control.

Stratified multilayer metasurfaces could be realized experimentally through techniques such as drop casting and sequential deposition. Drop casting is a simple low cost method, to prepare thin film layers. Monolayer films can be created by casting solution with NPs on a substrate followed by the solvents evaporation, to form a layer with certain thickness. This process can be automated and easy to adapt without much equipment. Our experimental collaborators through PREM consortium at University of Hawaii, Manoa and University of Washington are developing automated workflows to create, characterize and evaluate monolayer thin-films through drop-casting. Choices between various drop casting methods, and parameters such as NPs in the solution, solvent, substrate can be explored and the process can be automated through lab automation equipment such as Opentrons OT-2 for pipetting droplets.[207] Another thin-film processing method is dip coating, where the substrate is immersed in the coating solution. Efforts to automate dip-coating to create layers of thin-film with uniform thickness are ongoing. Both these methods could be used to synthesize thin-films of plasmonic NPs that we could corroborate or simultaneously model through our gradient-based method to learn about the structure-function properties of the monolayers. Using computational tools to study this monolayers could provide information on parameters that are difficult to characterize experimentally.

Thin-films created experimentally through techniques such atomic layer deposition (ALD) can often be of non-uniform thickness. Ellipsometry through direct measurements of phase difference (ψ) and amplitude ratios (Δ) is used to calculate the thickness and effective refractive index of these films. Ellipsometry measures change in the polarization of light upon reflection from or transmission through a sample. ψ and Δ represent the raw measurement from an ellipsometer.

They describe the change in polarization that occurs when the measurement beam interacts with a sample surface. Accuracy of the thickness values is entirely dependent on the models used to process ψ and Δ. We can use our stratified medium calculations shown in Chapter 4 to calculate reflectance, transmittance coefficients of thin films by modeling them as slabs. These coefficients can then be used to calculate ψ and Δ. Target ψ and Δ from stratified medium calculations can then be used to inverse design experimental measurements. This can be used to determine concentration of thin-films. An example where this can be applied is vapor phase synthesis of ZIF-8 thin-film from ZnO.

Stratified medium calculations combined with MPM and adjoint method is shown to optimize for experimentally measurable property of reflectance at normal incidence angle. By working through gradient propagation for non-normal incidence angle and demonstrating it in the future, we will be able to design NP based metamaterials agnostic to incidence angle. Having control over incidence angle will help design materials that have optical properties that are currently highly sensitive to change in incidence angle.[66]

In addition to electric field for electromagnetic simulations, magnetic fields can be applied externally to colloidal nanoparticles. They are known to orient particles to control their optical properties. These particles could include particles such as dielectrics without any distinct optical properties or plasmonic NPs. Plasmonic NPs that can be tuned by external magnetic field are termed as paramagnetic NPs. We can explore plasmonic response of these materials through magnetic field directed self-assembly through our framework. Magnetic control is shown to tune optical properties such as structural color.[149] Brownian dynamics simulation with mutual dipole interactions can be used to assemble paramagnetic nanoparticles with varying field strength and and particle volume fraction. We can then characterize their optical response through our electromagnetic simulator. This can be done to see how optical response such as extinction spectrum can evolve as NPs self-assemble in magnetic field. Orientation of light parallel or perpendicular to the magnetic field will lead to change in extinction response. We could characterize, ensemble resonance frequencies with varying magnetic field strength and electric field polarizations. This can be applied to structures with varying volume fractions.

We hope the methods and implications outlined in these chapters will inspire future development of inverse design frameworks and design of unique colloidal materials.

Appendix A

Supplementary Information : Chapter 3. Inverse Design of Optical Metamaterials Assembled from Plasmonic Nanoparticles

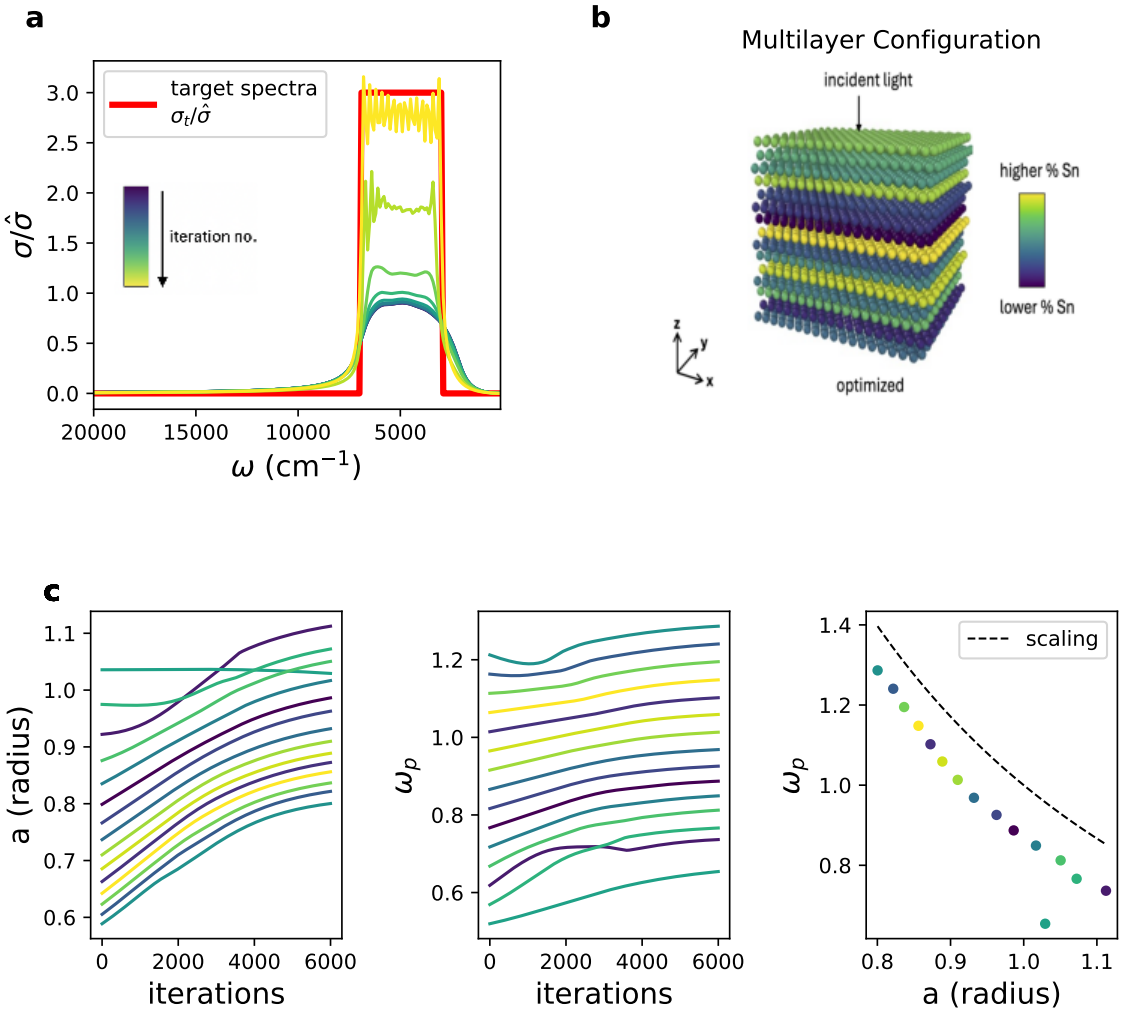

Figure A.1: Inverse design of a stratified plasmonic metasturface. Optimizer updates the radius a, plasma frequency ω_p, damping coefficient γ and high-frequency-permittivity ε_∞ of each layer. Layers are randomized and not initialized in decreasing order of radius from top to bottom layer **A:** Evolution of the extinction cross-section σ of the metasurface as a function of incident frequency ω over optimization iterations (colors) The target spectrum is in red. **B:** Snapshot of the final metasurface configuration, with each nanoparticle colored by its ω_p. **C:** a and ω_p for each layer (colors) as a function of optimization iteration and the final set of $(a, omega_p)$ plotted together. Dashed line indicates $a \sim \omega_p^{-2/3}$ scaling. Quantities are nondimensionalized by $\omega_p^* = \sqrt{\varepsilon_0/\varepsilon_f}\omega_p$ and $\hat{\sigma} = \sqrt{\varepsilon_f \mu_f}\omega_p^*$.

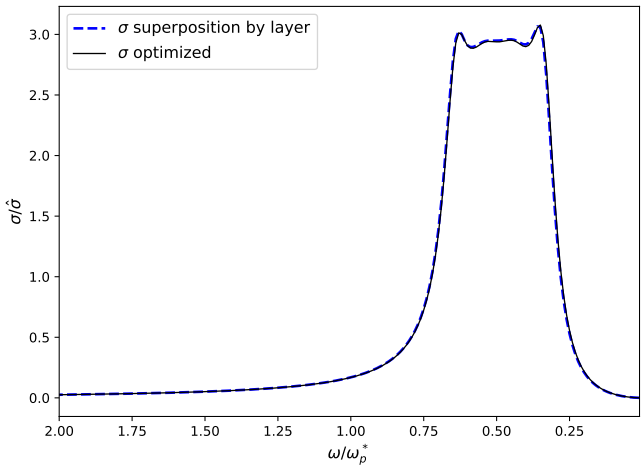

Figure A.2: Optimized extinction cross-section σ of the metasurface ensemble in Figure 3.2 (black) and linear superposition of the isolated layers σ (dashed blue lines)

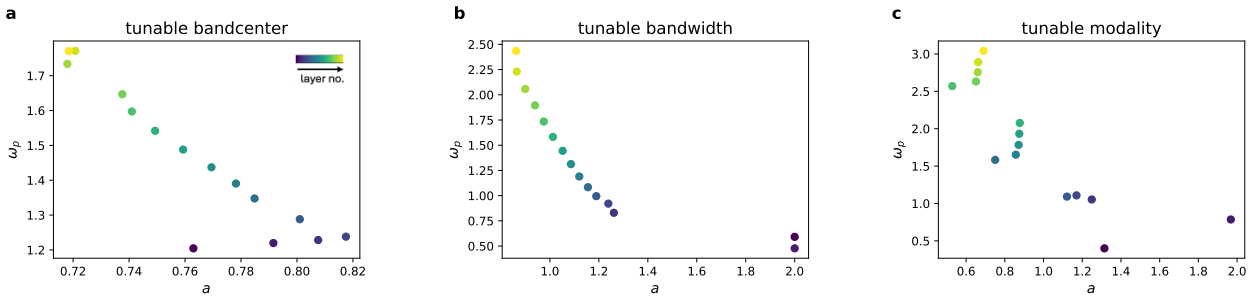

Figure A.3: Final set of optimized a and ω_p for each layer plotted together for stratified plasmonic metasurfaces tuned in Figure 3.3 for the target spectra of **A:** bandcenter $\Omega = 0.8\hat{\omega}$ and bandwidth $W = 0.4\hat{\omega}$; **B:** bandcenter $\Omega = 0.8\hat{\omega}$ and bandwidth $W = 1.2\hat{\omega}$; **C:** three stopbands of bandwidth $W = 0.3\hat{\omega}$ and bandcenters $\Omega = 0.35, 0.95, 1.55\hat{\omega}$.

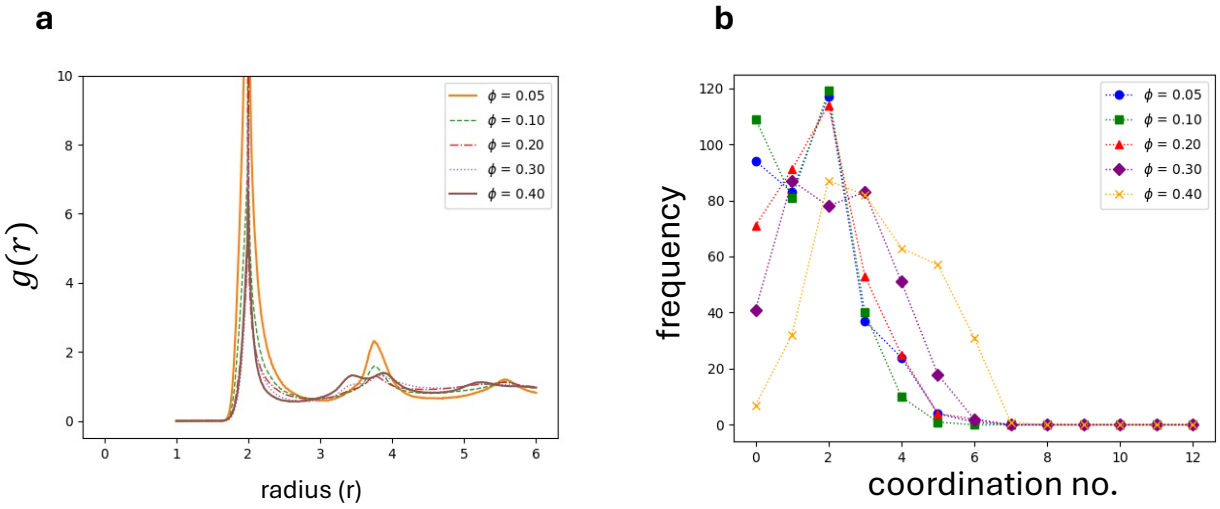

Figure A.4: Structural analysis of metamaterial structures across a range volume fractions ϕ in Figure 3.5 through **A:** Radial Distribution Function (RDF); **B:** Coordination number

Appendix B

Supplementary Information : Chapter 5. Reaction Pathway Analysis of PET Deconstruction via Methanolysis and Tertiary Amine Catalysts

B.1 Relative energy (E_0) of transition state for transesterification reaction between ethylbenzoate and methanol uncatalyzed and in presence of catalysts using M06-2x[189] functional and the 6-31G (d, p) basis set. Imaginary frequency for verifying transition state structures calculated using frequency analysis is also included for these reactions.

Catalysts	Catalyst Configuration	E_0 (kcal/mol)		Transition state structure imaginary frequency (cm^{-1})	
		in vacuum	in implicit methanol	in vacuum	in implicit methanol
NMP	cyclic	34.5	36.8	−1236.0	−1309.6
Linear TMA	linear	34.3	37.7	−1214.9	−1284.3
TEA	linear	34.1	36.8	−1189.7	−1234.4
Aromatic TMA	aromatic	33.3	36.6	−1238.7	−1315.8
DMA	aromatic	32.7	36.7	−1235.6	−1316.7
TEEDA	diamine	30.7	34.1	−1187.4	−1258.3
no catalyst	–	41.0	42.9	−1185.3	−1250.9

B.2 Yield equations for DMT yield %, EG yield % and total yield or DMT + EG yield % for depolymerization of 0.1g PET bottle strips in 20 ml of 0.20 M tertiary amine methanol solution at $160C$*, 1 hour reaction duration at 700 rpm*

$$\text{DMT yield\%} = \frac{n_1}{n_0} \times 100 \tag{B.1}$$

$$\text{EG yield\%} = \frac{n_2}{n_0} \times 100 \tag{B.2}$$

$$\text{Total yield\%} = \frac{n_1 + n_2}{n_0} \times 100 \tag{B.3}$$

$$\tag{B.4}$$

n_0 is the moles of the repeat unit of fresh PET reactants before reaction.
n_1 is the moles of dimethyl terephthalate after the reaction.
n_2 is the moles of ethylene glycol after the reaction

B.3 Charge on N atom in the neutral and protonated tertiary amine catalysts as calculated by CHELPG using the M06-2x[189] functional and the 6-311++G (d, p)[198,199] basis set

Catalysts	Catalyst Configuration	Charge on N atom in neutral catalyst		Transition state structure imaginary frequency (cm^{-1})	
		in vacuum	in implicit methanol	in vacuum	in implicit methanol
NMP	cyclic	−0.54	−0.61	0.12	0.19
Linear TMA	linear	−0.36	−0.42	−0.01	0.13
TEA	linear	−0.67	−0.76	0.17	0.16
Aromatic TMA	aromatic	−0.44	−0.50	−0.40	−0.28
DMA	aromatic	−0.50	−0.51	−0.32	−0.30
TEEDA	diamine	−0.55	−0.60	−0.19	−0.14

B.4 Example gaussian input files for finding transition state, intrinsic reaction coordinate scan and geometry optimization. Reaction is ethyl benzoate, methanol and NMP catalyst in implicit methanol solvent

Input file for transition state calculation

```
%chk=TS.chk
%nprocshared=10
# opt(TS,CalcFC,noeigen) freq 6-31g(d,p) nosymm m062x geom=connectivity
scrf(solvent=methanol)

Title Card Required

0 1
C          -0.51248800   1.77844300   0.02802400
O          -2.02330900   1.50000400   0.42877900
C          -2.96021300   1.60637300  -0.65762200
H          -3.94161100   1.70801800  -0.19123600
H          -2.73309900   2.50779200  -1.23015200
O          -0.34254500   2.40494700  -0.99577000
C          -0.00948200   2.55148500   2.61567600
H           1.06296400   2.40808300   2.44206600
H          -0.40562700   1.64942000   3.09826000
H          -0.14729600   3.40306700   3.28697600
O          -0.65979100   2.83608500   1.38968100
H          -1.81914500   2.30647500   1.15428400
C           0.30953400   0.59612800   0.44023800
C          -0.17567200  -0.42600600   1.25951700
C           1.60866900   0.52990400  -0.06621800
C           0.63935600  -1.51372000   1.56037900
H          -1.19068100  -0.37818300   1.63792000
C           2.41979100  -0.55864100   0.23743900
H           1.96106900   1.32661600  -0.71330200
C           1.93490800  -1.58173100   1.04995400
H           0.25958900  -2.31294700   2.18823900
H           3.42448900  -0.61343500  -0.16804500
H           2.56429600  -2.43493400   1.28174500
C          -0.49073900  -3.52004200  -4.07485600
C          -0.94088800  -2.64306900  -2.90302200
C           0.27922300  -2.04189800  -2.19275500
C           1.59119100  -2.12246800  -4.20860100
C           0.42830700  -2.72600700  -5.00743800
H          -0.02733700  -1.37996900  -1.37535200
H          -1.59059900  -1.84015500  -3.27540100
H          -1.53372100  -3.22170400  -2.18610600
H           0.06238500  -4.38446600  -3.68116800
H          -1.35329800  -3.91486500  -4.62124900
H           2.23795300  -1.52124100  -4.85709700
```

H	2.20289100	-2.94381800	-3.80881700
H	-0.14388500	-1.92630500	-5.49456800
H	0.82261900	-3.36552400	-5.80435900
H	0.86321000	-2.85807200	-1.74313400
N	1.17450400	-1.29384100	-3.07672800
C	0.61513900	-0.01441900	-3.48735100
H	0.40827100	0.59452100	-2.60042500
H	1.34984100	0.51816500	-4.10005700
H	-0.31662700	-0.08404600	-4.07385300
C	-2.86369500	0.36220200	-1.51803800
H	-3.04224100	-0.53584700	-0.92143400
H	-3.60447300	0.40443600	-2.32023800
H	-1.87036300	0.29278000	-1.97043800

1 6 2.0 13 1.0
2 3 1.0
3 4 1.0 5 1.0 44 1.0
4
5
6
7 8 1.0 9 1.0 10 1.0 11 1.0
8
9
10
11
12
13 14 1.5 15 1.5
14 16 1.5 17 1.0
15 18 1.5 19 1.0
16 20 1.5 21 1.0
17
18 20 1.5 22 1.0
19
20 23 1.0
21
22
23
24 25 1.0 28 1.0 32 1.0 33 1.0
25 26 1.0 30 1.0 31 1.0
26 29 1.0 38 1.0 39 1.0
27 28 1.0 34 1.0 35 1.0 39 1.0
28 36 1.0 37 1.0
29
30
31
32
33

```
 34
 35
 36
 37
 38
 39 40 1.0
 40 41 1.0 42 1.0 43 1.0
 41
 42
 43
 44 45 1.0 46 1.0 47 1.0
 45
 46
 47

1 12 F
1 11 F
12 2 F
12 11 F
```

Input file for intrinsic reaction coordinate calculation in forward direction followed by geometry optimization

```
%chk=TS.chk
%nprocshared=10
# IRC(Forward,RCFC) 6-31g(d,p) nosymm m062x geom=allcheck guess=read
scrf(solvent=methanol)

--Link1--
%chk=TS.chk
%nprocshared=10
# opt 6-31g(d,p) freq nosymm m062x geom=allcheck guess=read scrf(solvent=methanol)
```

Input file for intrinsic reaction coordinate calculation in reverse direction followed by geometry optimization

```
%chk=TS.chk
%nprocshared=10
# IRC(Reverse,RCFC) 6-31g(d,p) nosymm m062x geom=allcheck guess=read
scrf(solvent=methanol)

--Link1--
%chk=TS.chk
%nprocshared=10
# opt 6-31g(d,p) freq nosymm m062x geom=allcheck guess=read scrf(solvent=methanol)
```

BIBLIOGRAPHY

[1] Everett, D. H. Manual of Symbols and Terminology for Physicochemical Quantities and Units, Appendix II: Definitions, Terminology and Symbols in Colloid and Surface Chemistry. *Pure and Applied Chemistry* **1972**, *31*, 577–638.

[2] Lekkerkerker, H. N. W. *Colloids and the Depletion Interaction*; Lecture Notes in Physics Ser v.833; Springer Netherlands: Dordrecht, 2011.

[3] Kolluru, L.; Atre, P.; Rizvi, S. Characterization and Applications of Colloidal Systems as Versatile Drug Delivery Carriers for Parenteral Formulations. *Pharmaceuticals* **2021**, *14*, 108.

[4] Wasan, D.; Nikolov, A.; Moudgil, B. Colloidal dispersions: Structure, stability and geometric confinement. *Powder Technology* **2005**, *153*, 135–141.

[5] Moradpour, N.; Yang, J.; Tsai, P. A. Liquid foam: Fundamentals, rheology, and applications of foam displacement in porous structures. *Current Opinion in Colloid & Interface Science* **2024**, *74*, 101845.

[6] Xu, L.; Zhou, Y.; Amin, S. In *Soft Matter Series*; Priestley, R., Prud'homme, R., Eds.; Royal Society of Chemistry: Cambridge, 2019; pp 399–417.

[7] *Coulson and Richardson's Chemical Engineering*; Elsevier, 2019; pp 693–737.

[8] Whitesides, G. M.; Grzybowski, B. Self-Assembly at All Scales. *Science* **2002**, *295*, 2418–2421.

[9] Agrawal, A.; Cho, S. H.; Zandi, O.; Ghosh, S.; Johns, R. W.; Milliron, D. J. Localized Surface Plasmon Resonance in Semiconductor Nanocrystals. *Chemical Reviews* **2018**, *118*, 3121–3207.

[10] Hu, M.; Chen, J.; Li, Z.-Y.; Au, L.; Hartland, G. V.; Li, X.; Marquez, M.; Xia, Y. Gold nanostructures: engineering their plasmonic properties for biomedical applications. *Chemical Society Reviews* **2006**, *35*, 1084.

[11] Maier, S. A. *Plasmonics: fundamentals and applications*, repr. ed.; Springer: New York, NY, 2007.

[12] Giannini, V.; Fernández-Domínguez, A. I.; Heck, S. C.; Maier, S. A. Plasmonic Nanoantennas: Fundamentals and Their Use in Controlling the Radiative Properties of Nanoemitters. *Chemical Reviews* **2011**, *111*, 3888–3912.

[13] LaMer, V. K.; Dinegar, R. H. Theory, Production and Mechanism of Formation of Monodispersed Hydrosols. *Journal of the American Chemical Society* **1950**, *72*, 4847–4854.

[14] Lu, X.; Rycenga, M.; Skrabalak, S. E.; Wiley, B.; Xia, Y. Chemical Synthesis of Novel Plasmonic Nanoparticles. *Annual Review of Physical Chemistry* **2009**, *60*, 167–192.

[15] Van Embden, J.; Chesman, A. S. R.; Jasieniak, J. J. The Heat-Up Synthesis of Colloidal Nanocrystals. *Chemistry of Materials* **2015**, *27*, 2246–2285.

[16] Kwon, S. G.; Hyeon, T. Formation Mechanisms of Uniform Nanocrystals via Hot-Injection and Heat-Up Methods. *Small* **2011**, *7*, 2685–2702.

[17] Hamza, M. K.; Bluet, J.-M.; Masenelli-Varlot, K.; Canut, B.; Boisron, O.; Melinon, P.; Masenelli, B. Tunable mid IR plasmon in GZO nanocrystals. *Nanoscale* **2015**, *7*, 12030–12037.

[18] Kim, K.; Sherman, Z. M.; Cleri, A.; Chang, W. J.; Maria, J.-P.; Truskett, T. M.; Milliron, D. J. Hierarchically Doped Plasmonic Nanocrystal Metamaterials. *Nano Letters* **2023**, *23*, 7633–7641.

[19] Takatori, K.; Okamoto, T.; Ishibashi, K. Surface-plasmon-induced ultra-broadband light absorber operating in the visible to infrared range. *Optics Express* **2018**, *26*, 1342.

[20] Gong, J.; Dai, R.; Wang, Z.; Zhang, Z. Thickness Dispersion of Surface Plasmon of Ag Nanothin Films: Determination by Ellipsometry Iterated with Transmittance Method. *Scientific Reports* **2015**, *5*, 9279.

[21] Shen, G.; Guyot-Sionnest, P. HgS and HgS/CdS Colloidal Quantum Dots with Infrared Intraband Transitions and Emergence of a Surface Plasmon. *The Journal of Physical Chemistry C* **2016**, *120*, 11744–11753.

[22] Stetefeld, J.; McKenna, S. A.; Patel, T. R. Dynamic light scattering: a practical guide and applications in biomedical sciences. *Biophysical Reviews* **2016**, *8*, 409–427.

[23] Filippov, S. K.; Khusnutdinov, R.; Murmiliuk, A.; Inam, W.; Zakharova, L. Y.; Zhang, H.; Khutoryanskiy, V. V. Dynamic light scattering and transmission electron microscopy in drug delivery: a roadmap for correct characterization of nanoparticles and interpretation of results. *Materials Horizons* **2023**, *10*, 5354–5370.

[24] Nekvapil, F.; Farcău, C. The role of focused laser plasmonics in shaping SERS spectra of molecules on nanostructured surfaces. *Nanoscale Advances* **2025**, *7*, 3008–3017.

[25] Kuznetsov, A. I. et al. Roadmap for Optical Metasurfaces. *ACS Photonics* **2024**, *11*, 816–865.

[26] Pan, Z.; Pan, X. Deep Learning and Adjoint Method Accelerated Inverse Design in Photonics: A Review. *Photonics* **2023**, *10*, 852.

[27] Gallinet, B.; Butet, J.; Martin, O. J. F. Numerical methods for nanophotonics: standard problems and future challenges. *Laser & Photonics Reviews* **2015**, *9*, 577–603.

[28] Fu, P.-H.; Lo, S.-C.; Tsai, P.-C.; Lee, K.-L.; Wei, P.-K. Optimization for Gold Nanostructure-Based Surface Plasmon Biosensors Using a Microgenetic Algorithm. *ACS Photonics* **2018**, *5*, 2320–2327.

[29] Solis, D. M.; Obelleiro, F.; Taboada, J. M. Surface Integral Equation-Domain Decomposition Scheme for Solving Multiscale Nanoparticle Assemblies With Repetitions. *IEEE Photonics Journal* **2016**, *8*, 1–14.

[30] Yu, D.-M.; Liu, Y.-N.; Tian, F.-L.; Pan, X.-M.; Sheng, X.-Q. Accurate thermoplasmonic simulation of metallic nanoparticles. *Journal of Quantitative Spectroscopy and Radiative Transfer* **2017**, *187*, 150–160.

[31] Sherman, Z. M.; Milliron, D. J.; Truskett, T. M. Distribution of Single-Particle Resonances Determines the Plasmonic Response of Disordered Nanoparticle Ensembles. *ACS Nano* **2024**, *18*, 21347–21363.

[32] Dey, D.; Schatz, G. C. Plasmonic surface lattice resonances in nanoparticle arrays. *MRS Bulletin* **2024**, *49*, 421–430.

[33] Herkert, E.; Sterl, F.; Both, S.; Tikhodeev, S. G.; Weiss, T.; Giessen, H. Influence of structural disorder on plasmonic metasurfaces and their colors—a coupled point dipole approach: tutorial. *Journal of the Optical Society of America B* **2023**, *40*, B59.

[34] Markel, V. A. Extinction, scattering and absorption of electromagnetic waves in the coupled-dipole approximation. *Journal of Quantitative Spectroscopy and Radiative Transfer* **2019**, *236*, 106611.

[35] Theobald, D.; Beutel, D.; Borgmann, L.; Mescher, H.; Gomard, G.; Rockstuhl, C.; Lemmer, U. Simulation of light scattering in large, disordered nanostructures using a periodic T-matrix method. **2021**,

[36] Mishchenko, M. I.; Travis, L. D.; Mackowski, D. W. T-matrix computations of light scattering by nonspherical particles: A review. *Journal of Quantitative Spectroscopy and Radiative Transfer* **1996**, *55*, 535–575.

[37] Aizpurua, J.; Hanarp, P.; Sutherland, D. S.; Käll, M.; Bryant, G. W.; García De Abajo, F. J. Optical Properties of Gold Nanorings. *Physical Review Letters* **2003**, *90*, 057401.

[38] Sherman, Z. M.; Kim, K.; Kang, J.; Roman, B. J.; Crory, H. S. N.; Conrad, D. L.; Valenzuela, S. A.; Lin, E.; Dominguez, M. N.; Gibbs, S. L.; Anslyn, E. V.; Milliron, D. J.; Truskett, T. M. Plasmonic Response of Complex Nanoparticle Assemblies. *Nano Lett.* **2023**, *23*, 3030–3037.

[39] Back, T.; Hammel, U.; Schwefel, H.-P. Evolutionary computation: comments on the history and current state. *IEEE Transactions on Evolutionary Computation* **1997**, *1*, 3–17.

[40] Chen, W.; Zhang, B.; Wang, P.; Dai, S.; Liang, W.; Li, H.; Fu, Q.; Li, J.; Li, Y.; Dai, T.; Yu, H.; Yang, J. Ultra-compact and low-loss silicon polarization beam splitter using a particle-swarm-optimized counter-tapered coupler. *Optics Express* **2020**, *28*, 30701.

[41] Peurifoy, J.; Shen, Y.; Jing, L.; Yang, Y.; Cano-Renteria, F.; DeLacy, B. G.; Joannopoulos, J. D.; Tegmark, M.; Soljačić, M. Nanophotonic particle simulation and inverse design using artificial neural networks. *Science Advances* **2018**, *4*, eaar4206.

[42] Wu, Y.; Walsh, A.; Ganose, A. M. Race to the bottom: Bayesian optimisation for chemical problems. *Digital Discovery* **2024**, *3*, 1086–1100.

[43] Li, M.; McCourt, M. J.; Galante, A. J.; Leu, P. W. Bayesian optimization of nanophotonic electromagnetic shielding with very high visible transparency. *Optics Express* **2022**, *30*, 33182.

[44] Molesky, S.; Lin, Z.; Piggott, A. Y.; Jin, W.; Vucković, J.; Rodriguez, A. W. Inverse design in nanophotonics. *Nature Photonics* **2018**, *12*, 659–670.

[45] Fu, M.; Glover, F.; April, J. Simulation Optimization: A Review, New Developments, and Applications. Proceedings of the Winter Simulation Conference, 2005. Orlando, FL. USA, 2005; pp 83–95.

[46] Piggott, A. Y.; Lu, J.; Lagoudakis, K. G.; Petykiewicz, J.; Babinec, T. M.; Vučković, J. Inverse design and demonstration of a compact and broadband on-chip wavelength demultiplexer. *Nature Photonics* **2015**, *9*, 374–377.

[47] Borel, P. I.; Harpøth, A.; Frandsen, L. H.; Kristensen, M.; Shi, P.; Jensen, J. S.; Sigmund, O. Topology optimization and fabrication of photonic crystal structures. *Optics Express* **2004**, *12*, 1996.

[48] Giles, M. B.; Pierce, N. A. An Introduction to the Adjoint Approach to Design. *Flow, Turbulence and Combustion* **2000**, *65*, 393–415.

[49] Mengu, D.; Sakib Rahman, M. S.; Luo, Y.; Li, J.; Kulce, O.; Ozcan, A. At the intersection of optics and deep learning: statistical inference, computing, and inverse design. *Advances in Optics and Photonics* **2022**, *14*, 209.

[50] Hornik, K.; Stinchcombe, M.; White, H. Multilayer feedforward networks are universal approximators. *Neural Networks* **1989**, *2*, 359–366.

[51] Jiang, J.; Fan, J. A. Global Optimization of Dielectric Metasurfaces Using a Physics-Driven Neural Network. *Nano Letters* **2019**, *19*, 5366–5372.

[52] Qu, Y.; Jing, L.; Shen, Y.; Qiu, M.; Soljačić, M. Migrating Knowledge between Physical Scenarios Based on Artificial Neural Networks. *ACS Photonics* **2019**, *6*, 1168–1174.

[53] Schulz, S. A. et al. Roadmap on photonic metasurfaces. *Applied Physics Letters* **2024**, *124*, 260701.

[54] Zheludev, N. I.; Kivshar, Y. S. From metamaterials to metadevices. *Nature Materials* **2012**, *11*, 917–924.

[55] Kildishev, A. V.; Boltasseva, A.; Shalaev, V. M. Planar Photonics with Metasurfaces. *Science* **2013**, *339*, 1232009.

[56] Yu, N.; Capasso, F. Flat optics with designer metasurfaces. *Nature Materials* **2014**, *13*, 139–150.

[57] Glybovski, S. B.; Tretyakov, S. A.; Belov, P. A.; Kivshar, Y. S.; Simovski, C. R. Metasurfaces: From microwaves to visible. *Physics Reports* **2016**, *634*, 1–72.

[58] Genevet, P.; Capasso, F.; Aieta, F.; Khorasaninejad, M.; Devlin, R. Recent advances in planar optics: from plasmonic to dielectric metasurfaces. *Optica* **2017**, *4*, 139–152.

[59] Kang, C.; Park, C.; Lee, M.; Kang, J.; Jang, M. S.; Chung, H. Large-scale photonic inverse design: computational challenges and breakthroughs. *Nanophotonics* **2024**, *13*, 3765–3792.

[60] Yang, Z.; Li, X.; Catherine Brinson, L.; Choudhary, A. N.; Chen, W.; Agrawal, A. Microstructural Materials Design Via Deep Adversarial Learning Methodology. *Journal of Mechanical Design* **2018**, *140*.

[61] Sarkar, S.; Ji, A.; Jermain, Z.; Lipton, R.; Brongersma, M.; Dayal, K.; Noh, H. Y. Physics-Informed Machine Learning for Inverse Design of Optical Metamaterials. *Advanced Photonics Research* **2023**, *4*.

[62] Chen, Y.; Zhu, J.; Xie, Y.; Feng, N.; Liu, Q. H. Smart inverse design of graphene-based photonic metamaterials by an adaptive artificial neural network. *Nanoscale* **2019**, *11*, 9749–9755.

[63] Rodríguez, J. A.; Abdalla, A. I.; Wang, B.; Lou, B.; Fan, S.; Cappelli, M. A. Inverse Design of Plasma Metamaterial Devices for Optical Computing. *Physical Review Applied* **2021**, *16*.

[64] Bendsøe, M. P.; Sigmund, O. *Topology Optimization*; Springer Berlin Heidelberg, 2004.

[65] Su, L.; Piggott, A. Y.; Sapra, N. V.; Petykiewicz, J.; Vučković, J. Inverse Design and Demonstration of a Compact on-Chip Narrowband Three-Channel Wavelength Demultiplexer. *ACS Photonics* **2018**, *5*, 301–305.

[66] Xiao, T. P.; Cifci, O. S.; Bhargava, S.; Chen, H.; Gissibl, T.; Zhou, W.; Giessen, H.; Toussaint, K. C.; Yablonovitch, E.; Braun, P. V. Diffractive Spectral-Splitting Optical Element Designed by Adjoint-Based Electromagnetic Optimization and Fabricated by Femtosecond 3D Direct Laser Writing. *ACS Photonics* **2016**, *3*, 886–894.

[67] Lee, W.-K.; Yu, S.; Engel, C. J.; Reese, T.; Rhee, D.; Chen, W.; Odom, T. W. Concurrent design of quasi-random photonic nanostructures. *Proceedings of the National Academy of Sciences* **2017**, *114*, 8734–8739.

[68] Hughes, T. W.; Minkov, M.; Williamson, I. A. D.; Fan, S. Adjoint Method and Inverse Design for Nonlinear Nanophotonic Devices. *ACS Photonics* **2018**, *5*, 4781–4787.

[69] Sin Tan, Y.; Wang, H.; Wang, H.; Pan, C.; Yang, J. K. W. High-throughput fabrication of large-scale metasurfaces using electron-beam lithography with SU-8 gratings for multilevel security printing. *Photonics Research* **2023**, *11*, B103.

[70] Mak, J. C. C.; Sideris, C.; Jeong, J.; Hajimiri, A.; Poon, J. K. S. Binary particle swarm optimized 2 $\times$ 2 power splitters in a standard foundry silicon photonic platform. *Optics Letters* **2016**, *41*, 3868–3871.

[71] Shen, B.; Wang, P.; Polson, R.; Menon, R. An integrated-nanophotonics polarization beamsplitter with 2.4 $\times$ 2.4 μm2 footprint. *Nature Photonics* **2015**, *9*, 378–382.

[72] Piggott, A. Y.; Petykiewicz, J.; Su, L.; Vučković, J. Fabrication-constrained nanophotonic inverse design. *Scientific Reports* **2017**, *7*, 1786.

[73] Sherman, Z. M.; Kang, J.; Milliron, D. J.; Truskett, T. M. Illuminating Disorder: Optical Properties of Complex Plasmonic Assemblies. *The Journal of Physical Chemistry Letters* **2024**, *15*, 6424–6434.

[74] Solís, D. M.; Taboada, J. M.; Obelleiro, F.; Liz-Marzán, L. M.; García De Abajo, F. J. Optimization of Nanoparticle-Based SERS Substrates through Large-Scale Realistic Simulations. *ACS Photonics* **2017**, *4*, 329–337.

[75] Mueller, N. S.; Pfitzner, E.; Okamura, Y.; Gordeev, G.; Kusch, P.; Lange, H.; Heberle, J.; Schulz, F.; Reich, S. Surface-Enhanced Raman Scattering and Surface-Enhanced Infrared Absorption by Plasmon Polaritons in Three-Dimensional Nanoparticle Supercrystals. *ACS Nano* **2021**, *15*, 5523–5533.

[76] Atwater, H. A.; Polman, A. Plasmonics for improved photovoltaic devices. *Nature Materials* **2010**, *9*, 205–213.

[77] L. Runnerstrom, E.; Llordés, A.; D. Lounis, S.; J. Milliron, D. Nanostructured electrochromic smart windows: traditional materials and NIR-selective plasmonic nanocrystals. *Chemical Communications* **2014**, *50*, 10555–10572.

[78] Kim, J.; Ong, G. K.; Wang, Y.; LeBlanc, G.; Williams, T. E.; Mattox, T. M.; Helms, B. A.; Milliron, D. J. Nanocomposite Architecture for Rapid, Spectrally-Selective Electrochromic Modulation of Solar Transmittance. *Nano Letters* **2015**, *15*, 5574–5579.

[79] Llordés, A.; Wang, Y.; Fernandez-Martinez, A.; Xiao, P.; Lee, T.; Poulain, A.; Zandi, O.; Saez Cabezas, C. A.; Henkelman, G.; Milliron, D. J. Linear topology in amorphous metal oxide electrochromic networks obtained via low-temperature solution processing. *Nature Materials* **2016**, *15*, 1267–1273.

[80] Cui, J.; Li, Y.; Liu, L.; Chen, L.; Xu, J.; Ma, J.; Fang, G.; Zhu, E.; Wu, H.; Zhao, L.; Wang, L.; Huang, Y. Near-Infrared Plasmonic-Enhanced Solar Energy Harvest for Highly Efficient Photocatalytic Reactions. *Nano Letters* **2015**, *15*, 6295–6301.

[81] Baffou, G.; Quidant, R.; García de Abajo, F. J. Nanoscale Control of Optical Heating in Complex Plasmonic Systems. *ACS Nano* **2010**, *4*, 709–716.

[82] Davies, D. W.; Roman, B. J.; Milliron, D. J. Tuning emittance in films of plasmonic metal oxide nanocrystals for daytime radiative cooling. *Solar Energy Materials and Solar Cells* **2024**, *277*, 113094.

[83] Ling, L.; Zhu, R.; Gu, Y.; Chen, Z. Doped semiconductor nanoparticles for possible daytime radiative cooling applications. *Semiconductor Science and Technology* **2020**, *35*, 075018.

[84] Chang, W. J.; Roman, B. J.; Paul, T.; Sakotic, Z.; Vora, P.; Kim, K.; Hurst, L. E.; Wasserman, D.; Truskett, T. M.; Milliron, D. J. Ultrastrong Coupling by Assembling Plasmonic Metal Oxide Nanocrystals in Open Cavities. *ACS Nano* **2025**, *19*, 12332–12344.

[85] Chang, W. J.; Sakotic, Z.; Ware, A.; Green, A. M.; Roman, B. J.; Kim, K.; Truskett, T. M.; Wasserman, D.; Milliron, D. J. Wavelength Tunable Infrared Perfect Absorption in Plasmonic Nanocrystal Monolayers. *ACS Nano* **2024**, *18*, 972–982.

[86] Huh, J.-H.; Lee, J.; Lee, S. Soft Plasmonic Assemblies Exhibiting Unnaturally High Refractive Index. *Nano Letters* **2020**, *20*, 4768–4774.

[87] Singh, M.; Sherman, Z. M.; Milliron, D. J.; Truskett, T. M. Linker-Templated Structure Tuning of Optical Response in Plasmonic Nanoparticle Gels. *The Journal of Physical Chemistry C* **2022**, *126*, 16885–16893.

[88] Yadav, P. R.; Rizvi, M. H.; Kuttich, B.; Mishra, S. R.; Chapman, B. S.; Lynch, B. B.; Kraus, T.; Oldenburg, A. L.; Tracy, J. B. Plasmon-Coupled Gold Nanoparticles in Stretched Shape-Memory Polymers for Mechanical/Thermal Sensing. *ACS Applied Nano Materials* **2021**, *4*, 3911–3921.

[89] Fan, Z.; Govorov, A. O. Plasmonic Circular Dichroism of Chiral Metal Nanoparticle Assemblies. *Nano Letters* **2010**, *10*, 2580–2587.

[90] Yoon, J.; Jang, H.-J.; Jung, I.; Park, S. A close-packed 3D plasmonic superlattice of truncated octahedral gold nanoframes. *Nanoscale* **2017**, *9*, 7708–7713.

[91] Kim, J.; Zhao, Q.; Choi, I.; Oh, M. J.; Kwon, S.; Park, S. Ensemble hot-spots in 3D supercrystals of plasmonic octahedral nanoparticles in tip-to-tip configured superlattices. *Nature Communications* **2025**, *16*.

[92] Matricardi, C.; Hanske, C.; Garcia-Pomar, J. L.; Langer, J.; Mihi, A.; Liz-Marzán, L. M. Gold

Nanoparticle Plasmonic Superlattices as Surface-Enhanced Raman Spectroscopy Substrates. *ACS Nano* **2018**, *12*, 8531–8539.

[93] Chang, W. J.; Roman, B. J.; Green, A. M.; Truskett, T. M.; Milliron, D. J. Surface-Enhanced Infrared Absorption Spectroscopy by Resonant Vibrational Coupling with Plasmonic Metal Oxide Nanocrystals. *ACS Nano* **2024**, *18*, 20636–20647.

[94] Sherman, Z. M.; Green, A. M.; Howard, M. P.; Anslyn, E. V.; Truskett, T. M.; Milliron, D. J. Colloidal Nanocrystal Gels from Thermodynamic Principles. *Accounts of Chemical Research* **2021**, *54*, 798–807.

[95] Green, A. M.; Ofosu, C. K.; Kang, J.; Anslyn, E. V.; Truskett, T. M.; Milliron, D. J. Assembling Inorganic Nanocrystal Gels. *Nano Letters* **2022**, *22*, 1457–1466.

[96] Rogers, W. B.; Shih, W. M.; Manoharan, V. N. Using DNA to program the self-assembly of colloidal nanoparticles and microparticles. *Nature Reviews Materials* **2016**, *1*, 16008.

[97] Dominguez, M. N. et al. Assembly of Linked Nanocrystal Colloids by Reversible Covalent Bonds. *Chemistry of Materials* **2020**, *32*, 10235–10245.

[98] Kang, J.; Sherman, Z. M.; Conrad, D. L.; Crory, H. S. N.; Dominguez, M. N.; Valenzuela, S. A.; Anslyn, E. V.; Truskett, T. M.; Milliron, D. J. Structural Control of Plasmon Resonance in Molecularly Linked Metal Oxide Nanocrystal Gel Assemblies. *ACS Nano* **2023**, *17*, 24218–24226.

[99] Saez Cabezas, C. A.; Sherman, Z. M.; Howard, M. P.; Dominguez, M. N.; Cho, S. H.; Ong, G. K.; Green, A. M.; Truskett, T. M.; Milliron, D. J. Universal Gelation of Metal Oxide Nanocrystals via Depletion Attractions. *Nano Letters* **2020**, *20*, 4007–4013.

[100] Green, A. M.; Kadulkar, S.; Sherman, Z. M.; Fitzsimons, T. M.; Ofosu, C. K.; Yan, J.; Zhao, D.; Ilavsky, J.; Rosales, A. M.; Helms, B. A.; Ganesan, V.; Truskett, T. M.; Milliron, D. J. Depletion-Driven Assembly of Polymer-Coated Nanocrystals. *The Journal of Physical Chemistry C* **2022**, *126*, 19507–19518.

[101] Saez Cabezas, C. A.; Ong, G. K.; Jadrich, R. B.; Lindquist, B. A.; Agrawal, A.; Truskett, T. M.; Milliron, D. J. Gelation of plasmonic metal oxide nanocrystals by polymer-induced depletion attractions. *Proceedings of the National Academy of Sciences* **2018**, *115*, 8925–8930.

[102] Cai, Y.; Naser, N. Y.; Ma, J.; Baneyx, F. Precision Loading and Delivery of Molecular Cargo by Size-Controlled Coacervation of Gold Nanoparticles Functionalized with Elastin-like Peptides. *Biomacromolecules* **2024**, *25*, 2390–2398.

[103] Kang, J.; Valenzuela, S. A.; Lin, E. Y.; Dominguez, M. N.; Sherman, Z. M.; Truskett, T. M.; Anslyn, E. V.; Milliron, D. J. Colorimetric quantification of linking in thermoreversible nanocrystal gel assemblies. *Science Advances* **2022**, *8*, eabm7364.

[104] Herrmann, A.-K.; Formanek, P.; Borchardt, L.; Klose, M.; Giebeler, L.; Eckert, J.; Kaskel, S.; Gaponik, N.; Eychmüller, A. Multimetallic Aerogels by Template-Free Self-Assembly of Au, Ag, Pt, and Pd Nanoparticles. *Chemistry of Materials* **2013**, *26*, 1074–1083.

[105] Wen, D.; Liu, W.; Haubold, D.; Zhu, C.; Oschatz, M.; Holzschuh, M.; Wolf, A.; Simon, F.; Kaskel, S.; Eychmüller, A. Gold Aerogels: Three-Dimensional Assembly of Nanoparticles and Their Use as Electrocatalytic Interfaces. *ACS Nano* **2016**, *10*, 2559–2567.

[106] Torquato, S. Inverse optimization techniques for targeted self-assembly. *Soft Matter* **2009**, *5*, 1157.

[107] Jain, A.; Bollinger, J. A.; Truskett, T. M. Inverse methods for material design. *AIChE Journal* **2014**, *60*, 2732–2740.

[108] Sherman, Z. M.; Howard, M. P.; Lindquist, B. A.; Jadrich, R. B.; Truskett, T. M. Inverse methods for design of soft materials. *The Journal of Chemical Physics* **2020**, *152*.

[109] Chen, D.; Zhang, G.; Torquato, S. Inverse Design of Colloidal Crystals via Optimized Patchy Interactions. *The Journal of Physical Chemistry B* **2018**, *122*, 8462–8468.

[110] Coli, G. M.; Boattini, E.; Filion, L.; Dijkstra, M. Inverse design of soft materials via a deep learning–based evolutionary strategy. *Science Advances* **2022**, *8*.

[111] Petix, C. L.; Fakhraei, M.; Kieslich, C. A.; Howard, M. P. Surrogate Modeling of the Relative Entropy for Inverse Design Using Smolyak Sparse Grids. *Journal of Chemical Theory and Computation* **2023**, *20*, 1538–1546.

[112] Mahynski, N. A.; Mao, R.; Pretti, E.; Shen, V. K.; Mittal, J. Grand canonical inverse design of multicomponent colloidal crystals. *Soft Matter* **2020**, *16*, 3187–3194.

[113] Ma, Y.; Ferguson, A. L. Inverse design of self-assembling colloidal crystals with omnidirectional photonic bandgaps. *Soft Matter* **2019**, *15*, 8808–8826.

[114] Lindquist, B. A.; Jadrich, R. B.; Truskett, T. M. Communication: Inverse design for self-assembly via on-the-fly optimization. *The Journal of Chemical Physics* **2016**, *145*.

[115] Zhao, J.; Pinchuk, A. O.; McMahon, J. M.; Li, S.; Ausman, L. K.; Atkinson, A. L.; Schatz, G. C. Methods for Describing the Electromagnetic Properties of Silver and Gold Nanoparticles. *Accounts of Chemical Research* **2008**, *41*, 1710–1720.

[116] He, J.; He, C.; Zheng, C.; Wang, Q.; Ye, J. Plasmonic nanoparticle simulations and inverse design using machine learning. *Nanoscale* **2019**, *11*, 17444–17459.

[117] Kanehara, M.; Koike, H.; Yoshinaga, T.; Teranishi, T. Indium Tin Oxide Nanoparticles with Compositionally Tunable Surface Plasmon Resonance Frequencies in the Near-IR Region. *Journal of the American Chemical Society* **2009**, *131*, 17736–17737.

[118] Choi, S.-I.; Nam, K. M.; Park, B. K.; Seo, W. S.; Park, J. T. Preparation and Optical Properties of Colloidal, Monodisperse, and Highly Crystalline ITO Nanoparticles. *Chemistry of Materials* **2008**, *20*, 2609–2611.

[119] Wang, T.; Radovanovic, P. V. Free Electron Concentration in Colloidal Indium Tin Oxide Nanocrystals Determined by Their Size and Structure. *The Journal of Physical Chemistry C* **2010**, *115*, 406–413.

[120] Lee, J.; Lee, S.; Li, G.; Petruska, M. A.; Paine, D. C.; Sun, S. A Facile Solution-Phase Approach to Transparent and Conducting ITO Nanocrystal Assemblies. *Journal of the American Chemical Society* **2012**, *134*, 13410–13414.

[121] Crockett, B. M.; Jansons, A. W.; Koskela, K. M.; Johnson, D. W.; Hutchison, J. E. Radial Dopant Placement for Tuning Plasmonic Properties in Metal Oxide Nanocrystals. *ACS Nano* **2017**, *11*, 7719–7728.

[122] Lounis, S. D.; Runnerstrom, E. L.; Bergerud, A.; Nordlund, D.; Milliron, D. J. Influence of Dopant Distribution on the Plasmonic Properties of Indium Tin Oxide Nanocrystals. *Journal of the American Chemical Society* **2014**, *136*, 7110–7116.

[123] Kang, J.; Sherman, Z. M.; Crory, H. S. N.; Conrad, D. L.; Berry, M. W.; Roman, B. J.; Anslyn, E. V.; Truskett, T. M.; Milliron, D. J. Modular mixing in plasmonic metal oxide nanocrystal gels with thermoreversible links. *The Journal of Chemical Physics* **2023**, *158*.

[124] Sherman, Z. M.; Ghosh, D.; Swan, J. W. Field-Directed Self-Assembly of Mutually Polarizable Nanoparticles. *Langmuir* **2018**, *34*, 7117–7134.

[125] Vaddi, K.; Chiang, H. T.; Pozzo, L. D. Autonomous retrosynthesis of gold nanoparticles *via* spectral shape matching. *Digital Discovery* **2022**, *1*, 502–510.

[126] Krivina, R. A.; Knecht, T. A.; Crockett, B. M.; Boettcher, S. W.; Hutchison, J. E. Sculpting Optical Properties of Thin Film IR Filters through Nanocrystal Synthesis and Additive, Solution Processing. *Chemistry of Materials* **2020**, *32*, 8683–8693.

[127] Zhao, M.; Sikdar, D.; Zhao, M.; Ma, Y. 3D Self-Assembly of a Bilayer Nanoparticle Metasurface for Surface-Enhanced Raman Scattering (SERS) Sensing. *Nano Letters* **2025**, *25*, 8251–8257.

[128] Schulz, F.; Pavelka, O.; Lehmkühler, F.; Westermeier, F.; Okamura, Y.; Mueller, N. S.; Reich, S.; Lange, H. Structural order in plasmonic superlattices. *Nature Communications* **2020**, *11*.

[129] Lin, Q.-Y.; Mason, J. A.; Li, Z.; Zhou, W.; O'Brien, M. N.; Brown, K. A.; Jones, M. R.; Butun, S.; Lee, B.; Dravid, V. P.; Aydin, K.; Mirkin, C. A. Building superlattices from individual nanoparticles via template-confined DNA-mediated assembly. *Science* **2018**, *359*, 669–672.

[130] Fortini, A.; Martín-Fabiani, I.; De La Haye, J. L.; Dugas, P.-Y.; Lansalot, M.; D'Agosto, F.; Bourgeat-Lami, E.; Keddie, J. L.; Sear, R. P. Dynamic Stratification in Drying Films of Colloidal Mixtures. *Phys. Rev. Lett.* **2016**, *116*, 118301.

[131] Howard, M. P.; Nikoubashman, A.; Panagiotopoulos, A. Z. Stratification Dynamics in Drying Colloidal Mixtures. *Langmuir* **2017**, *33*, 3685–3693.

[132] Fernando, S.; Gunawardana, M. K.; Thilanka, T.; Bhatia, S. R. Evaporation-Induced Stratification in Nanoparticle Coatings: A Panoramic Overview of Single-Step Processes to Manufacture Multifunctional Films. *Industrial & Engineering Chemistry Research* **2025**, *64*, 18002–18012.

[133] Carr, A. J.; Rees-Zimmerman, C. R.; Zheng, B.; Routh, A. F.; Bhatia, S. R. Experimental and Numerical Investigation of Stratification Regimes in Drying Polystyrene and Silica Nanoparticle Films: Implications for Evaporative Self-Assembly of Colloidal Particles. *ACS Applied Nano Materials* **2024**, *7*, 8102–8112.

[134] Liu, X.; Liu, W.; Carr, A. J.; Santiago Vazquez, D.; Nykypanchuk, D.; Majewski, P. W.; Routh, A. F.; Bhatia, S. R. Stratification during evaporative assembly of multicomponent nanoparticle films. *Journal of Colloid and Interface Science* **2018**, *515*, 70–77.

[135] Jensen, J. S.; Sigmund, O. Systematic design of photonic crystal structures using topology optimization: Low-loss waveguide bends. *Applied Physics Letters* **2004**, *84*, 2022–2024.

[136] Jensen, J.; Sigmund, O. Topology optimization for nano-photonics. *Laser & Photonics Reviews* **2011**, *5*, 308–321.

[137] Lalau-Keraly, C. M.; Bhargava, S.; Miller, O. D.; Yablonovitch, E. Adjoint shape optimization applied to electromagnetic design. *Optics Express* **2013**, *21*, 21693.

[138] Matsunaga, K. Inverse Design of Colloidal Nanocrystal Assemblies With Targeted Structural and Optical Features. M.Sc. thesis, 2025; Copyright - Database copyright ProQuest LLC; ProQuest does not claim copyright in the individual underlying works; Last updated - 2026-02-18.

[139] Schoenholz, S. S.; Cubuk, E. D. JAX, M.D. A framework for differentiable physics. *J. Stat. Mech.* **2021**, *2021*, 124016.

[140] Goerlitzer, E. S. A.; Puri, A. S.; Moses, J. J.; Poulikakos, L. V.; Vogel, N. The Beginner's Guide to Chiral Plasmonics: Mostly Harmless Theory and the Design of Large-Area Substrates. *Advanced Optical Materials* **2021**, *9*.

[141] Kumar, J.; Thomas, K. G.; Liz-Marzán, L. M. Nanoscale chirality in metal and semiconductor nanoparticles. *Chemical Communications* **2016**, *52*, 12555–12569.

[142] Gardner, J.; Kusner, M.; Zhixiang; Weinberger, K.; Cunningham, J. Bayesian Optimization with Inequality Constraints. Proceedings of the 31st International Conference on Machine Learning. Bejing, China, 2014; pp 937–945.

[143] Fiore, A. M.; Balboa Usabiaga, F.; Donev, A.; Swan, J. W. Rapid sampling of stochastic displacements in Brownian dynamics simulations. *J. Chem. Phys.* **2017**, *146*, 124116.

[144] Lindbo, D.; Tornberg, A.-K. Spectral accuracy in fast Ewald-based methods for particle simulations. *J. Comp. Phys.* **2011**, *230*, 8744–8761.

[145] Zhu, H.; Walsh, T. F.; Semperlotti, F. Total-internal-reflection elastic metasurfaces: Design and application to structural vibration isolation. *Applied Physics Letters* **2018**, *113*, 221903.

[146] Castro, J. M.; Zhang, D.; Myer, B.; Kostuk, R. K. Energy collection efficiency of holographic planar solar concentrators. *Applied Optics* **2010**, *49*, 858.

[147] Xu, W.-Q.; Lin, D.-F.; Xu, X.; Ye, J.-S.; Wang, X.-K.; Feng, S.-F.; Sun, W.-F.; Han, P.; Zhang, Y.; Meng, Q.-B.; Yang, G.-Z. Simple and universal method in designs of high-efficiency diffractive optical elements for spectrum separation and beam concentration. *Chinese Physics B* **2017**, *26*, 074202.

[148] Schubert, M. L.; Fischbach, J. D.; Nyman, M.; Lüer, L.; Brabec, C. J.; Rockstuhl, C.; Sturges, T. J. Wide angle tolerant solar spectral splitter for lateral tandem solar cells. *APL Photonics* **2025**, *10*, 066105.

[149] Ge, J.; Hu, Y.; Yin, Y. Highly Tunable Superparamagnetic Colloidal Photonic Crystals. *Angewandte Chemie International Edition* **2007**, *46*, 7428–7431.

[150] Daqiqeh Rezaei, S.; Dong, Z.; You En Chan, J.; Trisno, J.; Ng, R. J. H.; Ruan, Q.; Qiu, C.-W.; Mortensen, N. A.; Yang, J. K. Nanophotonic Structural Colors. *ACS Photonics* **2021**, *8*, 18–33.

[151] Kim, S.; Mitropoulos, A. N.; Spitzberg, J. D.; Tao, H.; Kaplan, D. L.; Omenetto, F. G. Silk inverse opals. *Nature Photonics* **2012**, *6*, 818–823.

[152] Xuan, Z.; Li, J.; Liu, Q.; Yi, F.; Wang, S.; Lu, W. Artificial Structural Colors and Applications. *The Innovation* **2021**, *2*, 100081.

[153] Wu, C.; Fan, Q.; Wu, W.; Liang, T.; Liu, Y.; Yu, H.; Yin, Y. Magnetically Tunable One-Dimensional Plasmonic Photonic Crystals. *Nano Letters* **2023**, *23*, 1981–1988.

[154] Zeng, J.; Zhang, Y.; Zeng, T.; Aleisa, R.; Qiu, Z.; Chen, Y.; Huang, J.; Wang, D.; Yan, Z.; Yin, Y. Anisotropic plasmonic nanostructures for colorimetric sensing. *Nano Today* **2020**, *32*, 100855.

[155] Atkinson, R.; Hendren, W. R.; Wurtz, G. A.; Dickson, W.; Zayats, A. V.; Evans, P.; Pollard, R. J. Anisotropic optical properties of arrays of gold nanorods embedded in alumina. *Physical Review B* **2006**, *73*, 235402.

[156] Liz-Marzán, L. M. Tailoring Surface Plasmons through the Morphology and Assembly of Metal Nanoparticles. *Langmuir* **2006**, *22*, 32–41.

[157] Born, M.; Wolf, E. *Principles of optics: electromagnetic theory of propagation, interference and diffraction of light*, 6th ed.; Cambridge University Press: Cambridge, 1999.

[158] Sanghavi, R.; Intan, N. N.; Xie, S.; Lin, H.; Pfaendtner, J. Reaction Pathway Analysis of PET Deconstruction via Methanolysis and Tertiary Amine Catalysts. *The Journal of Physical Chemistry A* **2024**, *128*, 5883–5891.

[159] Geyer, R.; Jambeck, J. R.; Law, K. L. Production, use, and fate of all plastics ever made. *Science Advances* **2017**, *3*, e1700782.

[160] Li, T.; Vijeta, A.; Casadevall, C.; Gentleman, A. S.; Euser, T.; Reisner, E. Bridging Plastic Recycling and Organic Catalysis: Photocatalytic Deconstruction of Polystyrene via a C–H Oxidation Pathway. *ACS Catalysis* **2022**, *12*, 8155–8163.

[161] Guo, B.; Vanga, S. R.; Lopez-Lorenzo, X.; Saenz-Mendez, P.; Ericsson, S. R.; Fang, Y.; Ye, X.; Schriever, K.; Bäckström, E.; Biundo, A.; Zubarev, R. A.; Furó, I.; Hakkarainen, M.; Syrén, P.-O. Conformational Selection in Biocatalytic Plastic Degradation by PETase. *ACS Catalysis* **2022**, *12*, 3397–3409.

[162] Jambeck, J. R.; Geyer, R.; Wilcox, C.; Siegler, T. R.; Perryman, M.; Andrady, A.; Narayan, R.; Law, K. L. Plastic waste inputs from land into the ocean. *Science* **2015**, *347*, 768–771.

[163] Hundertmark, T.; Mayer, M.; McNally, C. How plastics waste recycling could transform the chemical industry. `https://www.mckinsey.com/industries/chemicals/our-insights/how-plastics-waste-recycling-could-transform-the-chemical-industry.`

[164] Cao, F.; Wang, L.; Zheng, R.; Guo, L.; Chen, Y.; Qian, X. Research and progress of chemical depolymerization of waste PET and high-value application of its depolymerization products. *RSC Advances* **2022**, *12*, 31564–31576.

[165] Yang, W.; Liu, R.; Li, C.; Song, Y.; Hu, C. Hydrolysis of waste polyethylene terephthalate catalyzed by easily recyclable terephthalic acid. *Waste Management* **2021**, *135*, 267–274.

[166] Kang, M. J.; Yu, H. J.; Jegal, J.; Kim, H. S.; Cha, H. G. Depolymerization of PET into terephthalic acid in neutral media catalyzed by the ZSM-5 acidic catalyst. *Chemical Engineering Journal* **2020**, *398*, 125655.

[167] Yoshioka, T.; Sato, T.; Okuwaki, A. Hydrolysis of waste PET by sulfuric acid at 150°C for a chemical recycling. *Journal of Applied Polymer Science* **1994**, *52*, 1353–1355.

[168] Wang, Y.; Zhang, Y.; Song, H.; Wang, Y.; Deng, T.; Hou, X. Zinc-catalyzed ester bond cleavage: Chemical degradation of polyethylene terephthalate. *Journal of Cleaner Production* **2019**, *208*, 1469–1475.

[169] Song, X.; Hu, W.; Huang, W.; Wang, H.; Yan, S.; Yu, S.; Liu, F. Methanolysis of polycarbonate into valuable product bisphenol A using choline chloride-based deep eutectic solvents as highly active catalysts. *Chemical Engineering Journal* **2020**, *388*, 124324.

[170] Pham, D. D.; Cho, J. Low-energy catalytic methanolysis of poly(ethyleneterephthalate). *Green Chemistry* **2021**, *23*, 511–525.

[171] Kurokawa, H.; Ohshima, M.-a.; Sugiyama, K.; Miura, H. Methanolysis of polyethylene terephthalate (PET) in the presence of aluminium tiisopropoxide catalyst to form dimethyl terephthalate and ethylene glycol. *Polymer Degradation and Stability* **2003**, *79*, 529–533.

[172] Pingale, N. D.; Palekar, V. S.; Shukla, S. R. Glycolysis of postconsumer polyethylene terephthalate waste. *Journal of Applied Polymer Science* **2010**, *115*, 249–254.

[173] Wang, H.; Liu, Y.; Li, Z.; Zhang, X.; Zhang, S.; Zhang, Y. Glycolysis of poly(ethylene terephthalate) catalyzed by ionic liquids. *European Polymer Journal* **2009**, *45*, 1535–1544.

[174] Liu, B.; Lu, X.; Ju, Z.; Sun, P.; Xin, J.; Yao, X.; Zhou, Q.; Zhang, S. Ultrafast Homogeneous Glycolysis of Waste Polyethylene Terephthalate via a Dissolution-Degradation Strategy. *Industrial & Engineering Chemistry Research* **2018**, *57*, 16239–16245.

[175] Gupta, P.; Bhandari, S. *Recycling of Polyethylene Terephthalate Bottles*; Elsevier, 2019; pp 109–134.

[176] Carniel, A.; Waldow, V. D. A.; Castro, A. M. D. A comprehensive and critical review on key elements to implement enzymatic PET depolymerization for recycling purposes. *Biotechnology Advances* **2021**, *52*, 107811.

[177] Lee, H. L.; Chiu, C. W.; Lee, T. Engineering terephthalic acid product from recycling of PET bottles waste for downstream operations. *Chemical Engineering Journal Advances* **2021**, *5*, 1–14.

[178] da Costa, A. M.; de Oliveira Lopes, V. R.; Vidal, L.; Nicaud, J.-M.; de Castro, A. M.; Coelho, M. A. Z. Poly(ethylene terephthalate) (PET) degradation by Yarrowia lipolytica: Investigations on cell growth, enzyme production and monomers consumption. *Process Biochemistry* **2020**, *95*, 81–90.

[179] Duh, B. Reaction kinetics for solid-state polymerization of poly(ethylene terephthalate). *Journal of Applied Polymer Science* **2001**, *81*, 1748–1761.

[180] Lawal, M. M.; Govender, T.; Maguire, G. E. M.; Kruger, H. G.; Honarparvar, B. DFT study of the acid-catalyzed esterification reaction mechanism of methanol with carboxylic acid and its halide derivatives. *International Journal of Quantum Chemistry* **2018**, *118*, e25497–e25497.

[181] Baliga, S.; Wong, W. T. Depolymerization of poly(ethylene terephthalate) recycled from postconsumer soft-drink bottles. *Journal of Polymer Science Part A: Polymer Chemistry* **1989**, *27*, 2071–2082.

[182] Xi, G.; Lu, M.; Sun, C. Study on depolymerization of waste polyethylene terephthalate into monomer of bis(2-hydroxyethyl terephthalate). *Polymer Degradation and Stability* **2005**, *87*, 117–120.

[183] Ghaemy, M.; Mossaddegh, K. Depolymerisation of poly(ethylene terephthalate) fibre wastes using ethylene glycol. *Polymer Degradation and Stability* **2005**, *90*, 570–576.

[184] Shukla, S. R.; Kulkarni, K. S. Depolymerization of poly(ethylene terephthalate) waste. *Journal of Applied Polymer Science* **2002**, *85*, 1765–1770.

[185] Bao, Y.-S.; Zhaorigetu, B.; Agula, B.; Baiyin, M.; Jia, M. Aminolysis of Aryl Ester Using Tertiary Amine as Amino Donor via C–O and C–N Bond Activations. *The Journal of Organic Chemistry* **2014**, *79*, 803–808.

[186] Oliveri, I. P.; Di Bella, S. Sensitive Fluorescent Detection and Lewis Basicity of Aliphatic Amines. *The Journal of Physical Chemistry A* **2011**, *115*, 14325–14330.

[187] Lin, H. Conversion of co-mingled waste plastics to monomers and fuels in sequential catalytic process.

[188] Frisch, M. J. et al. Gaussian 16 Rev. C.01. **2016**, Place: Wallingford, CT.

[189] Zhao, Y.; Truhlar, D. G. The M06 suite of density functionals for main group thermochemistry, thermochemical kinetics, noncovalent interactions, excited states, and transition elements: two new functionals and systematic testing of four M06-class functionals and 12 other functionals. *Theoretical Chemistry Accounts* **2008**, *120*, 215–241.

[190] Francl, M. M.; Pietro, W. J.; Hehre, W. J.; Binkley, J. S.; Gordon, M. S.; DeFrees, D. J.; Pople, J. A. Self-consistent molecular orbital methods. XXIII. A polarization-type basis set for second-row elements. *The Journal of Chemical Physics* **1982**, *77*, 3654–3665.

[191] Hehre, W. J.; Ditchfield, R.; Pople, J. A. Self—Consistent Molecular Orbital Methods. XII. Further Extensions of Gaussian—Type Basis Sets for Use in Molecular Orbital Studies of Organic Molecules. *The Journal of Chemical Physics* **1972**, *56*, 2257–2261.

[192] Cammi, R.; Tomasi, J. Remarks on the use of the apparent surface charges (ASC) methods in solvation problems: Iterative versus matrix-inversion procedures and the renormalization of the apparent charges. *Journal of Computational Chemistry* **1995**, *16*, 1449–1458.

[193] Miertuš, S.; Scrocco, E.; Tomasi, J. Electrostatic interaction of a solute with a continuum. A direct utilizaion of AB initio molecular potentials for the prevision of solvent effects. *Chemical Physics* **1981**, *55*, 117–129.

[194] Mennucci, B.; Cancès, E.; Tomasi, J. Evaluation of Solvent Effects in Isotropic and Anisotropic Dielectrics and in Ionic Solutions with a Unified Integral Equation Method: Theoretical Bases, Computational Implementation, and Numerical Applications. *The Journal of Physical Chemistry B* **1997**, *101*, 10506–10517.

[195] Cancès, E.; Mennucci, B.; Tomasi, J. A new integral equation formalism for the polarizable continuum model: Theoretical background and applications to isotropic and anisotropic dielectrics. *The Journal of Chemical Physics* **1997**, *107*, 3032–3041.

[196] Cancès, E.; Mennucci, B. New applications of integral equations methods for solvation continuum models: ionic solutions and liquid crystals. *Journal of Mathematical Chemistry* **1998**, *23*, 309–326.

[197] Fukui, K. The path of chemical reactions - the IRC approach. *Accounts of Chemical Research* **1981**, *14*, 363–368.

[198] Breneman, C. M.; Wiberg, K. B. Determining atom-centered monopoles from molecular electrostatic potentials. The need for high sampling density in formamide conformational analysis. *Journal of Computational Chemistry* **1990**, *11*, 361–373.

[199] Krishnan, R.; Binkley, J. S.; Seeger, R.; Pople, J. A. Self-consistent molecular orbital methods. XX. A basis set for correlated wave functions. *The Journal of Chemical Physics* **1980**, *72*, 650–654.

[200] Clark, T.; Chandrasekhar, J.; Spitznagel, G. W.; Schleyer, P. V. R. Efficient diffuse function-augmented basis sets for anion calculations. III. The 3-21+G basis set for first-row elements, Li-F. *Journal of Computational Chemistry* **1983**, *4*, 294–301.

[201] The PLUMED consortium Promoting transparency and reproducibility in enhanced molecular simulations. *Nature Methods* **2019**, *16*, 670–673.

[202] Tribello, G. A.; Bonomi, M.; Branduardi, D.; Camilloni, C.; Bussi, G. PLUMED 2: New feathers for an old bird. *Computer Physics Communications* **2014**, *185*, 604–613.

[203] Kenouche, S.; Belkadi, A.; Djebaili, R.; Melkemi, N. High regioselectivity in the amination reaction of isoquinolinequinone derivatives using conceptual DFT and NCI analysis. *Journal of Molecular Graphics and Modelling* **2021**, *104*, 107828.

[204] Sarala, S.; Geetha, S.; Muthu, S.; Irfan, A. Probing solvent effect and strong and weak interactions in 2-Nitrophenyl-hydrazine using independent gradient model and Hirshfeld from wave function calculation. *Journal of Molecular Liquids* **2021**, *341*, 117345.

[205] Borges, I. D.; Danielli, J. A. V.; Silva, V. E. G.; Sallum, L. O.; Queiroz, J. E.; Dias, L. D.; Iermak, I.; Aquino, G. L. B.; Camargo, A. J.; Valverde, C.; Osório, F. A. P.; Baseia, B.; Napolitano, H. B. Synthesis and structural studies on (*E*)-3-(2,6-difluorophenyl)-1-(4-fluorophenyl)prop-2-en-1-one: a promising nonlinear optical material. *RSC Advances* **2020**, *10*, 22542–22555.

[206] Silva, P. L.; Silva, C. M.; Guimarães, L.; Pliego, J. R. Acid-catalyzed transesterification and esterification in methanol: a theoretical cluster-continuum investigation of the mechanisms and free energy barriers. *Theoretical Chemistry Accounts* **2015**, *134*, 1591.

[207] Ismail, M.; Cabañero, M. A.; Orive, J.; Babulal, L. M.; Garcia, J.; Morant-Miñana, M. C.; Dauvergne, J.-L.; Bonilla, F.; Monterrubio, I.; Carrasco, J.; Saracibar, A.; Reynaud, M. ADEL: an automated drop-cast electrode setup for high-throughput screening of battery materials. *Digital Discovery* **2025**, *4*, 943–953.